

AMERICAN UNIVERSITY OF BEIRUT

ELECTROCHEMICAL INVESTIGATION OF THE EFFECTS OF
GUEST METALS IN NICKEL HYDROXIDE FILMS ON
OXYGEN EVOLUTION REACTION CATALYSIS

by
RIDA JAMAL FARHAT

A thesis
submitted in partial fulfillment of the requirements
for the degree of Master of Science
to the Department of Chemistry
of the Faculty of Arts and Sciences
at the American University of Beirut

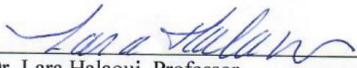
Beirut, Lebanon
June 2020

AMERICAN UNIVERSITY OF BEIRUT

ELECTROCHEMICAL INVESTIGATION OF THE EFFECTS OF
GUEST METALS IN NICKEL HYDROXIDE FILMS ON
OXYGEN EVOLUTION REACTION CATALYSIS

by
RIDA JAMAL FARHAT

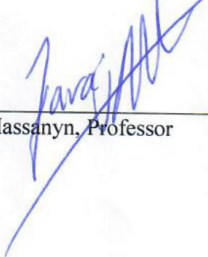
Approved by:



Dr. Lara Halaoui, Professor
Chemistry
Advisor



Dr. Tarek Ghaddar, Professor
Chemistry
Member of Committee



Dr. Faraj Hassany, Professor
Chemistry
Member of Committee

Date of thesis defense: June 15, 2020

AMERICAN UNIVERSITY OF BEIRUT

THESIS, DISSERTATION, PROJECT RELEASE FORM

Student Name: Rida Jamal Farhat

Master's Thesis Master's Project Doctoral Dissertation

I authorize the American University of Beirut to: (a) reproduce hard or electronic copies of my thesis, dissertation, or project; (b) include such copies in the archives and digital repositories of the University; and (c) make freely available such copies to third parties for research or educational purposes.

I authorize the American University of Beirut, to: (a) reproduce hard or electronic copies of it; (b) include such copies in the archives and digital repositories of the University; and (c) make freely available such copies to third parties for research or educational purposes after:

One --- year from the date of submission of my thesis, dissertation, or project.

Two --- years from the date of submission of my thesis, dissertation, or project.

Three --- years from the date of submission of my thesis, dissertation, or project.



Signature

5/7/2020

Date

ACKNOWLEDGMENTS

I wish to express my deepest gratitude and thanks to Dr. Lara Halaoui for her constant efforts and guidance as my research adviser. Her consistent advice and overall professionalism helped mold me into the chemist that I am today. I am more than proud to be a member in her research group.

I wish to express my sincere thanks and respect to the committee members, Dr. Tarek Ghaddar and Dr. Faraj Hasanayn, for the guidance and feedback.

Some of the experiments (of the large number of films conducted in this study) were performed by or in collaboration and direct help of research assistant, Jihan Dhainy. Thus, I would like to whole-heartedly thank the members of the Halaoui Group, Jihan Dhainy, Marwa Al Rammal, Nour Beydoun and Khalil Akkaoui, for their help, guidance and motivation. The knowledge I have gained by joining the Halaoui Group, whether from my adviser or colleagues, is indispensable.

I acknowledge the technical support and overall help of the CRSL team, Ms. Rania Shatila, Mr. Joan Younes, Mr. Samer Khalil and Mr. Chady Assaf, and technicians Mr. Simon Al-Ghawi and Mr. Boutros Sawaya.

I sincerely appreciate the constant support by my colleagues and peers during my MS studies.

I dedicate this work to my family for their never-ending support and motivation. I would like to offer my deepest gratitude and thanks to my mother, my father, my brother, my aunts and cousins. I would specifically dedicate this work to the people I lost during this journey and who could not see me finish it, my guardian angels, my grandmother and my best friend, Grace.

AN ABSTRACT OF THE THESIS OF

Rida Jamal Farhat for

Master of Science

Major: Chemistry

Title: Electrochemical Investigation of the Effects of Guest Metals in Nickel Hydroxide Films on Oxygen Evolution Reaction Catalysis.

The sun is the largest and cheapest green energy source worldwide with one hour of solar energy outweighing the global energy consumption per year. Thus, the generation of renewable energy using nanomaterials is a rising topic in science today especially via solar water splitting at nanostructures coupled with co-catalysts. This MS thesis focuses on investigating oxygen evolution reaction (OER) catalysts from earth abundant materials and the role of guest metal inclusion.

The aim of this project is to investigate the effect of guest metals, Fe and Al, on Ni-based oxide catalysts for oxygen evolution reactions as a function of i) mode of inclusion, ii) electrolyte and iii) the presence and absence of Fe in solution. Thin Ni-oxo/hydroxo films have shown significant activity as non-noble metal OER electrocatalysts. A promoting effect has been reported with the addition of certain supplementary metals particularly Fe. Nonetheless, the role of guest metals in solution has yet to be fully and clearly understood. Earlier in this laboratory, Ni-oxo/hydroxo films in borate, KB_i , were investigated in the presence and absence of Fe: as-deposited and after anodic conditioning. Differences in OER activity between co-electrodeposition and inclusion post-deposition of Fe led to the hypothesis that surface modification with Fe causes an increase in OER activity rather than its bulk inclusion. Furthermore, it was observed earlier in this laboratory that Al in solution inhibits OER.¹ In this MS thesis,

we investigate the electrochemistry and OER activity at Ni-oxohydroxo, Ni(Fe) and Ni(Al)-oxohydroxo films in KBi, KOH purified from Fe and KOH with traces of Fe. OER activity of NiO_xH_y and co-deposited NiAlO_xH_y and NiFeO_xH_y was studied in KOH electrolytes which were unpurified or purified from Fe impurities to eliminate any trace Fe that would modify the catalyst surface. The effect of Al and Fe added to these electrolytes was also studied. The effects of the guest metals on the redox behavior of Ni-based oxides on OER electrocatalytic activity and stability were studied using cyclic voltammetry, Tafel slope measurements, current-overpotential and turnover frequency calculations. The films were characterized using SEM coupled with EDX to examine the surface structure and morphology of the catalysts.

The complete removal of Fe from the electrolyte resulted in low OER activity at both Ni and Ni(Fe) co-deposited films and thus supports our hypothesis that bulk Fe does not promote OER. The presence of Fe in 1 M KOH showed an increase in OER activity of NiO_xH_y , while the addition of Al to 1 M KBi inhibited OER activity. The OER activity was not sustained at Fe-activated NiO_xH_y in Fe-free electrolyte indicated that the presence of Fe is needed for sustainability of active sites. A deactivation mechanism consistent with the electrochemical results was proposed for OER activity. The addition of Al to 1 M KOH and 1 M Fe-free KOH did not cause an effect on OER but affected the redox behavior of the catalyst. The co-deposition of Al with Ni showed no significant effect on Tafel slopes but a varied effect on TOF at different thicknesses in the tested electrolytes.

CONTENTS

ACKNOWLEDGMENTS.....	v
ABSTRACT.....	vi
LIST OF ILLUSTRATIONS.....	xii
LIST OF TABLES.....	xviii

Chapter

I. INTRODUCTION.....	1
A. Water Splitting.....	1
B. Oxygen Evolution Reaction.....	4
C. Previous Metal Based OER Electrocatalysts.....	8
D. Non-Precious Metal Based OER Electrocatalysts.....	10
1. Types of Non-Precious Metal Based OER Electrocatalysts.....	10
2. Ni-oxo/hydroxide OER Electrocatalysts.....	12
a. Structure.....	12
b. Preparation and Synthesis.....	14
c. Ion Inclusion in Solution.....	15
d. Codeposition of Fe.....	18
e. Codeposition of Other Metals.....	20
II. EXPERIMENTAL SECTION.....	23
A. Materials.....	23

B. Preparation of Solutions.....	23
1. Preparation of KOH and KBi electrolytes.....	23
2. KOH Electrolyte Purification.....	24
C. Electrodeposition of NiO _x H _y , NiFeO _x H _y and NiAlO _x H _y	25
1. Preparation of Substrates.....	25
2. Preparation of Ni-Bi, NiFe-Bi and NiAl-Bi Solutions.....	26
3. Electrodeposition of NiO _x H _y , NiFeO _x H _y and NiAlO _x H _y on FTO.....	26
D. Electrochemical Measurements.....	27
1. Cyclic Voltammetry.....	27
2. Tafel Plot Measurements.....	28
3. Effect of Potential Cycling.....	28
4. Sustainability of Active Sites.....	29
5. Addition of Metal Impurities to the Electrolyte.....	29
6. Electrode Aging in Fe-free KOH.....	31
E. SEM Imaging and EDX.....	31

III. INVESTIGATION OF THE EFFECTS OF IRON IN NICKEL HYDROXIDE FILMS ON OXYGEN EVOLUTION REACTION CATALYSIS.....32

A. Dependence of OER Catalysis at NiO _x H _y on Surface-Fe vs. Bulk-Fe.....	34
1. Effect of Fe Co-deposition in Thin Ni _{0.6} Fe _{0.4} O _x H _y) _{1mC} on the Electrochemical Behavior and OER in 1 M Fe-free KOH and 1 M Unpurified KOH.....	34
a. Effect of Fe on OER Catalysis.....	34
b. Effect of Fe on Redox Peak Behavior.....	44

2. Effect of Fe Co-deposition in Thick Ni _{0.6} Fe _{0.4} O _x H _y) _{100mC} on the Electrochemical Behavior and OER in 1 M Fe-free KOH and 1 M Unpurified KOH.....	45
a. Effect of Fe on OER Catalysis.....	45
b. Effect of Fe on Redox Peak Behavior.....	57
B. Sustainability of Active Site in the Absence of Fe in Solution.....	59
C. Dependence of OER Activity at Ni(Fe)-Oxo/Hydroxide on the Presence of Fe in Solution.....	63
1. Possible Deactivation Mechanism.....	63
2. Examining Other Possibilities for Deactivation.....	65
3. Examining Possible Effects of Other Impurities.....	70
a. Examining the Effect of Pt Addition.....	70
b. Discussion of Other Possible Impurities in KOH.....	72
4. Differences from Literature.....	72
a. Differences in Deposition Technique and Initial Catalyst Structure with Fe Co-deposition.....	72
b. Different Deposition Methods at Other Transition Metal Based OER Catalyst Systems.....	73
D. Conclusions.....	74

IV. INVESTIGATION OF THE EFFECTS OF ALUMINUM IN NICKEL HYDROXIDE FILMS ON OXYGEN EVOLUTION REACTION CATALYSIS.....76

A. Effect of the Al in Solution on Ni-oxo/hydroxide Films.....	78
1. Effect of Al Addition in 1 M KBi on Electrochemical Behavior and OER of Ni-Bi.....	79
2. Effect of Al Addition in KOH on the Electrochemical Behavior and OER of NiO _x H _y	83
B. Effect of the Co-deposition of Al on Ni-oxo/hydroxide Films.....	88

1. Effect of Al Co-deposition in Thin $\text{Ni}_{0.6}\text{Al}_{0.4}\text{-Bi)}_{1\text{mC}}$ on the Electrochemical Behavior and OER in 1 M KBi.....	88
2. Effect of Al Co-deposition in Thin $\text{Ni}_{0.6}\text{Al}_{0.4}\text{O}_x\text{H}_y)_{1\text{mC}}$ on the Electrochemical Behavior and OER in 1 M Fe-free KOH.....	96
3. Effect of Al Co-deposition in Thin $\text{Ni}_{0.6}\text{Al}_{0.4}\text{O}_x\text{H}_y)_{1\text{mC}}$ on the Electrochemical Behavior and OER in 1 M Unpurified KOH.....	105
4. Thicker Films in 1 M Fe-free KOH and 1 M KOH.....	112
C. Conclusions.....	127
 V. CONCLUSIONS.....	 132
 REFERENCES.....	 135

ILLUSTRATIONS

Figure	Page
1.1: Modelled Tafel slopes and their corresponding rate-determining steps based on the work of Doyle et al. and Shinagawa et al. “-” represents an unreported Tafel slope.....	7
1.2: Volcano relation OER plot showing the electrocatalytic activity in acid as closed circles and in alkaline as open circles. Copyright American Chemical Society 2010.....	9
1.3: Bode diagram showing the transformations of Ni(OH) ₂ /NiOOH. Adopted from reference 83. Copyright American Chemical Society 2020.....	13
2.1: Scheme illustrating the purification of KOH from Fe traces.....	24
2.2: Scheme illustrating the electrodeposition of NiO _x H _y	27
3.1: Cyclic voltammograms in 1 M Fe-free KOH at NiO _x H _y) _{1mC} (A) and Ni _{0.6} Fe _{0.4} O _x H _y) _{1mC} (B) as a first scan (a, blue), after anodic conditioning in the same solution (b, red) and after Tafel measurements (c, green). The insets show the corresponding redox peaks and onset of oxygen evolution for the three scans shown. Scan rate is 10 mV/s.....	35
3.2: Cyclic voltammograms of the second set of films in 1 M Fe-free KOH at NiO _x H _y) _{1mC} (A) and Ni _{0.6} Fe _{0.4} O _x H _y) _{1mC} (B) as a first scan (a, blue), after anodic conditioning in the same solution (b, red) and after Tafel measurements (c, green). The insets show the corresponding redox peaks and onset of oxygen evolution for the three scans shown. Scan rate is 10 mV/s.....	37
3.3: Cyclic voltammograms of NiO _x H _y) _{1mC} film in 1 M Fe-free KOH as a first scan (CV ₁ blue) and then CVs acquired after 10 CVs were taken at 100 mV/s, repeated 7 times in the same solution. The insets show the Ni(OH) ₂ /NiOOH redox peaks. The number of CVs (10-70) refers to the total number of scans acquired at 100 mV/s. Scan rate of all CVs in this figure is 10 mV/s.....	38
3.4: Tafel plots, overpotential η (mV) versus $\log(J \text{ A/cm}^2)$, for NiO _x H _y) _{1mC} and Ni _{0.6} Fe _{0.4} O _x H _y) _{1mC} films anodized in 1 M Fe-free KOH and measured in the same solutions (a-b) and NiO _x H _y) _{1mC} and Ni _{0.6} Fe _{0.4} O _x H _y) _{1mC} films anodized in 1 M unpurified KOH and measured in the same solution (c-d). These Tafel plots correspond to films whose CVs are presented in Figure 3.1-3.5 (A) and 3.2-3.6 (B).....	39
3.5: Cyclic voltammograms in 1 M KOH at NiO _x H _y) _{1mC} (A) and Ni _{0.6} Fe _{0.4} O _x H _y) _{1mC} (B) as a first scan (a, blue), after anodic conditioning in the same solution (b, red) and after Tafel measurements (c, green). The insets show the corresponding redox peaks and onset of oxygen evolution for the three scans shown. Scan rate is 10 mV/s.....	40
3.6: Cyclic voltammograms of the second set of films in 1 M KOH at NiO _x H _y) _{1mC} (A) and Ni _{0.6} Fe _{0.4} O _x H _y) _{1mC} (B) as a first scan (a, blue), after anodic conditioning in the same	

solution (b, red) and after Tafel measurements (c, green). The insets show the corresponding redox peaks and onset of oxygen evolution for the three scans shown. Scan rate is 10 mV/s.....	41
3.7: Cyclic voltammograms of NiO_xH_y) _{1mC} film in 1 M KOH as a first scan (CV ₁ blue) and then CVs acquired after 10 CVs were taken at 100 mV/s, repeated 6 times in the same solution. The insets show the $\text{Ni}(\text{OH})_2/\text{NiOOH}$ redox peaks. The number of CVs (10-60) refers to the total number of scans acquired at 100 mV/s. Scan rate of all CVs in this figure is 10 mV/s.....	42
3.8: Normalized Tafel plots, overpotential η (mV) versus $\log(I/n \text{ A.nmol}^{-1})$, where nmol is for the electrochemically active Ni centers, for NiO_xH_y) _{1mC} , and $\text{Ni}_{0.6}\text{Fe}_{0.4}\text{O}_x\text{H}_y$) _{1mC} films anodized in 1 M Fe-free KOH (a-b) and unpurified 1 M KOH (c-d), and measured in the same solution: for the Tafel plots in Figure 3.1 and 3.5 using 1.2e/Ni for determining nmol of Ni for all films in both solutions.....	43
3.9: Cyclic voltammograms in 1 M Fe-free KOH (A, B) and in 1 M KOH (C, D) at NiO_xH_y) _{100mC} (A, C) and $\text{Ni}_{0.6}\text{Fe}_{0.4}\text{O}_x\text{H}_y$) _{100mC} (B, D) as a first scan (a, blue), after anodic conditioning in the same solution (b, red) and after Tafel measurements (c, green). The insets show the corresponding redox peaks and onset of oxygen evolution for the three scans shown. Scan rate is 10 mV/s.....	45
3.10: SEM image (A) and EDX spectrum (B) of an as-deposited $\text{Ni}_{0.6}\text{Fe}_{0.4}\text{O}_x\text{H}_y$) _{100mC} film.....	47
3.11: Powder X-ray diffraction (XRD) patterns for $\text{Ni}_{0.6}\text{Fe}_{0.4}\text{O}_x\text{H}_y$) _{100mC} on FTO, as-deposited (A) and anodized in 1 M Fe-free KOH (B), and two different FTO electrodes (C).....	48
3.12: Cyclic Voltammograms, J (mA/cm^2) versus E (V) vs. Ag/AgCl (A, C), and normalized cyclic voltammograms, I/n (mA/nmol) versus η (V) (B, D), at NiO_xH_y) _{100mC} (a, blue) and $\text{Ni}_{0.6}\text{Fe}_{0.4}\text{O}_x\text{H}_y$) _{100mC} (b, red) in 1 M Fe-free KOH (A-B) and in 1 M KOH (C-D) as a first scan. The insets show the $\text{Ni}(\text{OH})_2/\text{NiOOH}$ redox peaks and the onset of oxygen evolution for the three scans shown at each film. Scan rate is 10 mV/s.....	49
3.13: Cyclic voltammograms of $\text{Ni}_{0.6}\text{Fe}_{0.4}\text{O}_x\text{H}_y$) _{100mC} film in 1 M Fe-free KOH, as a first scan (CV ₁ blue) and then CVs acquired after 10 CVs were taken at 100 mV/s, repeated 6 times in the same solution. Scan rate of all CVs in this figure is 10 mV/s. The insets show the $\text{Ni}(\text{OH})_2/\text{NiOOH}$ redox peaks. The number of CVs (10-60) refers to the total number of scans acquired at 100 mV/s.....	51
3.14: Anodization plots (i-t plots) of ultra-thin $\text{Ni}_{0.6}\text{Fe}_{0.4}\text{O}_x\text{H}_y$) _{1mC} (A) and thicker $\text{Ni}_{0.6}\text{Fe}_{0.4}\text{O}_x\text{H}_y$) _{100mC} (B) films biased at 0.5 V vs. Ag/AgCl in 1 M Fe-free KOH (a, red traces) or unpurified 1 M KOH (b, blue traces) as indicated.....	52
3.15: Tafel plots (A) and normalized Tafel plots (B) (C) for $\text{Ni}_{0.6}\text{Fe}_{0.4}\text{O}_x\text{H}_y$) _{100mC} (a-c) and NiO_xH_y) _{100mC} (d-e) films anodized in 1 M unpurified KOH and measured in the same solutions. Normalization was done using 1.2e/Ni for nmol of Ni (B) and for determining nmol of metal, assuming 40% Fe content, for $\text{Ni}_{0.6}\text{Fe}_{0.4}\text{O}_x\text{H}_y$) _{100mC} (C).	

Tafel plots (D) and normalized Tafel plots (E) for NiO_xH_y)_{1mC} (a), $\text{Ni}_{0.6}\text{Fe}_{0.4}\text{O}_x\text{H}_y$)_{1mC} (b), NiO_xH_y)_{10mC} (c) and $\text{Ni}_{0.6}\text{Fe}_{0.4}\text{O}_x\text{H}_y$)_{10mC} (d) films anodized in 1 M KOH and measured in the same solutions. Normalization was done using 1.2e/Ni for determining nmol of Ni in (E). Plot (d) from (B) has been added in (E) for comparison. Number of mole of Ni are calculated from post-Tafel. Note that Hg/HgO was used for one of the Tafel plots of NiO_xH_y)₁₀₀ (orange. A and B), in the rest used Ag/AgCl.....54

3.16: Tafel plots (A) and normalized Tafel plots (B) for $\text{Ni}_{0.6}\text{Fe}_{0.4}\text{O}_x\text{H}_y$)_{100mC} (a-b) and NiO_xH_y)_{100mC} (c-e) films anodized in 1 M Fe-free KOH and measured in the same solutions. Normalization was done using 1.2e/Ni for determining nmol of Ni in (B). Number of mole of Ni is calculated from post-Tafel measurements.....56

3.17: Cyclic Voltammograms acquired at 10 mV/s, between the same scan limits as in Figure 3.9, showing the region of the redox peaks and onset of oxygen evolution for NiO_xH_y)_{100mC} in unpurified 1 M KOH (i) and in Fe-free 1 M KOH (ii) as-deposited (blue) and after-Tafel measurements (green).....57

3.18: Cyclic Voltammograms for NiO_xH_y)_{1mC} as (a) a first scan for the as-deposited film in 1 M Fe-free KOH, (b) a second scan after the film was moved to 1 M KOH, (c) after anodization in 1 M KOH, (d) after the anodized film was moved back into Fe-free KOH, and (e) scans acquired in Fe-free KOH after increments of 10 CVs were taken at 100 mV/s in this solution, this was repeated 6 times; some of the CVs are shown. Scan rate is 10 mV/s.....60

3.19: Cyclic Voltammograms for NiO_xH_y)_{10mC} as (a) a first scan for the as-deposited film in 1 M Fe-free KOH, (b) a second scan after the film was moved to 1 M KOH, (c) after anodization in 1 M KOH, (d) after the anodized film was moved back into Fe-free KOH, and (e) scans acquired in Fe-free KOH after increments of 10 CVs were taken at 100 mV/s in this solution, this was repeated 25 times; some of the CVs are shown. Scan rate is 10 mV/s.....61

3.20: Cyclic voltammograms for $\text{Ni}_{0.6}\text{Fe}_{0.4}\text{O}_x\text{H}_y$)_{10mC} as follows: a) a first CV for the as-deposited film in 1 M Fe-free KOH, b) a second CV after the film was moved to 1 M KOH, c) CV after anodization in 1 M KOH, d) CV of anodized film moved back into 1 M Fe-free KOH, and e) CVs acquired in 1 M Fe-free KOH after increments of 10 CVs were taken at 100 mV/s in this solution, this was repeated 25 times, some of the CVs are shown. Scan rate is 10 mV/s.....62

3.21: Cyclic voltammograms of FTO in 1 M KOH (A) and 1 M Fe-free KOH (B) as a first scan (CV₁ blue) and then CVs acquired after 10 CVs were taken at 100 mV/s, repeated 6 times in the same solution. Scan rate of all CVs in this figure is 10 mV/s. The number of CVs (10-60) refers to the total number of scans acquired at 100 mV/s.....66

3.22: Cyclic voltammograms of NiO_xH_y)_{1mC} film after the addition of 1.2 nmol Fe³⁺ and three scans in 1 M Fe-free KOH. CVs as first and third scan after anodic conditioning in the same solution were acquired. 10 CVs were taken at 100 mV/s in the same solution followed by a CV at 10 mV/s; this was repeated 2 times. Scan rate for the CVs in this figure is 10 mV/s. The number of CVs (10-20) refers to the total number of scans acquired at 100 mV/s.....67

3.23: Cyclic voltammograms of NiO_xH_y)_{1mC} film as a first scan in 1 M Fe-free KOH before and immediately after addition of 2.4 nmol Fe^{3+} . 10 CVs were acquired at 100 mV/s in the same solution followed by a CV at 10 mV/s; this was repeated 6 times (A). A CV was acquired immediately before and after the addition of a total of 21 nmol Fe^{3+} . 10 CVs were acquired at 100 mV/s followed by a CV at 10 mV/s; this repeated 6 times (B). Scan rate for the CVs in this figure is 10 mV/s. The inset shows the anodic shift in $\text{Ni}(\text{OH})_2/\text{NiOOH}$ redox peaks. The number of CVs (10-60) refers to the total number of scans acquired at 100 mV/s.....68

3.24: Cyclic voltammograms of NiO_xH_y)_{100mC} film in 1 M Fe-free KOH after addition of 2.4 nmol Fe^{3+} and 60 CVs at 100 mV/s were acquired. A CV was acquired after the addition of a total of 8 nmol Fe^{3+} . Similarly, 10 CVs were acquired at 100 mV/s followed by a CV at 10 mV/s; this was repeated 6 times. A CV after anodization was taken followed by 10 CVs at 100 mV/s and a CV at 10 mV/s; this was repeated 2 times. Scan rate for the CVs in this figure is 10 mV/s. The inset shows the slight anodic shift in $\text{Ni}(\text{OH})_2/\text{NiOOH}$ redox peaks post Fe^{3+} addition and anodic conditioning. The number of CVs (10-60) refers to the total number of scans acquired at 100 mV/s.....69

3.25: CVs of NiO_xH_y)_{1mC} in unpurified (and aerated) 1 M KOH after 10 CVs at 100 mV/s immediately before (a, blue) and after the addition of 8 μM K_2PtCl_4 (b, red), and then after 20 CVs at 100 mV/s (c, green) showing the usual anodic shift and splitting of the peaks (A). A CV scan from -1.5 V to 1 V before (a, blue) and after the addition of 8 μM K_2PtCl_4 (b, red), note that there are 40 CVs at 100 mV/s between these two CVs hence the anodic shift in the peaks (B). Scan rate is 10 mV/s.....71

4.1: Cyclic voltammograms of Ni-Bi)_{1mC} film in 1 M KBi, as a first (CV₁ blue) and second scan (CV₂ orange) and CVs acquired after 10 CVs were taken at 100 mV/s, repeated 6 times in the same solution. Scan rate of all CVs in this figure is 10 mV/s. The inset shows the $\text{Ni}(\text{OH})_2/\text{NiOOH}$ redox peaks and onset of oxygen evolution. The number of CVs (10-60) refers to the total number of scans acquired at 100 mV/s.....79

4.2: Cyclic voltammograms of Ni-Bi)_{1mC} film in 1 M KBi, as a first scan (CV₁ blue), a second scan after 0.01 mM (A), 0.08 mM (B) and 0.32 mM (C) Al^{3+} addition (orange) and CVs acquired after 10 CVs were taken at 100 mV/s, repeated 6 times in the same solution. Scan rate of all CVs in this figure is 10 mV/s. The inset shows the $\text{Ni}(\text{OH})_2/\text{NiOOH}$ redox peaks and onset of oxygen evolution. The number of CVs (10-60) refers to the total number of scans acquired at 100 mV/s.....80

4.3: Cyclic voltammograms of NiO_xH_y)_{1mC} film in 1 M KOH, as a first scan (CV₁ blue), after the addition of 0.16 mM Al^{3+} (CV₂ orange) and CVs acquired after 10 CVs were taken at 100 mV/s, repeated 6 times in the same solution. Scan rate of all CVs in this figure is 10 mV/s. The inset shows the $\text{Ni}(\text{OH})_2/\text{NiOOH}$ redox peaks and onset of oxygen evolution. The number of CVs (10-60) refers to the total number of scans acquired at 100 mV/s.....83

4.4: Cyclic voltammograms of NiO_xH_y)_{1mC} film in 1 M Fe-free KOH, as a first scan (CV₁ blue), after the addition of 0.16 mM Al^{3+} (CV₂ orange) and CVs acquired after 10 CVs were taken at 100 mV/s, repeated 6 times in the same solution. Scan rate of all CVs in this figure is 10 mV/s. The inset shows the $\text{Ni}(\text{OH})_2/\text{NiOOH}$ redox peaks and onset

of oxygen evolution. The number of CVs (10-60) refers to the total number of scans acquired at 100 mV/s.....	85
4.5: Cyclic voltammograms in 1 M KBi at Ni-Bi) _{1mC} (A) and Ni _{0.6} Al _{0.4} -Bi) _{1mC} (B) as a first scan (a, blue) and after anodic conditioning in the same solution (b, red). The insets show the corresponding redox peaks and onset of oxygen evolution for the three scans shown. Scan rate is 10 mV/s.....	89
4.6: Anodization plot (i-t plot) of an ultra-thin Ni _{0.6} Al _{0.4} -Bi) _{1mC} film biased at 0.903 V vs. Ag/AgCl in 1 M KBi.....	92
4.7: Tafel plots (A) and normalized Tafel plots (B) for Ni-Bi) _{1mC} (red, orange and brown; ▲) and Ni _{0.6} Al _{0.4} -Bi) _{1mC} (blue, green and purple; ■) anodized in 1 M KBi and measured in the same solution with the corresponding slopes for the best fit linear plot.....	93
4.8: Cyclic voltammograms in 1 M Fe-free KOH at Ni _{0.6} Al _{0.4} O _x H _y) _{1mC} as a first scan (a, blue), after anodic conditioning in the same solution (b, red) and after Tafel measurements (c, green). The insets show the corresponding redox peaks and onset of oxygen evolution for the three scans shown. Scan rate is 10 mV/s.....	97
4.9: Normalized cyclic voltammograms, I/n (mA/nmol) vs. η (V), at Ni _{0.6} Al _{0.4} O _x H _y) _{1mC} (a, blue) and NiO _x H _y) _{1mC} (b, orange) films in 1 M Fe-free KOH as a first scan. The inset shows the Ni(OH) ₂ /NiOOH redox peaks and onset of oxygen evolution. Scan rate is 10 mV/s.....	100
4.10: Cyclic voltammograms of Ni _{0.6} Al _{0.4} O _x H _y) _{1mC} film in 1 M Fe-free KOH, as a first scan (CV ₁ blue) and CVs acquired after 10 CVs were taken at 100 mV/s, repeated 6 times in the same solution. Scan rate of all CVs in this figure is 10 mV/s. The inset shows the Ni(OH) ₂ /NiOOH redox peaks and onset of oxygen evolution. The number of CVs (10-60) refers to the total number of scans acquired at 100 mV/s.....	101
4.11: Tafel plots (A), overpotential η (mV) versus log(J (A/cm ²)), and normalized Tafel plots (B), overpotential η (mV) versus log(I/n (A/nmol)), for two NiO _x H _y) _{1mC} (red, orange; ▲) and two Ni _{0.6} Al _{0.4} O _x H _y) _{1mC} (green, blue; ■) films anodized in 1 M Fe-free KOH and measured in the same solution with the corresponding slopes for the best fit linear plot.....	102
4.12: Cyclic voltammograms in 1 M KOH at Ni _{0.6} Al _{0.4} O _x H _y) _{1mC} as a first scan (a, blue), after anodic conditioning in the same solution (b, red) and after Tafel measurements (c, green). The insets show the corresponding redox peaks and onset of oxygen evolution for the three scans shown. Scan rate is 10 mV/s.....	106
4.13: Anodization plots (i-t plots) of ultra-thin Ni _{0.6} Al _{0.4} O _x H _y) _{1mC} films biased at 0.58 V vs. Hg/HgO in 1 M Fe-free KOH (a, red traces) or unpurified 1 M KOH (b, blue traces) as indicated.....	107
4.14: Cyclic voltammograms of Ni _{0.6} Al _{0.4} O _x H _y) _{1mC} film in 1 M KOH, as a first scan (CV ₁ blue) and CVs acquired after 10 CVs were taken at 100 mV/s, repeated 6 times in	

the same solution. Scan rate of all CVs in this figure is 10 mV/s. The inset shows the Ni(OH) ₂ /NiOOH redox peaks and onset of oxygen evolution. The number of CVs (10-60) refers to the total number of scans acquired at 100 mV/s.....	109
4.15: Tafel plots (A), overpotential η (mV) versus $\log(J \text{ (A/cm}^2\text{)})$, and normalized Tafel plots (B), overpotential η (mV) versus $\log(I/n \text{ (A/nmol)})$, for NiO _x H _y) _{1mC} (red, orange; ▲) and Ni _{0.6} Al _{0.4} O _x H _y) _{1mC} (green, blue; ■) anodized in 1 M KOH and measured in the same solution with the corresponding slopes for the best fit linear plot.....	110
4.16: SEM images of Ni _{0.6} Al _{0.4} O _x H _y) _{400mC} deposited by passing a charge of 400 mC/cm ² on FTO: as-deposited (A) and after anodic conditioning in 1 M KOH (B).....	113
4.17: EDX spectrum of as-deposited Ni _{0.6} Al _{0.4} O _x H _y) _{400mC} showing both Ni and Al peaks.....	113
4.18: Cyclic voltammograms in 1 M Fe-free KOH at Ni _{0.6} Al _{0.4} O _x H _y) _{100mC} as a first scan (a, blue), after anodic conditioning in the same solution (b, red) and after Tafel measurements (c, green). The insets show the corresponding redox peaks and onset of oxygen evolution for the three scans shown. Scan rate is 10 mV/s.....	115
4.19: Cyclic voltammograms in 1 M KOH at Ni _{0.6} Al _{0.4} O _x H _y) _{100mC} as a first scan (a, blue), after anodic conditioning in the same solution (b, red) and after Tafel measurements (c, green). The insets show the corresponding redox peaks and onset of oxygen evolution for the three scans shown. Scan rate is 10 mV/s.....	117
4.20: Anodization plots (i-t plots) of ultra-thin Ni _{0.6} Al _{0.4} O _x H _y) _{100mC} films biased at 0.58 V vs. Hg/HgO in 1 M Fe-free KOH (a, red traces) or unpurified 1 M KOH (b, blue traces) as indicated.....	119
4.21: Tafel plots (A, C) and normalized Tafel plots (B, D) for NiO _x H _y) _{100mC} (red, orange, brown; ▲) and Ni _{0.6} Al _{0.4} O _x H _y) _{100mC} (green, blue; ■) anodized in 1 M Fe-free KOH (A, B) and 1 M KOH (C, D) and measured in the same solution with the corresponding slopes for the best fit linear plot.....	121
4.22: Tafel plots (A, C) and normalized Tafel plots (B, D) for NiO _x H _y) _{100mC} (red ▲), Ni _{0.6} Al _{0.4} O _x H _y) _{100mC} (green ■), NiO _x H _y) _{1mC} (orange ▲) and Ni _{0.6} Al _{0.4} O _x H _y) _{1mC} (blue ■) anodized in 1 M Fe-free KOH (A, B) and 1 M KOH (C, D) and measured in the same solution with the corresponding slopes for the best fit linear plot.....	122
4.23: Cyclic voltammograms of Ni _{0.6} Al _{0.4} O _x H _y) _{100mC} film in 1 M Fe-free KOH (A) and 1 M KOH (B), as a first (CV ₁ blue) and second (CV ₂ orange) scan and CVs acquired after 10 CVs were taken at 100 mV/s, repeated 6 times in the same solution. Scan rate of all CVs in this figure is 10 mV/s. The inset shows the Ni(OH) ₂ /NiOOH redox peaks and onset of oxygen evolution. The number of CVs (10-60) refers to the total number of scans acquired at 100 mV/s.....	125

TABLES

Table	Page
4.1: Average cathodic peak charge, number of moles of active Ni, thickness and monolayer equivalence of Ni(OH) ₂ for as-deposited and anodized Ni-Bi) _{1mC} and Ni _{0.6} Al _{0.4} -Bi) _{1mC} films measured in 1 M KBi.....	88
4.2: Average anodic and cathodic peak positions, peak separation and half-wave potentials for as-deposited and anodized Ni-Bi) _{1mC} , Ni _{0.6} Al _{0.4} -Bi) _{1mC} and Ni _{0.4} Al _{0.6} -Bi) _{1mC} films measured in 1 M KBi. E _p and E _{1/2} values are reported vs. Ag/AgCl.....	90
4.3: Average Tafel slope, apparent TOF for O ₂ per second per Ni center calculated at an overpotential of ~ 400 mV from steady-state current measurements under stirring for as-deposited and anodized Ni-Bi) _{1mC} and Ni _{0.6} Al _{0.4} -Bi) _{1mC} films measured in 1 M KBi....	94
4.4: Average cathodic peak charge, number of moles of active Ni, thickness and monolayer equivalence of Ni(OH) ₂ for as-deposited, anodized and after Tafel NiO _x H _y) _{1mC} and Ni _{0.6} Al _{0.4} O _x H _y) _{1mC} films measured in 1 M Fe-free KOH.....	96
4.5: Average anodic and cathodic peak positions, peak separation and half-wave potentials for as-deposited, anodized and after Tafel NiO _x H _y) _{1mC} and Ni _{0.6} Al _{0.4} O _x H _y) _{1mC} films measured in 1 M Fe-free KOH. E _p and E _{1/2} values are reported vs. Hg/HgO.....	99
4.6: Average Tafel slope, apparent TOF for O ₂ per second per Ni center calculated at an overpotential of ~ 400 mV from steady-state current measurements under stirring for as-deposited and anodized NiO _x H _y) _{1mC} and Ni _{0.6} Al _{0.4} O _x H _y) _{1mC} films measured in 1 M Fe-free KOH.....	104
4.7: Average cathodic peak charge, number of moles of active Ni, thickness and monolayer equivalence of Ni(OH) ₂ for as-deposited and anodized NiO _x H _y) _{1mC} and Ni _{0.6} Al _{0.4} O _x H _y) _{1mC} films measured in 1 M KOH.....	105
4.8: Average anodic and cathodic peak positions, peak separation and half-wave potentials for as-deposited, anodized and after Tafel NiO _x H _y) _{1mC} and Ni _{0.6} Al _{0.4} O _x H _y) _{1mC} films measured in 1 M KOH. E _p and E _{1/2} values are reported vs. Hg/HgO.....	108
4.9: Average Tafel slope, apparent TOF for O ₂ per second per Ni center calculated at an overpotential of ~ 300 mV from steady-state current measurements under stirring for as-deposited and anodized NiO _x H _y) _{1mC} and Ni _{0.6} Al _{0.4} O _x H _y) _{1mC} films measured in 1 M KOH.....	111
4.10: Average cathodic peak charge, number of moles of active Ni, thickness and monolayer equivalence of Ni(OH) ₂ for as-deposited, anodized and after Tafel NiO _x H _y) _{100mC} and Ni _{0.6} Al _{0.4} O _x H _y) _{100mC} films measured in 1 M Fe-free KOH.....	114
4.11: Average anodic and cathodic peak positions, peak separation and half-wave potentials for as-deposited, anodized and after Tafel NiO _x H _y) _{100mC} and	

Ni _{0.6} Al _{0.4} O _x H _y) _{100mC} films measured in 1 M Fe-free KOH. E _p and E _{1/2} values are reported vs. Hg/HgO.....	116
4.12: Average cathodic peak charge, number of moles of active Ni, thickness and monolayer equivalence of Ni(OH) ₂ for as-deposited, anodized and after Tafel NiO _x H _y) _{100mC} and Ni _{0.6} Al _{0.4} O _x H _y) _{100mC} films measured in 1 M KOH.....	117
4.13: Average anodic and cathodic peak positions, peak separation and half-wave potentials for as-deposited, anodized and after Tafel NiO _x H _y) _{100mC} and Ni _{0.6} Al _{0.4} O _x H _y) _{100mC} films measured in 1 M KOH. E _p and E _{1/2} values are reported vs. Hg/HgO.....	119
4.14: Average Tafel slope, apparent TOF for O ₂ per second per Ni center calculated at an overpotential of ~ 400 mV from steady-state current measurements under stirring for as-deposited and anodized NiO _x H _y) _{100mC} and Ni _{0.6} Al _{0.4} O _x H _y) _{100mC} films measured in 1 M Fe-free KOH (A) and 1 M KOH (B).....	123

CHAPTER I

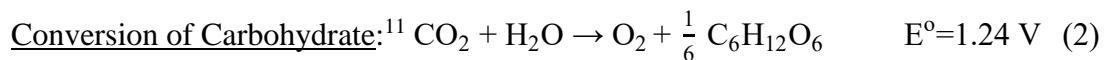
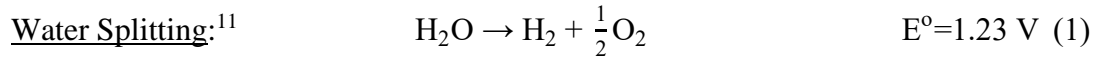
INTRODUCTION

A. Water Splitting

The global use of energy has been exponentially increasing with an estimated projection of 30 TW global power need by 2050.² A high reliance on fossil fuels is still required to meet this demand despite its detrimental effect on the environment. Thus, the movement towards green carbon-neutral energy sources is needed for the future of the planet. The sun constitutes the largest decentralized and inexhaustible source of green energy with one hour of solar energy outweighing the global energy consumption per year³ and one second of solar power hitting the surface of the earth corresponding to 130 million 500 MW power plants.⁴ However, the sporadic nature of solar energy due to diurnal and seasonal cycles limits its usage and yield and pushes towards the need for the storage of harvested solar energy. This has driven researchers to study photodriven water splitting: the generation of H₂ and O₂ from water to store energy in a chemical bond using solar energy mimicking photosynthesis.^{1-2, 5-7}

Hydrogen is a notable green fuel as it can be sustainably generated from water splitting and produces heat, when combusted with oxygen, or electricity, when oxidized in a fuel cell, while only yielding water as a product.⁸ However, 96% of current hydrogen production is from fossil fuels.⁸ Hydrogen fuel cells have their pros, such as higher volumetric energy density and long-term storage capability of fuel cells in comparison to commercial batteries, mainly due to the absence of self-discharge, and cons, such as its low efficiency with respect to commercial batteries.⁸

Scientists as early as 1912 and before have pondered upon the use of photochemical reactions performed by plants to properly harvest and store solar energy.⁹ Photosynthesis is the widely known reaction through which plants harvest solar energy to convert water to oxygen and hydrogen with the latter combining with carbon dioxide to store energy in the form of carbohydrates.¹⁰



Photosystem II (PSII), a specialized protein complex in the thylakoid membrane of photosynthetic species, absorbs solar energy and produces an excited electron which moves to Photosystem I (PSI) using redox-active cofactors.¹¹ This then produces a hole in PSII which moves to the oxygen evolving complex (OEC), a Mn_4Ca cubic cluster, triggering the water splitting reaction and producing O_2 and protons as per the Kok cycle.¹¹ The protons are then reduced using the electrons and ferredoxin-NADP⁺ reductase to generate hydrogen in the form of NADPH, via NADP⁺ reduction, thus storing the solar energy.¹²

Water splitting is a thermodynamically unfavored reaction described as an “uphill reaction” due to the increase in Gibbs free energy by 237 kJ/mol.¹³ Solar water splitting cells have been researched to simultaneously drive both oxygen and hydrogen evolution reactions using solar energy absorbed by semiconductors based on the pioneering research of Honda and Fujishima on TiO_2 photoelectrochemistry.¹⁴ Both half reactions, oxygen and hydrogen evolution, are sluggish and require electrocatalysts to be coupled to the semiconductor. There are three main solar water splitting systems:

- 1) Photochemical (PC): Photocatalysts are used to split water into O_2 and H_2 gas under UV or visible light illumination.¹⁵ Semiconductors need a band gap equal

to or above + 1.23 V vs. normal hydrogen electrode (NHE) to excite electrons in its conduction band and generate holes in its valence band driving water reduction and oxidation when irradiated with photons.¹⁶ Metal oxides and chalcogenides, such as TiO₂ and CdS, are well-known and common water splitting photocatalysts.^{14, 16}

- 2) Photoelectrochemical (PEC): This system is formed by a semiconductor, functioning as a photoanode for water oxidation or a photocathode for water reduction, and a metallic counter electrode (such as Pt).¹⁷ Light is absorbed by the photoelectrodes and electrons are excited to the conduction band leaving holes in the valence band.¹⁸ The incoming photon energy should be greater than the band-gap energy of the semiconductor (1.6 eV to overcome the thermodynamic barriers of water splitting and charge recombination potential losses).¹⁸ Charge carriers are then separated and transported to the electrode surface through the semiconductor.¹⁸ Finally, water from the aqueous electrolyte is oxidized to O₂ using the holes at the photoanode surface and is reduced to H₂ by the electrons at the photocathode surface.¹⁸ The opposite reaction occurs at the counter electrode.¹⁸ The first PEC cell was made by Honda and Fujishima and composed of a TiO₂ photoanode and Pt counter electrode.¹⁴ Recently, WO₃ and BiVO₄ doped with metal cations, such as Mo, have proven to be promising photoanodes.¹⁶
- 3) Photovoltaic-Electrolysis (PV-E): This system is formed by connecting a photovoltaic cell (solar cell) to a water electrolyzer (or two electrolyzers, a cathode and an anode for HER and OER, respectively).¹⁷ The PV converts solar

energy to electrical energy. The photogenerated current is transferred, usually via the circuit wires, to the electrolyzer to be used for water electrolysis.

To enhance the proposed system, work has been focused on searching and optimizing materials of suitable band gaps and light harvesting capabilities to push fast electron transfer, stability and high chemical-to-solar energy conversion efficiency (known as STH, solar-to-hydrogen efficiency). Moreover, coupling of electrocatalysts to photoelectrodes has been in development to overcome the slow water splitting reaction kinetics while maintaining stability and efficiency.

B. Oxygen Evolution Reaction

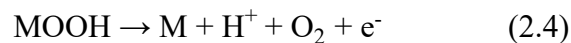
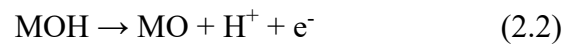
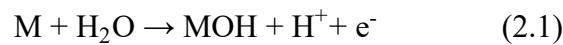
The discovery of water splitting reactions can be traced back to as early as 1789 with Paets van Troostwijk and Deiman performing water electrolysis using gold wires submerged in water connected to an electrostatic generator.¹⁹⁻²⁰ However, industrialization of water electrolysis only came during the 1900s to produce hydrogen gas.²¹ This was accompanied by a rise in scientific interest to increase the efficiency of this reaction and thus pushing researchers to study its reactivity and catalysis.¹⁹⁻²⁰ Electrochemical water splitting is made up of two main reactions: reduction of water into hydrogen (H₂) at the cathode, hydrogen evolution reaction (HER), and oxidation of water into oxygen (O₂) at the anode, oxygen evolution reaction (OER).

HER: $2\text{H}^+ + 2\text{e}^- \rightarrow \text{H}_2$ in **acid** ($E^\circ = 0 \text{ V}$), and $2\text{H}_2\text{O} + 2\text{e}^- \rightarrow \text{H}_2 + 2\text{OH}^-$ in **alkaline** ($E^\circ = -0.83 \text{ V}$).²²

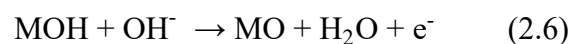
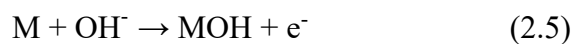
OER: $2\text{H}_2\text{O} \rightarrow \text{O}_2 + 4\text{H}^+ + 4\text{e}^-$ in **acid** ($E^\circ = 1.23 \text{ V}$), and $4\text{OH}^- \rightarrow \text{O}_2 + \text{H}_2\text{O} + 4\text{e}^-$ in **alkaline** ($E^\circ = -0.40 \text{ V}$).²²

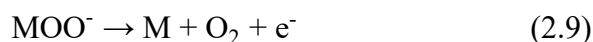
Four electrons and four protons as well as 1.23 V per transferred electron (4.92 eV overall) are required to form one dioxygen molecule from two water molecules making the oxygen evolution reaction kinetically sluggish.^{2, 23-24} Thus, demanding catalysts to fasten these processes are necessary to reduce activation overpotential. Several studies have been done over the years to find efficient electrocatalysts of high stability and activity for OER and thus producing a large amount of oxygen at the lowest possible overpotential while experiencing minimal dissolution and corrosion during its use.²⁵ Metal-based oxide catalysts have shown promising activity and stability and are categorized into noble and non-noble metal-based electrocatalysts.

Proposed OER mechanisms differ based on the pH of electrolyte in which the reaction takes place as well as the nature of the catalyst used and its active sites. Nonetheless, general mechanisms can be laid out but differ slightly in the literature.²²⁻²³ A major common characteristic is the description of OER as a heterogeneous reaction with the bonding in the intermediates (MOH, MO, MOOH) between the electrocatalyst (M) and the oxygen atom (forming M-O) being an important factor in the activity of the catalyst.²² A proposed mechanism in acid medium, based on DFT-predicted peroxide path, is as follows, where M represents the surface site:²⁶



Its counterpart in alkaline medium, assuming a single-site mechanism, is:²⁷





Recent studies are combining the use of experimental data, such as the electrochemical behavior of the redox couple, Tafel plot analysis of the catalyst, and DFT calculations to better understand the OER mechanism and thus better design electrocatalysts of higher efficiency.

Generally, the mechanism behind OER electrocatalyst activity is still under debate. Rossmeisl et al. reported that when OER occurs, an oxide layer forms on the metal surface and for this layer to be stable, a high potential should be applied.²⁸ Trasatti et al. proposed that OER activity depends on the strength of the metal-oxygen bond at the active sites and the interaction between oxide and intermediate²⁹ which was later supported with DFT studies modeling the energetics of the reaction.²³ The electrocatalyst surface active sites act as adsorbents to OER intermediates and thus assist in the charge transfer between the intermediates and the electrode.²²

To properly evaluate the efficiency and kinetics of the electrocatalyst, two main electrochemical parameters are evaluated.²² The first parameter is the overpotential (η) which is the potential applied over the equilibrium potential to drive the OER and is expressed as $\eta = E - E_{eq}$, where E is the applied potential and E_{eq} is the equilibrium potential.²² An electrocatalyst is deemed more efficient and active when it needs a lower overpotential to produce a specific current density. The overpotential at 10 mA/cm² is used as a benchmarking tool since it corresponds to the approximate current density at a solar water splitting cell anode operating at 10% efficiency.³⁰ The second parameter is the Tafel slope, specifically the Tafel slope which is generally governed by the

following equation derived from the Butler-Volmer equation: $\log(j) = \log(j_0) + \eta/b$ where b is the Tafel slope, j is the current density and j_0 is the exchange current density.²² Thus, the slope here expresses the rate at which the current changes versus the overpotential, i.e. a smaller slope indicates a faster increase in current density with less overpotential applied and thus a different rate determining step. The Tafel slope also gives insight on the mechanism of the reaction whereby a small slope is related to the rate-determining step occurring towards the end of the multiple electron transfer reactions.²²

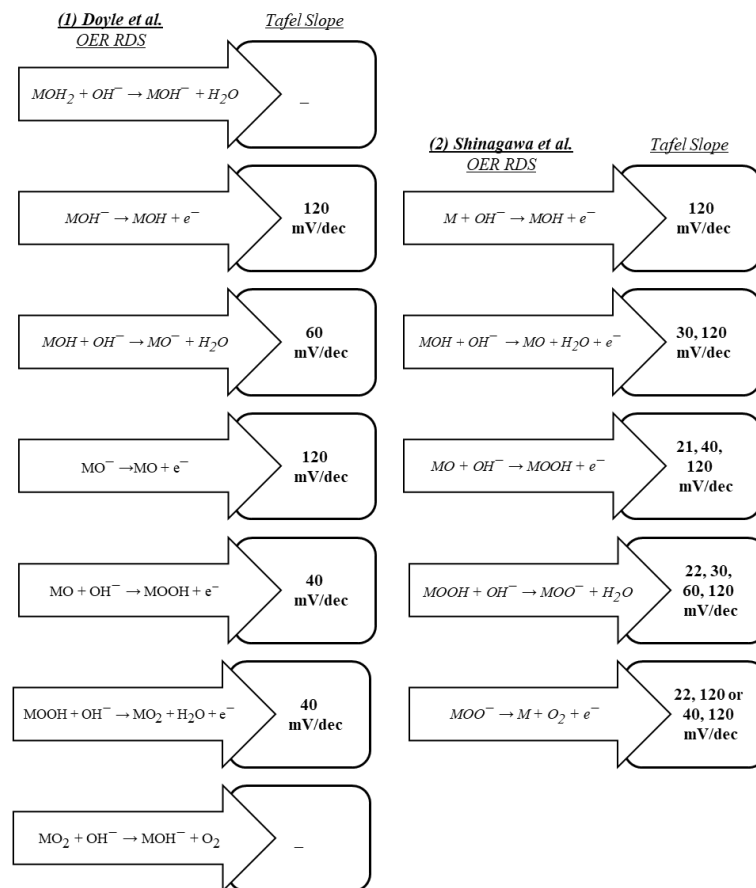


Figure 1.1: Modelled Tafel slopes and their corresponding rate-determining steps based on the work of Doyle et al. and Shinagawa et al.^{22, 27, 31} “-” represents an unreported Tafel slope.

Generally, when the rate-determining step is the first step of OER, a one electron process, the resulting Tafel slope would be 120 mV/dec.³² When it is the second step, then it would lead to a Tafel slope of 60 mV/dec if it is a chemical transformation and 40 mV/dec if it is an electron-proton reaction and thus involves a second electron transfer.³² Thus, a trend in Tafel slopes of OER electrocatalysts can be traced out with common values of 30 mV/dec, 40 mV/dec, 60 mV/dec and 120 mV/dec, each corresponding to a specific rate-determining step in the proposed OER mechanism.^{22, 27, 31} Figure 1.1 shows Tafel slopes and their predicted rate-determining steps based on the two proposed mechanisms by Doyle et al.³¹ and Shinagawa et. al.²⁷ However, due to the complicated nature of OER, the Tafel slope and its rate-determining step may not be accurately predicted and analyses of the mechanism should not only be based on these values.²² Shinagawa et al. proposed that Tafel slopes vary for the same rate-determining steps depending on the coverage of intermediates on the surface of the electrocatalyst.²⁷ The Tafel slope decreases as the rate-determining step is towards the end of the reactions classifying the catalyst as efficient.²²

C. Precious Metal Based OER Electrocatalysts

The main factor in any catalysis is the material which the catalyst is formed of. The latter dictates the type of catalytic active sites and the nature of its interaction with the reactants. Early survey studies have shown that rare metal oxides, such as RuO₂ in alkaline media and IrO₂ in acidic media, have demonstrated high OER catalytic efficiency in comparison to non-precious metals.^{23, 28-29, 33-39} Volcano type activity plots for OER in alkaline and acid electrolytes show RuO₂ and IrO₂ as the most active OER catalysts based on their DFT-predicted binding energy to surface oxygen species (OER

intermediates)^{23, 28-29} as seen in Figure 1.2. The plot relates the overpotential at low current density (lower than 1 mA/cm²) to the standard enthalpy of lower-to-higher oxide transition.^{23, 29} At the ascending portion, as the strength of the oxide-intermediate interaction increases, the OER overpotential decreases. While at the descending portion, as the absorbed intermediate coverage increases (due to the easily oxidized material), the overpotential increases.^{23, 29} The catalytic activity depends on the particle size⁴⁰⁻⁴² and crystal structure of the OER catalyst.⁴²⁻⁴³

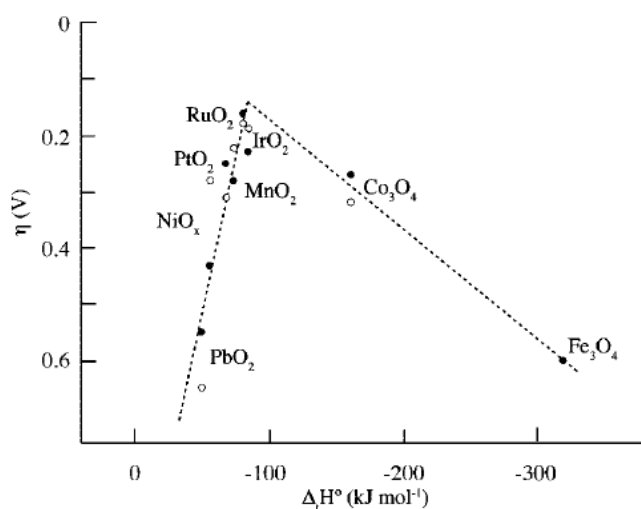


Figure 1.2: Volcano relation OER plot showing the electrocatalytic activity in acid as closed circles and in alkaline as open circles. Figure used with permission from ACS; *Chemical Reviews* **2010** 110 (11), 6446-

6473, <https://pubs.acs.org/doi/10.1021/cr1002326>.²⁹ Further permissions related to the material excerpted should be directed to ACS.

Ru-based catalysts were found to be more active than other precious metals, such as Ir, Pt and Pd, possibly due to their ideal medium bonding strength to OER intermediates.^{28, 44-45} Generally, metallic catalysts tend to be more OER active than their

oxide derivatives but suffer from low stability with a general activity of $\text{Ru} > \text{Ir} \approx \text{RuO}_2 > \text{IrO}_2$ and dissolution trend of $\text{Ru} \gg \text{Ir} > \text{RuO}_2 \gg \text{IrO}_2$, independent of the electrolyte.⁴⁶ In alkaline, RuO_x and IrO_x have shown significant catalytic activity but lack stability due to surface oxidation and leaching of the catalyst.³⁰ Studies have shown that increased OER activity and stability in noble metals and their oxides in both acidic and alkaline media is achieved with nanoscaling, use of nanoparticle catalysts over bulk, specifically Ir-based electrodes, due to increased surface area and catalytic edge sites.^{44, 47-49} Another method to combat the low stability of monometallic catalysts is the use of bimetallic Ru and Ir based electrodes.^{25, 50-54} However, earlier work has initially struggled to obtain higher activity and prolonged stability with bimetallic catalysts over their monometallic counterparts^{51, 55-58} until recently.⁵⁹⁻⁶⁰

Noble metals have exhibited higher catalytic activity and efficiency over non-noble metals as OER catalysts in acidic medium due to their stability and lower corrosion in the latter.³⁰ This in turn makes them the leading candidate for use in polymer electrolyte membrane (PEM) electrolyzers which use acidic electrolytes.²⁵ Though also OER active in alkaline medium, noble metals are generally more efficient and stable in acidic medium unlike non-noble metals.^{24, 44, 46}

D. Non-Precious Metal Based OER Electrocatalysts

1. Types of Non-Precious Metal Based OER Electrocatalysts

The use of precious metals as OER electrocatalysts has shown several disadvantages especially in alkaline electrolyte ranging from low stability to high production cost. Thus, research shifted its focus onto non-precious transition metals as they are cheaper and in some cases, have comparable stability and OER activity in

alkaline media.²² Several structures of transition metals were found to exhibit significant OER activity such as perovskites, spinels, pyrochlores, oxides, hydroxides, oxyhydroxides, and recently, chalcogens and layered double hydroxide (LDH).^{22, 24, 61-69}

Briefly, perovskites are of general formula ABO_3 where A is an alkaline/precious metal and B is a transition metal with the latter as the center of the octahedron and A filling in the spaces to complete the structure.²² Using this system, researchers ordered OER electrocatalytic activity based on the nature of B: $Ni > Co > Fe > Mn > Cr$, showing Tafel slopes of 40 mV/dec for Ni, 60 mV/dec for Co and 120 mV/dec for Fe and Mn based catalysts.⁶⁹ B-OH bond strength highly influenced electrocatalytic activity with moderate strength as seen in Ni and Co showing the highest efficiency.^{22, 70} This can be generalized for all OER metal-based catalysts.²² Spinel is of general formula AB_2O_4 where A and B are either alkaline earth, group 13 (boron group) or first-row transition metals with the latter occupying a tetrahedral or octahedral orientation.⁷¹ These systems exhibit good conductivity and stability in alkaline and thus are promising OER electrocatalysts.²² Bimetallic oxides offer greater activity due to the varying effects of the secondary metal ion inducing electronic changes in the catalyst and thus allowing enhanced bonding with OER intermediates.⁷² Recent studies have found that spinel metal oxides structurally transform into metal hydroxides at the surface.⁷³⁻⁷⁴

Layer structure oxides, namely hydroxides $M(OH)_2$ and oxyhydroxides $MOOH$ (M is a transition metal), are promising OER electrocatalysts with reasonable conductivity, stability and activity.²² Structurally, a layer is formed of the transition metal centering an octahedron with an oxygen anion at each corner ($[MO_6]$), and cations

(such as H^+ or alkali metals, Na^+ and K^+) or water intercalated in between each layer.²² This forms a structure better known as layered double hydroxides (LDH).²² Similar to prevooskites, the general activity trend based on the nature of the transition metal is the same with Ni showing the highest efficiency.⁶²

2. Ni-oxo/hydroxide OER Electrocatalysts

a. Structure

Studies on the structure and electrochemistry of Ni-based oxides and layered oxides date back to as early as the 1950s as they were used in battery technology and various applications in chemistry, physics and engineering.⁷⁵⁻⁷⁶ Nickel hydroxides and oxyhydroxides, generally termed NiO_xH_y , showed promising results as OER catalysts in alkaline electrolyte due to their high activity coupled with stability, abundance and relatively low costs.^{22, 77} Their catalytic activity was attributed to the ideal bonding strength of the Ni-OH bond according to Sabatier's principle as seen in spinel metal oxides.²² Ni in $Ni(OH)_2$ is in an oxidation state of +2, stable in alkaline media, and undergoes oxidation with the onset of OER to reach +3 or higher in some cases (+3-4) and form $NiOOH$ as per the following equation: $Ni(OH)_2 + OH^- \rightarrow NiOOH + H_2O + e^-$.⁷⁷⁻⁷⁸ Both phases are arranged in layers of shared edges forming octahedra with Ni as the center and O/OH groups at its vertices.⁷⁸

Bode et al. proposed a diagram in 1966 that would be used to this day as a basis of nickel hydroxide phase analysis.⁷⁹ They reported the electrochemical behavior of two phases of nickel hydroxide upon their redox transformations with charging, discharging, aging and overcharging in alkaline solution.^{76, 79-80} Two forms of $Ni(OH)_2$ are present: α - $Ni(OH)_2$ and β - $Ni(OH)_2$ with redox couples: α - $Ni(OH)_2/\gamma$ - $NiOOH$ of greater

reversibility and average Ni oxidation states of ~ 2 and 3.5 - 3.6 , respectively, and β -Ni(OH)₂/ β -NiOOH of greater reported OER activity and average Ni oxidation states of ~ 2 and 3 , respectively.^{76, 80} Hydrated disordered α -Ni(OH)₂ transforms into dehydrated crystalline β -Ni(OH)₂ with aging in water or alkaline medium^{76, 80}. α -Ni(OH)₂ contains intercalated anions in its lattice which it exchanges for hydroxyl ions in alkaline solution.⁸¹ β -NiOOH transforms into γ -NiOOH with overcharging and reverts back to β -NiOOH at low bias or directly reduces into β -Ni(OH)₂.⁷⁸ γ -NiOOH characteristically intercalates metal cations between its layers thus increasing its mass.⁸⁰ Transformations from the β/β couple to the α/γ couple lead to a significant increase in interlayer distance due to water intercalation.⁷⁸ These transformations are represented in the following Bode diagram^{76, 80}:

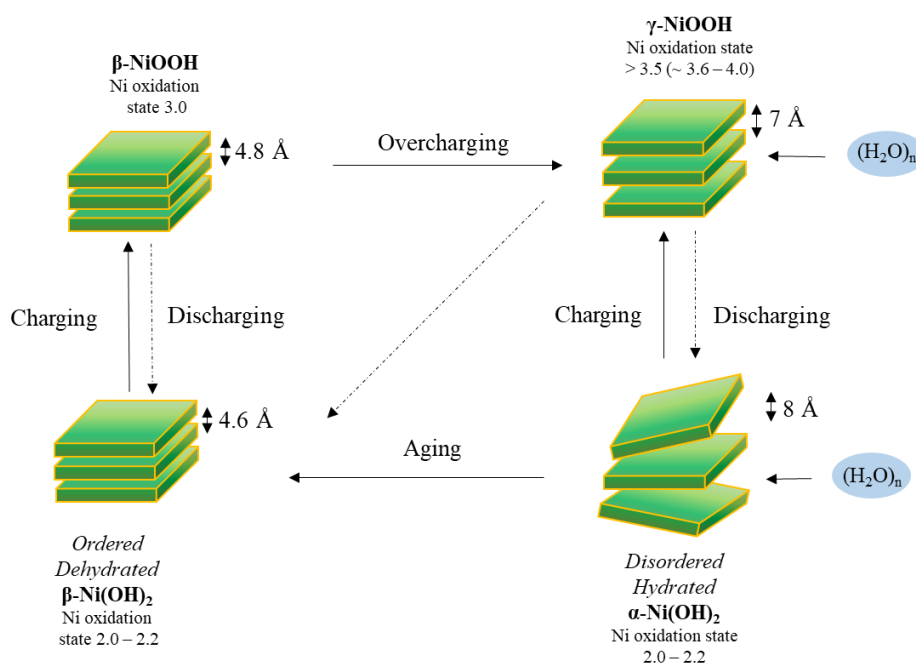


Figure 1.3: Bode diagram showing the transformations of Ni(OH)₂/NiOOH.⁷⁹⁻⁸⁰ Figure used with permission from ACS; *ACS Catalysis* **2020** 10 (1), 20-35, <https://pubs.acs.org/doi/10.1021/acscatal.9b02580>.⁸² Further permissions related to the material excerpted should be directed to ACS.

b. Preparation and Synthesis

A main factor affecting the performance of a catalyst is its synthesis method whereby some compounds might have different activities and electrochemical behaviors in the same electrolyte depending on its preparation.^{22, 83} This mainly has to do with the morphology of the produced material affecting its crystallinity, roughness and porosity which in turn lead to varying conductivity as well as active site distribution and electronic properties.²³ Nickel hydroxide can be prepared using several techniques depending on the desired phase, crystallinity, morphology and form, such as chemical precipitation, electrochemical precipitation, sol-gel synthesis, chemical and electrochemical aging and hydrothermal and solvothermal synthesis.⁷⁶ The following three methods were chosen based on their popularity and ease of use.⁷⁶

- 1) **Chemical precipitation** is used to prepare Ni(OH)₂ by adding a basic solution to a nickel(II) salt solution.⁷⁶ The phase is determined based on the solution concentrations, pH, type of base and salt used and temperature. For example, α -Ni(OH)₂ precipitates at room temperature while mixed α/β - phase or β -Ni(OH)₂ forms at higher temperature via ripening (rapid chemical aging of α to β).⁷⁶ Morphology of Ni(OH)₂ can be controlled by using the impregnation-precipitation method when a porous conductive substrate is dipped in nickel(II) salt solution and then treated with a basic solution.⁷⁶ This method is commonly used for battery anodes.⁷⁶
- 2) **Electrochemical precipitation** is used to form a layer of α -, α/β - or β -Ni(OH)₂ on a conductive substrate via anodic or cathodic electrodeposition, electro-precipitation and other methods.⁷⁶ For electrodeposition, the substrate is added to nickel(II) salt

solution and a negative or positive potential is held to produce a cathodic current (via water reduction) or an anodic current (via water oxidation).⁷⁶ The phase and crystallinity of the obtained Ni(OH)₂ depends on the counterion and concentration of the nickel(II) salt solution, temperature, substrate and deposition current density used.⁷⁶ For example, low deposition current densities (low mA/cm² range) generally result in α -Ni(OH)₂ while larger current densities result in mixed phase α/β -Ni(OH)₂.^{76, 84}

- 3) **Aging** is used to transform α -Ni(OH)₂ to β -Ni(OH)₂ in alkaline media and thus increasing the crystallinity of the material.⁷⁶ It can be categorized into chemical and electrochemical aging. Chemical aging mainly occurs at high temperature, such as 70 °C, and in concentrated alkaline media; however, it can also occur at room temperature and in water but at a slower rate.⁷⁶ Thermodynamically favored β -Ni(OH)₂ grows for instance as unstable α -Ni(OH)₂ dissolves based on a dissolution-precipitation mechanism in alkaline media.^{75, 85} Other mechanisms are also proposed such as a zipping mechanism.⁷⁶ Electrochemical aging occurs due to continued electrochemical cycling between Ni(OH)₂ and NiOOH of an α -Ni(OH)₂ electrode in alkaline media which leads to a decrease in conductivity and charge capacity.^{76, 85}

c. Ion Inclusion in Solution

Early studies on the effect of Fe impurities on Ni(OH)₂ electrodes showed a poisoning effect in Ni-based alkaline batteries due to a decrease in capacity, cycle life and OER overpotential.⁸⁶⁻⁹⁰ This effect was even seen at concentrations of under 1% Fe and initially thought to be due to the formation of ferric oxide.⁹¹ Corrigan was first to show that Fe impurities in solution, whether unintentional or intentional and at very low

concentrations of ~ 0.01%, co-precipitate and show a significant enhancement effect on the OER activity of NiO_xH_y.⁹²

Nocera et al. reported that electrodeposited amorphous Ni-(oxo)/hydroxo films in borate buffers (termed Ni-Bi) showed significant OER activity.^{7,93} However, these films reached maximum catalysis after conditioning at an anodic bias.⁹³ Generally, NiOOH forms the OER active phase of the catalyst as Ni³⁺ or a mixture of Ni³⁺ and Ni⁴⁺.^{77,93} As-deposited Ni-Bi resembled β-NiOOH and had an oxidation state of +3.1 which increased to +3.6 after anodization with the catalyst resembling γ-NiOOH.⁹³ Thus, due to the increase in activity seen with conditioning, γ-NiOOH was concluded to be more OER active than β-NiOOH⁹³ contradicting previous studies.²² Nonetheless, the reason behind the increase in activity during anodic conditioning turned out to be the inclusion of Fe.

Following the interest in Ni oxo/hydroxides and the work by Nocera and further studies by Boettcher et al. and Klaus et al. who reported that the increase in OER activity in the Ni(OH)₂/NiOOH system is due to the incidental incorporation of Fe traces from the unpurified electrolytes whether borate or KOH.^{77,92,94-95} In addition, aging α-Ni(OH)₂ in Fe-free KOH to form β-Ni(OH)₂ lowers its activity while aging in unpurified KOH incorporates Fe traces into the lattice and forms Ni-Fe LDH which as reported blocks the phase transformation of Ni(OH)₂.⁷⁷ Both research groups reported an increase in activity in unpurified KOH and a decrease in Fe-free purified KOH.^{77,94} This in turn clarified that the increase in activity of Ni-Bi with anodization is not due a consequent transformation of β-NiOOH to γ-NiOOH but Fe incorporation into the film,⁹⁴ as initially thought by Bediako et al.⁹⁶ Nocera et al. showed that Fe inclusion into Ni-Bi from Fe in solution followed by anodization in purified solution led to an increase

in Ni charge to IV. This was proposed to be due to Fe aiding in the overcharging from β to γ ⁹³ and thus increasing Ni-O covalency and oxyl character which in turn increases OER activity.⁹⁶

Corrigan also compared the effect of Fe in solution to 12 other d and f block transition metals and concluded that co-deposited Fe/Ni(OH)₂ results in the highest activity, except for Ce/Ni(OH)₂: $\eta = 287$ mV at $J = 16$ mA/cm².⁹⁷ The general trend of OER overpotential with coprecipitated metals, from largest to lowest, was determined as follows: Pb > Cd > Zn > Cr > Ni (reference) > Mn, Mg > Ag, Y > Co, Cu > La > Fe > Ce showing the significant enhancement effect of Ce, Fe and La, lowering overpotential by ~ 140 mV, and the poisoning effect of Pb, Cd and Zn, increasing overpotential by ~ 20 mV.⁹⁸ Thus, trivalent metal ions resulted in an enhancement in OER activity (Ce, Fe, La, Co, Y) while divalent ions lead to slight enhancement (Cu, Ag, Mg) or a poisoning effect (Cd, Zn).⁹⁸ Tetravalent ions also had little effect (Mn) or a poisoning effect (Pb) while hexavalent ions had little effect (Cr).⁹⁸ A cathodic shift by 20-25 mV in redox peaks with respect to those of Ni(OH)₂ was observed with Co and Mn. An anodic shift was observed with the other coprecipitated metals, namely with Ce, Cr, La and Zn reaching up to ~ 45 mV.⁹⁸ Fayad et al. reported that the addition of Fe³⁺ to 1 M KBi followed by potential cycling led to an increase in OER activity of Ni-Bi while the addition of Al³⁺ resulted in a decrease in OER activity.¹ Nonetheless, both showed similar electrochemical characteristics with an overall anodic shift in redox peaks after potential cycling and metal inclusion.¹ Studies using Mossbauer spectroscopy and extended X-ray absorption fine structure have shown that Fe substitutes Ni sites in the lattice as seen by the strong correlations between Ni and Fe.⁹⁹⁻

d. Codeposition of Fe

Ni-based bimetallic and trimetallic oxides have been of great interest as potential OER electrocatalysts due to their synergistic promoting effect with NiFe hydroxides and oxyhydroxides, namely $\text{Ni}_{0.9}\text{Fe}_{0.1}\text{O}_x$, surpassing the activity of NiO_xH_y and even IrO_x , thus competing with the most active catalysts in alkaline.^{24, 77, 92, 101-105} The role of doping Ni-based electrodes with guest metals and its effect on morphology, electronic properties and activity of the catalyst is needed to design efficient OER electrocatalysts. The inclusion of guest metals has varied effects on the transformations and stability of the redox couples depending on the nature of the introduced metal.^{99, 106} Namely, the substitution of Ni by Fe in α - $\text{Ni}(\text{OH})_2$ and γ - NiOOH within the hexagonal $[\text{NiO}_2]$ sheets has been reported to increase OER activity of the α/γ couple.^{80, 100} The α - $\text{Ni}(\text{OH})_2/\gamma$ - NiOOH redox couple was also reported to be stabilized by Fe^{3+} inclusion.^{76, 80} This was hypothesized to be due to the greater charge of Fe leading to an increase in anion intersheet bonding and an obstruction of transformation to β - $\text{Ni}(\text{OH})_2$.¹ Fe codeposition was also reported to stabilize the Ni-based catalyst as Mössbauer spectroscopic studies performed on NiFe LDH catalysts have shown that the NiOOH lattice was stabilized due to the formation of Fe(IV) neighboring Ni atoms in the bulk.¹⁰⁷

Boettcher et al. reported that Fe co-deposition at 25% leads to the formation of Ni-Fe LDH consequently blocking the aging of α - $\text{Ni}(\text{OH})_2$ to β - $\text{Ni}(\text{OH})_2$ and decreasing OER overpotential by 200 mV.⁹⁴ Nocera et al. showed that the co-deposition of $\text{Ni}_{0.9}\text{Fe}_{0.1}$ -Bi followed by anodization in Fe-containing electrolyte (KOH and KBi) led to similar results as Ni-Bi under the influence of Fe inclusion from solution, namely an

increase in OER activity and Ni charge to increase to IV.^{93, 96} Fayad et al. similarly reported that anodic conditioning was needed for NiFe-Bi films in Fe-containing borate to reach maximum catalysis, similar to the increase in OER with potential cycling after the addition of Fe³⁺ to KBi.¹

Several hypotheses have been proposed concerning the active site in these catalysts, whether Ni is the active site and neighboring Fe promote its activity or Fe is the active site itself.^{77, 94, 99, 107-110} SI-SECM (Surface Interrogation Scanning Electrochemical Microscopy) studies have shown the presence of two active sites in Ni_{1-x}Fe_xOOH films with Fe as the fast active site and Ni and the slow active site.¹¹⁰ Since Fe was hypothesized to be an active site, γ -FeOOH as an OER electrocatalyst was examined and found to be unstable in alkaline due to the formation of soluble FeO₄²⁻, and less OER active than Ni(Fe)O_xH_y with a high dissolution rate at overpotentials of 450 mV (96% decrease in current density after 4 h polarization), and ¹¹¹⁻¹¹² γ -FeOOH has shown high adsorption to OER intermediates while pure γ -NiOOH has shown weak adsorption.⁷⁸ Moreover, DFT calculations showed higher OER activity (lower overpotential) at Fe sites neighbored by Ni in both γ -FeOOH and γ -NiOOH, and near-optimal binding energies to OER intermediates at these sites.^{78, 100} Thus, the substitution and combination between Ni and Fe as a bimetallic catalyst, which ensures certain electronic interactions between the metals, was needed to sustain activity and form the needed catalytic active sites.

DFT studies by Li et. al showed that the lowest OER overpotentials by Fe in β -NiOOH.¹⁰⁹ Goldsmith et al. showed that the formation of Fe⁴⁺ occurs at the onset of catalysis in NiFeO_xH_y films and proposed the facilitation of oxidation of Fe³⁺ to Fe⁴⁺ by NiOOH and the location of active sites to be at defect sites, corners and edges.¹¹³

Martirez et al. reported a decrease in overpotential by 0.34 V when comparing Fe and Ni pathways and noted that the stability of an Fe(IV)-oxo species mediated pathway under low coordination of Fe in β -NiOOH.¹¹⁴ Moreover, the four-coordinated Fe on the surface of β -NiOOH was shown to be able to form two additional bonds.¹¹⁴ It was also reported to be catalytically active and did not form high-energy intermediates.¹¹⁴

e. Codeposition of Other Metals

Stahl et al. studied around 3500 trimetallic mixed metal oxide compositions in comparison to their pure metal oxide counterparts and reported that the most active OER catalysts are composed of Ni, Fe and a third metal such as Al, Ga and Cr.¹⁰³ Corrigan et al. studied the effect of co-precipitated guest metals on electrodeposited Ni(OH)₂ films at a metal:Ni ratio of 1:9 and showed that Ce, Fe and La were the most efficient with OER overpotentials of 277 mV, 287 mV and 358 mV, respectively, at 16 mA/cm².⁹⁷ Generally, mid-to-late first row transition metals have multiple oxidation states at OER potentials and thus tend to bind to each other and the electrode via oxo or hydroxo bonds.¹⁰³ However, similarly sized and charged metal ions did not have similar OER activity when co-deposited in Ni oxide films.¹⁰³ Ga can maintain almost the same activity as Al but was less active than Fe.⁹⁶ Mn resulted in low activity in some studies even though it is one of the main elements forming the OEC in Photosystem II.¹⁰³ The co-deposition of Cr as NiCr double hydroxide was reported to decrease OER potential by 190 mV at 0.5 mA/cm² with respect to IrO₂ but did not surpass NiFe double hydroxide, which lowered the potential by 230 mV.¹⁰⁶ Xu et al. recently reported that

$\text{Ni}_{0.6}\text{Fe}_{0.3}\text{Cr}_{0.1}\text{O}_x$ is ~ 31% more active than $\text{Ni}_{0.6}\text{Fe}_{0.4}\text{O}_x$ with Cr leaching out of the film and creating pores in the lattice which in turn increased the number of active sites.¹¹⁵

Carter et al. investigated the effect of 3d (V, Cr, Mn, Fe, Co) and 4d (Mo, Ru, Rh) transition metal dopants on OER catalysis of $\beta\text{-NiOOH}$ using DFT calculations.¹¹⁶ They examined the dopants' ability to form and stabilize terminal oxo species and the charge transfer between Ni(III) sites and dopants.¹¹⁶ They reported that Fe is the most effective dopant for OER on NiOOH followed closely by Co.¹¹⁶ Co(III) is less soluble in alkaline media leading to lower desorption off the Ni-catalyst surface, and in turn a possible decrease in OER activity.¹¹⁶ V(V), Mo(VI) and Ru(VII) were also predicted to lower OER overpotential in comparison to pure NiOOH possibly in a similar mechanism as Cr(VI)¹¹⁵ by etching into the solution and creating low coordination defect sites in the lattice.¹¹⁶ This was hypothesized since these dopants take on a 4-fold tetrahedral coordination and thus are not likely to stay on the surface.¹¹⁶

In earlier studies in this laboratory, Fayad et al. investigated the effects of Fe and Al on the redox behavior and OER catalysis of ultrathin Ni-Bi films in KBi.¹ They found that both Ni-Bi and co-deposited NiFe-Bi films required activation via anodization in KBi to reach maximum OER catalysis.¹ Thus, they hypothesized that the increase in OER activity with anodization is due to Fe modifying surface sites, surface-Fe, and not bulk-Fe.¹ They also reported that the addition of Al to KBi results in a decrease in OER activity of Ni-Bi and NiFe-Bi and an anodic shift in redox peaks.¹

In this work, we examined in electrochemical measurements the hypothesis that high OER activity is due to Fe-activated surface sites and not bulk-Fe inclusion. We also examined the sustainability of active sites and found that OER activity decreases at Fe-activated NiO_xH_y films in the absence of Fe in solution. The deactivation method is

proposed to be due to low-coordination surface-Fe moving to high-coordination bulk-Fe sites. This study is presented in Chapter 3.

We also examined further the role of Al, an ion that has been reported to increase OER activity when deposited in Ni-oxides, on the redox behavior and OER catalysis of Ni-oxo/hydroxide. Earlier work in this group showed that Al lowers OER currents in KBi electrolyte. We therefore began investigating the effect of Al in solution, in the absence and presence of Fe traces, and co-deposited in NiO_xH_y and Ni-Bi. This was presented in Chapter 4.

CHAPTER II

EXPERIMENTAL SECTION

A. Materials

Nickel (III) nitrate hexahydrate ($\text{Ni}(\text{NO}_3)_2 \cdot 6\text{H}_2\text{O}$, 99.999%, Aldrich), iron(III) nitrate nonahydrate ($\text{Fe}(\text{NO}_3)_3 \cdot 9\text{H}_2\text{O}$, 99.95%, Aldrich) and aluminum nitrate nonahydrate ($\text{Al}(\text{NO}_3)_3 \cdot 9\text{H}_2\text{O}$, 99.999%, Aldrich) were used in this work to deposited catalysts on fluorine-doped tin oxide coated glass (FTO, $R = 7 \Omega \cdot \text{sq}^{-1}$, low iron content, Solaronix). Boric acid (H_3BO_3 , 99.5%, Aldrich, specified by manufacturer to contain: $\text{Ca} \leq 0.005\%$, $\text{Fe} \leq 0.001\%$, heavy metals (such as Pb) $\leq 0.001\%$), potassium hydroxide (KOH, puriss, Aldrich, specified by the manufacturer to contain $\text{Fe} \leq 0.0005\%$, $\text{Al} \leq 0.001\%$, $\text{Ni} \leq 0.0005\%$, and heavy metals $\leq 0.0005\%$, indicated as Ag/As/Bi/Cd/Cu/Hg/Pb/Sb/Sn/Mo at ≤ 5 ppm total without exact determination of distribution) and deionized water (resistivity $18 \mu\Omega \cdot \text{cm}$, Nanopure Diamond, CRSL) were used for electrolyte preparation.

B. Preparation of Solutions

1. Preparation of KOH and KBi electrolytes

0.1 M KBi was used for the electrodeposition of Ni-oxo/hydroxo, NiFe-oxo/hydroxo and NiAl-oxo hydroxo films while 1 M KBi and 1 M KOH were used as electrolytes for cyclic voltammetry and chronoamperometric measurements. 0.1 M KBi was prepared by dissolving 3.0915 g in 500 mL of deionized water; its pH was adjusted to ~ 9.2 by the gradual addition of KOH pellets while stirring. Similarly, 1 M KBi was

prepared using 30.915 g of boric acid in 500 mL of deionized water. 1 M KOH of pH ~ 13.6 was freshly prepared by dissolving 2.8053 g in 50 mL of deionized water before every measurement.

2. KOH Electrolyte Purification

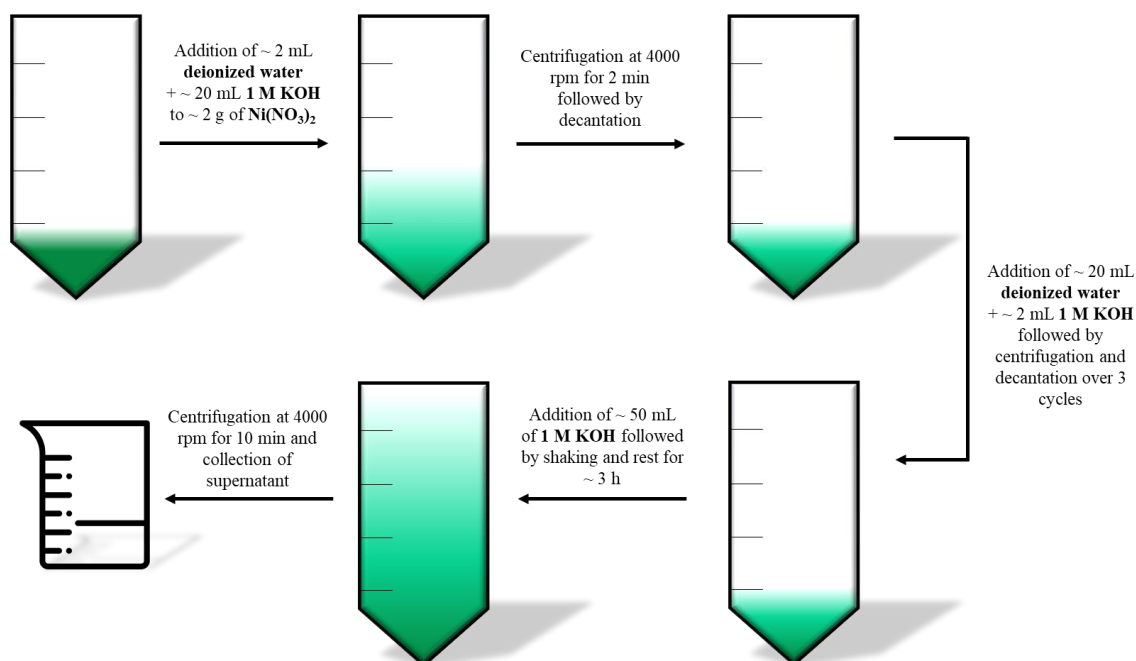


Figure 2.1: Scheme illustrating the purification of KOH from Fe traces.

KOH was purified from Fe impurities as previously reported by Boettcher et al.⁹⁴ ~ 2 g of nickel nitrate were added to polypropylene conical tubes and dissolved in ~ 2 mL of deionized water followed by the addition of ~ 20 mL of 1 M KOH. Pure nickel hydroxide is then precipitated. The solution was shaken briefly by hand to homogenize and centrifuged for 2 min at 4000 rpm followed by the decantation and disposal of the supernatant. ~ 20 mL of deionized water and ~ 2 mL of 1 M KOH were consecutively added to the precipitate followed by shaking, centrifugation and decantation. The latter

was repeated three times. ~ 50 mL of 1 M KOH was added to the solid Ni(OH)₂ in the tube. The solution was shaken by hand for 10 min, ensuring the resuspension of the solid in the solution, and then allowed to rest for ~ 3 h. This was followed by centrifugation at 4000 rpm for 10 min. The supernatant was collected in a polypropylene beaker and then filtered through a 0.45 μm pore size syringe filter using a 60 mL Luer-Lok syringe into a polypropylene conical tube. The final solution was briefly stored in the tube for a day or two as it was being used for the Fe-free experiments.⁹⁶ This solution is termed 1 M Fe-free KOH.

C. Electrodeposition of NiO_xH_y, NiFeO_xH_y and NiAlO_xH_y

1. Preparation of Substrates

Fluorine-doped tin oxide coated glass substrates (FTO, Solaronix, R = 7 Ω/sq, low iron content) were cut into ~ 1 × 4 cm² fragments. The electrodes were cleaned by ultrasonication for 15 min in a glass container filled with isopropanol. The solution was disposed and replaced by deionized water. It was then ultrasonicated for 15 min as well. The electrodes were then placed on a paper towel and air-dried. The electrode geometric area was defined using insulating epoxy resin at 1 cm² before electrodeposition. The width of the film is measured and the corresponding length to reach an area of 1 cm² is calculated. Using parafilm, the area is covered. A 2-part, resin and hardener, Alteco F-05 epoxy was used as follows: a small portion of the resin is added onto a watch glass and an equally sized portion of the hardener is added next to it. The two were then mixed thoroughly using a plastic spatula for ~ 1 min to activate the epoxy. The latter was then coated above the parafilm-covered area of the film. The upper portion of the film is left uncoated to allow its connection to the potentiostat during electrochemical

experiments. The film was then left to dry from an hour to a day. Before usage and after drying, the parafilm is removed and the now-defined area is thoroughly wiped, front and back, with acetone-soaked Kim wipes followed by ethanol-soaked-wiped to remove any impurities on the surface. The film is then rinsed off with deionized water and is ready for use.

2. Preparation of Ni-B_i, NiFe-B_i and NiAl-B_i solutions

0.4 M Ni(NO₃)₂ and Al(NO₃)₃, solutions were prepared by dissolving 0.1163 g of Ni(NO₃)₂·6H₂O and 0.1505 g of Al(NO₃)₃·9H₂O, respectively, in 1 mL of deionized water. 0.4 M Fe(NO₃)₃ solutions were freshly prepared by dissolving 0.0808 g of Fe(NO₃)₃·9H₂O in 0.5 mL of deionized water directly before electrodeposition. A mixed salt solutions of 1) 0.4 M Fe(NO₃)₃ and 0.4 M Ni(NO₃)₂ and 2) 0.4 M Al(NO₃)₃ and 0.4 M Ni(NO₃)₂ in a guest metal to Ni ratio of 4:6 were prepared by mixing 60 μL of 0.4 M Ni(NO₃)₂ and 40 μL of 0.4 M Fe(NO₃)₃ or 0.4 M Al(NO₃)₃ respectively. Ni(NO₃)₂ and mixed salt solutions were freshly diluted to a concentration of 0.4 mM via the addition of 20 μL of their respective 0.4 M solutions into 20 mL of 0.1 M KBi directly before electrodeposition.

3. Electrodeposition of NiO_xH_y, NiFeO_xH_y and NiAlO_xH_y on FTO

NiO_xH_y, NiFeO_xH_y and NiAlO_xH_y were electrodeposited on FTO substrates using a three-electrode electrochemical cell with FTO as the working electrode, Ag/AgCl (in 3 M NaCl, Bioanalytical Systems (BAS)) as the reference electrode and 1 mm diameter Pt wire as a counter electrode. An amperometric i-t measurement at anodic potential of 0.953 V vs. Ag/AgCl was performed in 0.4 mM of Ni(NO₃)₂ or

mixed salt solutions of 4:6 ratio of $\text{Fe}(\text{NO}_3)_3:\text{Ni}(\text{NO}_3)_2$ or $\text{Al}(\text{NO}_3)_3:\text{Ni}(\text{NO}_3)_2$, or 6:4 ratio of $\text{Al}(\text{NO}_3)_3:\text{Ni}(\text{NO}_3)_2$ in 0.1 M KBi, prepared as indicated in the previous section, until a set charge of 1, 10, 100 or 400 mC/cm^2 was reached.

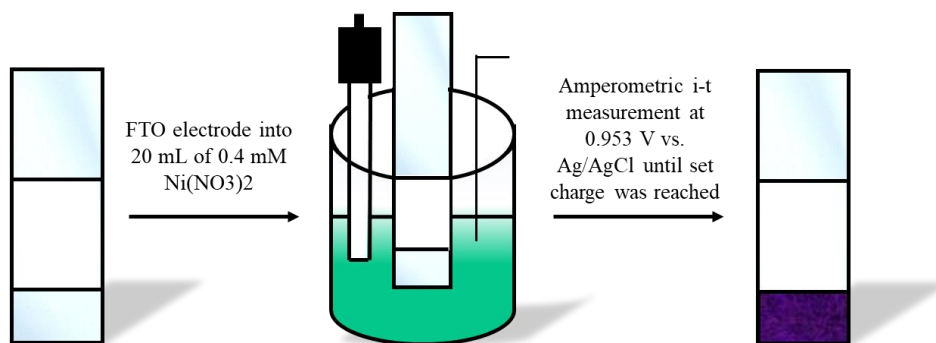


Figure 2.2: Scheme illustrating the electrodeposition of NiO_xH_y

D. Electrochemical Measurements:

I. Cyclic Voltammetry

Electrochemical measurements were conducted using CHI630A and CHI450C potentiostats in a three-electrode electrochemical cell made of glass for experiments in KBi and unpurified KOH and polypropylene plastic for experiments in Fe-free (purified from Fe impurities) KOH.

Cyclic voltammograms (CVs) were performed in 1 M KBi, 1 M unpurified KOH and 1 M Fe-free KOH. The potential was scanned in the positive direction between -0.6 V and 1.4 V vs. Ag/AgCl in KBi, 0 V and 1 V vs. Ag/AgCl in KOH, and 0 V and 1.1 V vs. Hg/HgO in KOH. CVs were acquired post-electrodeposition at 10, 20, 50 and 100 mV/s. This was followed by anodic conditioning (anodization), an amperometric I-t measurement, performed in the same electrolyte solution at 0.903 V vs. Ag/AgCl in 1 M KBi, 0.50 V or 0.51 V vs. Ag/AgCl or 0.58 V vs. Hg/HgO in 1 M

KOH with stirring at 600 rpm. CVs are acquired again at 10, 20, 50 and 100 mV/s post-anodization also in the same solution.

2. Tafel Plot Measurements

Steady-state currents using amperometric I-t curves, run for 600 s with stirring at 600 rpm to reach a steady-state, were acquired for Tafel plot measurements. Currents were measured at several potentials from ~ 0.46 V to 0.72 V vs. Ag/AgCl and ~ 0.58 V to 0.76 V vs. Hg/HgO in KOH, and ~ 0.86 V to 1.12 V vs. Ag/AgCl in KBi with an increment of 20 mV from high to low potential. A CV was acquired post-Tafel measurements at 10 mV/s. To calculate the overpotential for Tafel plots, open circuit potential was measured and the average of the last three reproducible values was used to determine the solution resistance to correct for ohmic potential losses using the iR compensation test in the instrument. Overpotential was calculated using the following equation:

$$\eta = E - E_{\text{eq}}(\text{O}_2/\text{H}_2\text{O}) - iR$$

where for Ag/AgCl, $E_{\text{eq}}(\text{V}) = 1.23 - (0.059 \times \text{pH}) + (0.059 \times \frac{\log(0.209)}{4}) - 0.197$

And for Hg/HgO, $E_{\text{eq}}(\text{V}) = 1.23 - (0.059 \times \text{pH}) + (0.059 \times \frac{\log(0.209)}{4}) - 0.117$

The amount of electrochemically active Ni was determined from the cathodic peak charges using the Gaussian peak shape mode of the CHI450C software.

3. Effect of Potential Cycling

NiO_xH_y , $\text{Ni}_{0.6}\text{Fe}_{0.4}\text{O}_x\text{H}_y$ and $\text{Ni}_{0.6}\text{Al}_{0.4}\text{O}_x\text{H}_y$ were electrodeposited as previously described by passing a charge of 1 or 100 mC/cm². The film was moved to a 1 M KBi, 1 M Fe-free KOH, 0.1 M KOH or 1 M unpurified KOH solution as indicated in different

experiments. A CV was initially acquired at 10 mV/s followed by 10 CVs at 100 mV/s then 1 CV at 10 mV/s was acquired. This process was repeated up to 7 times.

4. Sustainability of Active Sites

NiO_xH_y and $\text{Ni}_{0.6}\text{Fe}_{0.4}\text{O}_x\text{H}_y$ were electrodeposited as previously described by passing a charge of 1 or 10 mC/cm^2 and moved to 1 M Fe-free KOH where a CV is acquired at 10 mV/s. The films were rinsed with deionized water and taken to 1 M KOH where another CV is acquired at 10 mV/s. The film was anodized at 0.5 V vs. Ag/AgCl for ~ 3 h in 1 M KOH with stirring at 600 rpm and a CV at 10 mV/s was acquired post-anodization. The film was then rinsed and moved to 1 M Fe-free KOH where a CV at 10 mV/s was acquired followed by 10 CVs at 100 mV/s. This was repeated 6 times for the 1 mC/cm^2 film and 25 times for the 10 mC/cm^2 film.

5. Addition of Metal Impurities to the Electrolyte

NiO_xH_y was electrodeposited as previously described by passing a charge of 1 or 400 mC/cm^2 . A CV at 10 mV/s was acquired in 1 M KBi, 1 M Fe-free KOH, 0.1 M KOH or 1 M KOH. It was followed by the addition of 8 μL of the 0.4 M $\text{Fe}(\text{NO}_3)_3$ stock solution into 20 mL of the electrolyte to form 0.16 mM of Fe^{3+} and the addition of 0.5, 4, 8 and 16 μL of the 0.4 M $\text{Al}(\text{NO}_3)_3$ stock solution into 20 mL of the electrolyte to form 0.01, 0.08, 0.16 and 0.32 mM of Al^{3+} respectively. The solution was then manually stirred for a few seconds and followed by a CV at 10 mV/s. 10 CVs at 100 mV/s then a CV at 10 mV/s were acquired. This was repeated 6 times.

To test the effect of lower Fe amounts, NiO_xH_y was similarly electrodeposited by passing a charge of 1 mC/cm^2 and two CVs at 10 mV/s were acquired in 1 M Fe-free

KOH. 2 μL of 0.4 M $\text{Fe}(\text{NO})_3$ were taken and diluted to 1 mL using deionized water to form a solution of 0.8 mM $\text{Fe}(\text{NO})_3$. 3 μL of 0.8 mM $\text{Fe}(\text{NO})_3$ was added to 20 mL of 1 M Fe-free KOH, amounting to 2.4 nmol of Fe^{3+} in solution. This was followed by a CV at 10 mV/s, 10 CVs at 100 mV/s and a CV at 10 mV/s and repeated 6 times. 23.25 μL of 0.8 mM $\text{Fe}(\text{NO})_3$, or 18.6 nmol of Fe^{3+} , were added to the same solution (21 nmol of Fe^{3+} in total) and a CV at 10 mV/s was acquired again. This was followed by 10 CVs at 100 mV/s and a CV at 10 mV/s and repeated 6 times.

1.5 μL volume of 0.8 mM $\text{Fe}(\text{NO})_3$ was added to 20 mL of 1 M Fe-free KOH and amounting to 1.2 nmol of Fe^{3+} in solution. 3 CVs at 10 mV/s were acquired followed by anodic conditioning at 0.5 V for ~ 3 h with stirring at 600 rpm. 3 CVs at 10 mV/s were acquired post-anodization followed by 10 CVs at 100 mV/s and a CV at 10 mV/s and repeated 2 times.

Similarly, to test thicker films, NiO_xH_y was electrodeposited by passing a charge of 100 mC/cm² and two CVs at 10 mV/s were acquired in 1 M Fe-free KOH. 3 μL of 0.8 mM $\text{Fe}(\text{NO})_3$, amounting to 2.4 nmol of Fe^{3+} , were added to the electrolyte. This was followed by a CV at 10 mV/s, 10 CVs at 100 mV/s and a CV at 10 mV/s and repeated 6 times. 7 μL of 0.8 mM $\text{Fe}(\text{NO})_3$ were added to the same 20 mL of 1 M Fe-free KOH in-use and thus equating to an additional 5.6 nmol of Fe^{3+} in solution (8 nmol of Fe^{3+} in total). A CV at 10 mV/s was acquired again. This was followed by 10 CVs at 100 mV/s and a CV at 10 mV/s and repeated 6 times. The film was then anodized at 0.5 V for 1 h with stirring at 600 rpm. This was followed by a CV at 10 mV/s, 20 CVs at 100 mV/s and a CV at 10 mV/s and repeated 2 times.

To test the effect of the addition of Pt to solution, NiO_xH_y was electrodeposited at 1 mC/cm² and two CVs at 10 mV/s were acquired in 1 M unpurified KOH. This was

followed by 5 CVs at 100 mV/s and a CV at 10 mV/s; this was repeated twice. A CV at 10 mV/s was acquired from -1.5 to 1 V to test this range. A CV at 10 mV/s was then acquired. 10 CVs at 100 mV/s followed by a CV at 10 mV/s were acquired; this was repeated twice. 4 μ L of 50 mM K_2PtCl_4 (aqueous and aged for 1 day) were added to 25 mL of 1 M KOH. A CV at 10 mV/s was acquired. 10 CVs at 100 mV/s followed by a CV at 10 mV/s were then acquired; this was repeated twice. A CV at 10 mV/s was acquired from -1.5 to 1 V.

6. Electrode Aging in Fe-free KOH

NiO_xH_y was electrodeposited as previously stated by passing a charge of 100 mC/cm^2 . A CV at 10 mV/s was acquired in 1 M Fe-free KOH in the range of 0.18 V and 0.6 V, without overcharging, followed by aging in the same solution for 15 min. This was repeated 4 times until total time reached was 1 h.

E. SEM Imaging and EDX:

SEM images of NiO_xH_y , $NiFeO_xH_y$ and $NiAlO_xH_y$ electrodeposited at 100 mC/cm^2 and 400 mC/cm^2 were taken using a Tescan MIRA 3 LMU FEG SEM equipped with a SE beam detector and IN-Beam SE detector. EDX spectra of these films were acquired using an Oxford Instruments X-Max 20 EDX detector and Oxford INCA software.

CHAPTER III

INVESTIGATION OF THE EFFECTS OF IRON IN NICKEL HYDROXIDE FILMS ON OXYGEN EVOLUTION REACTION CATALYSIS

This work has been published in *ACS Catalysis*; *ACS Catalysis* **2020** *10* (1), 20-35, <https://pubs.acs.org/doi/10.1021/acscatal.9b02580>.⁸² Further permissions related to the material excerpted should be directed to ACS.

Catalysts are needed to fasten the slow kinetics of OER. Historically, rare-metal oxide OER electrocatalysts, such as iridium oxide and ruthenium oxide,^{29, 117} have been found to be the most efficient but recent studies have shifted their focus towards investigating and designing cheap non-noble metal catalysts.^{1, 29, 61, 77, 92, 101-105, 118-122} Ni and its bimetallic and trimetallic oxides, especially with Fe, have been shown in many studies as efficient non-noble metal OER electrocatalysts in alkaline media over the years.^{1, 29, 61, 77, 92, 101-105, 118-122}

Studies have shown an enhancement in OER activity by Ni-oxide films occurs due to the presence of Fe impurities in the electrolyte.^{92, 94-95} To better understand any catalyst, a correlation between its structure and activity is needed. Several hypotheses have been proposed towards understanding the effect of Fe and other guest metals on Ni-based oxide OER catalysts leading to a debate between whether Ni is the active site, with Fe promoting its activity, or Fe is the active site.^{77, 94, 99, 107-110}

Maximum catalysis was reached in thin Ni-(oxo)/hydroxide films deposited at low anodic bias after anodic conditioning in borate buffer.^{5, 7, 93} Boettcher et al. refuted the

initial claim that γ -NiOOH formation by overcharging and increase in Ni charge to IV were responsible for the enhancement in OER activity⁹³ but rather the inclusion of Fe into the catalyst films from traces of Fe in solution.^{92, 94-95} Nocera et al. further hypothesized that the inclusion of Fe increases the transformation to Ni(IV) and thus induces more Ni-O covalency enhancing the oxyl character and in turn increasing OER activity.⁹⁶

Electrochemical co-deposition of Fe in Ni-oxides, whether at anodic or cathodic bias, via annealing of mixed salt solutions or post-deposition by incubation or aging in Fe-containing solution leads to Fe inclusion in the catalyst film.^{1, 92, 94-95, 102} OER activity has been measured and studied in unpurified Fe-containing electrolytes^{7, 93} until recently.⁹⁴⁻⁹⁵ Fe³⁺ substitutes for Ni²⁺ during co-deposition of Fe in NiO_xH_y leading to the presence of Fe coordinated to six oxygen atoms in the Ni(OH)₂ lattice with the excess charge balanced out via intersheet bonding with the existing anions.^{76, 80, 123} We term this Fe as “bulk-Fe”. In contrast, Fe inclusion post-deposition via uptake from electrolyte with aging or under bias is proposed to occupy surface sites, such as edges and corners, and form low coordination with the lattice oxygens.¹¹⁴ We term this Fe as “surface-Fe”. Thus, the previously proposed hypothesis¹ that OER activity enhancement is due to Fe included post deposition rather than Fe included during anodic deposition of NiFe-oxo/hydroxide films is studied. It was followed by two main questions: 1) can bulk-Fe exchange to form surface-Fe in NiFe-oxo/hydroxide forming active sites and 2) are active sites in NiFe-oxo/hydroxide, and ultimately OER activity, sustained in the absence of Fe in solution.

The effect of mode of inclusion of Fe in Ni-oxo/hydroxide films on its electrochemical behavior and OER activity was examined in purified of Fe or Fe-

containing 1 M KOH. Fe was co-included in Ni-oxo/hydroxide films of different thicknesses at a Ni:Fe ratio of 6:4 which were scanned and anodized in Fe-free electrolyte. Moreover, Fe was included post-deposition from Fe-containing electrolyte for activation of catalyst then the catalyst was moved to Fe-free solution to examine the sustainability of OER active sites. Results show that post-deposition surface-Fe increases OER activity and not bulk-Fe, and that at both Fe-activated co-deposited and anodized NiFe-oxo/hydroxide, high OER catalysis cannot be maintained when Fe is removed from solution.

A. Dependence of OER Catalysis at NiO_xH_y on Surface-Fe vs. Bulk-Fe

1. Effect of Fe Co-deposition in Thin $\text{Ni}_{0.6}\text{Fe}_{0.4}\text{O}_x\text{H}_y$)_{1mC} on the Electrochemical Behavior and OER in 1 M Fe-free KOH and 1 M Unpurified KOH

a. Effect of Fe on OER Catalysis

Anodic electrodeposition of Ni- and NiFe-oxo/hydroxide films at varied loading of 1, 10 and 100 mC/cm² was performed on low Fe content FTO substrate using 0.4 mM $\text{Ni}(\text{NO}_3)_2$ or mixed $\text{Ni}(\text{NO}_3)_2$: $\text{Ni}(\text{NO}_3)_3$ at 6:4 ratio in 0.1 M KBi buffer of pH ~ 9.2.^{1, 93, 95-96} The films were rinsed and moved to a glass cell with 1 M unpurified KOH (containing Fe traces) or a non-glass cell with 1 M Fe-free KOH.⁹⁴ The films are referred to through the text according to their Ni:Fe ratio and charge during deposition such as $\text{Ni}_{0.6}\text{Fe}_{0.4}\text{O}_x\text{H}_y$)_{1mC}.

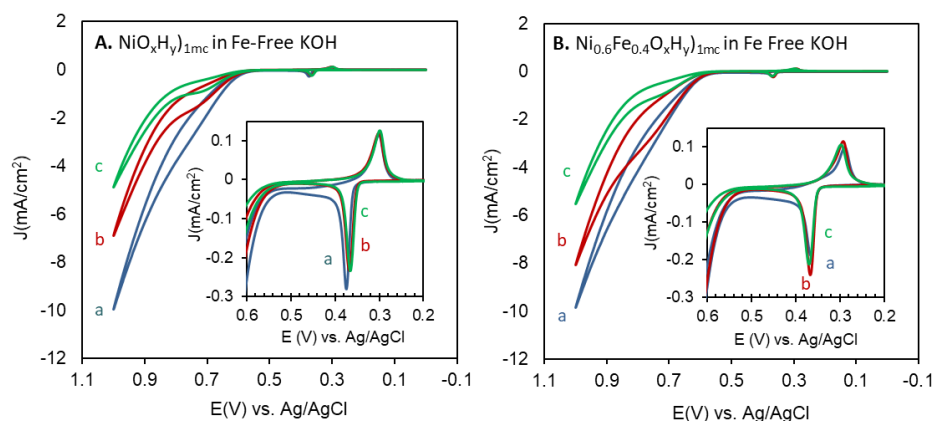


Figure 3.1: Cyclic voltammograms in 1 M Fe-free KOH at $\text{NiO}_x\text{H}_y)_{1\text{mC}}$ (A) and $\text{Ni}_{0.6}\text{Fe}_{0.4}\text{O}_x\text{H}_y)_{1\text{mC}}$ (B) as a first scan (a, blue), after anodic conditioning in the same solution (b, red) and after Tafel measurements (c, green). The insets show the corresponding redox peaks and onset of oxygen evolution for the three scans shown.

Scan rate is 10 mV/s. Figure used with permission from ACS; ACS

Catalysis **2020** *10* (1), 20-35, <https://pubs.acs.org/doi/10.1021/acscatal.9b02580>.⁸²

Further permissions related to the material excerpted should be directed to ACS.

Figure 3.1 shows CVs of $\text{NiO}_x\text{H}_y)_{1\text{mC}}$ (A) and $\text{Ni}_{0.6}\text{Fe}_{0.4}\text{O}_x\text{H}_y)_{1\text{mC}}$ (B) in 1 M Fe-free KOH at 10 mV/s: as-deposited (a), after anodic conditioning (b) and after Tafel measurements (c). Ultrathin films formed of a few monolayers of electrochemically active $\text{Ni}(\text{OH})_2$ (2-7 nm) were electrodeposited at $1 \text{ mC}/\text{cm}^2$. The number of moles of electrochemically active Ni was derived from CVs at 10 mV/s by integrating the charge of the $\text{NiOOH}/\text{Ni}(\text{OH})_2$ cathodic peak. It equaled $0.68 \pm 0.24 \text{ mC}/\text{cm}^2$ for $\text{NiO}_x\text{H}_y)_{1\text{mC}}$ and $0.50 \pm 0.10 \text{ mC}/\text{cm}^2$ for $\text{Ni}_{0.6}\text{Fe}_{0.4}\text{O}_x\text{H}_y)_{1\text{mC}}$. Assuming a film density of $1.25 \text{ g}/\text{cm}^3$, 8 \AA per monolayer and $1.2 \text{ e}/\text{Ni}$, the number of moles of active Ni (n_{Ni}) and $\text{Ni}(\text{OH})_2$ monolayers and thickness were calculated.⁸⁰ In Fe-free KOH, average n_{Ni} in as-deposited $\text{NiO}_x\text{H}_y)_{1\text{mC}}$ equaled to $5.85 \pm 2.04 \text{ nmol}/\text{cm}^2$ ($N = 5$), with a range of 3.4 –

8.1 nmol/cm², average thickness equaled to 4.34 ± 1.51 nm and average monolayers equaled to 5.42 ± 1.89 monolayers. While the average n_{Ni} in as-deposited $\text{Ni}_{0.6}\text{Fe}_{0.4}\text{O}_x\text{H}_y)_{1\text{mC}}$ equaled to 4.29 ± 0.86 nmol/cm² (N = 7), with a range of 2.8 – 5.3 nmol/cm², average $\text{Ni}(\text{OH})_2$ equivalent thickness equaled to 3.18 ± 0.64 nm and average monolayers equaled to 3.98 ± 0.80 monolayers. The average Ni content in as-deposited $\text{Ni}_{0.6}\text{Fe}_{0.4}\text{O}_x\text{H}_y)_{1\text{mC}}$ relative to $\text{NiO}_x\text{H}_y)_{1\text{mC}}$ was $73 \pm 29\%$.

CVs of as-deposited, anodically conditioned and after-Tafel $\text{NiO}_x\text{H}_y)_{1\text{mC}}$ and $\text{Ni}_{0.6}\text{Fe}_{0.4}\text{O}_x\text{H}_y)_{1\text{mC}}$ in 1 M Fe-free KOH are shown in Figure 3.1. As-deposited films showed the major redox $\text{Ni}(\text{OH})_2/\text{NiOOH}$ redox peaks, prior to which, small anodic and cathodic shoulders can be seen in addition to water oxidation current at higher potential and a positive to negative reverse scan not following the forward scan. Both films were then anodically conditioned in the same solution of 1 M Fe-free KOH which led to a decrease in OER currents but no change in OER onset, the appearance of an anodic wave at 0.7 – 0.8 V, hysteresis with a lower oxidation current on the reverse scan in comparison to the forward scan. The films underwent Tafel measurements, also in the same solution, which led to more decrease in OER activity with no change in OER onset and the same anodic wave at 0.7 – 0.8 V and hysteresis. The anodic peak potential $E_{\text{p,a}}$ of $\text{NiO}_x\text{H}_y)_{1\text{mC}}$ cathodically shifted by 6 mV after anodization and by 3 mV after Tafel while its cathodic peak potential $E_{\text{p,c}}$ remained almost unchanged after anodization and Tafel. The anodic peak potential $E_{\text{p,a}}$ of $\text{Ni}_{0.6}\text{Fe}_{0.4}\text{O}_x\text{H}_y)_{1\text{mC}}$ remained the same after anodization and anodically shifted by 3 mV after Tafel while its cathodic peak potential $E_{\text{p,c}}$ anodically shifted by 3 mV after anodization and by 5 mV after Tafel.

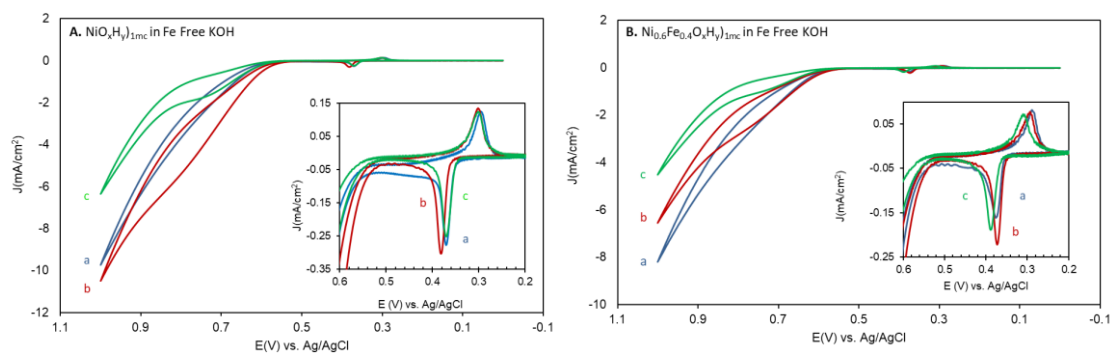


Figure 3.2: Cyclic voltammograms of the second set of films in 1 M Fe-free KOH at $\text{NiO}_x\text{H}_y)_{1\text{mC}}$ (A) and $\text{Ni}_{0.6}\text{Fe}_{0.4}\text{O}_x\text{H}_y)_{1\text{mC}}$ (B) as a first scan (a, blue), after anodic conditioning in the same solution (b, red) and after Tafel measurements (c, green). The insets show the corresponding redox peaks and onset of oxygen evolution for the three scans shown. Scan rate is 10 mV/s. Figure used with permission from ACS; ACS *Catalysis* **2020** *10* (1), 20-35, <https://pubs.acs.org/doi/10.1021/acscatal.9b02580>.⁸² Further permissions related to the material excerpted should be directed to ACS.

A similar trend was seen in all films with variation as seen in Figure 3.2 which shows CVs of other films of $\text{NiO}_x\text{H}_y)_{1\text{mC}}$ and $\text{Ni}_{0.6}\text{Fe}_{0.4}\text{O}_x\text{H}_y)_{1\text{mC}}$ in 1 M Fe-free KOH. A slight increase in OER currents after anodization followed by a decrease after Tafel with no change in OER onset, and similar hysteresis and an anodic wave at 0.7 – 0.8 V in $\text{NiO}_x\text{H}_y)_{1\text{mC}}$. A slight anodic shift in $E_{\text{p,a}}$ of $\text{NiO}_x\text{H}_y)_{1\text{mC}}$ was seen after anodization followed by cathodic shift returning it to its place after Tafel. While a slight cathodic shift in $E_{\text{p,a}}$ and a slight anodic shift of 3 mV in $E_{\text{p,c}}$ of $\text{Ni}_{0.6}\text{Fe}_{0.4}\text{O}_x\text{H}_y)_{1\text{mC}}$ were observed after anodization followed by distinct anodic shift of 13 mV in $E_{\text{p,a}}$ and 22 mV in $E_{\text{p,c}}$ after Tafel.

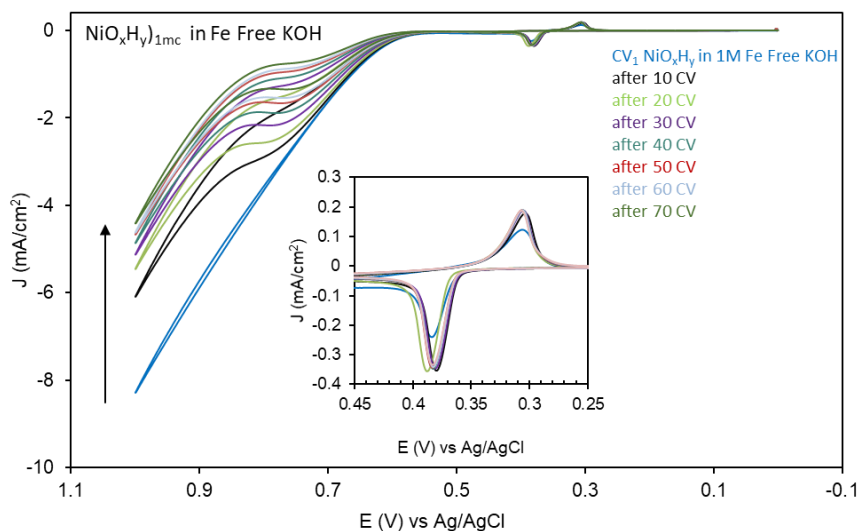


Figure 3.3: Cyclic voltammograms of NiO_xH_y film in 1 M Fe-free KOH as a first scan (CV_1 blue) and then CVs acquired after 10 CVs were taken at 100 mV/s, repeated 7 times in the same solution. The insets show the $\text{Ni}(\text{OH})_2/\text{NiOOH}$ redox peaks. The number of CVs (10-70) refers to the total number of scans acquired at 100 mV/s. Scan rate of all CVs in this figure is 10 mV/s. Figure used with permission from ACS; ACS *Catalysis* **2020** *10* (1), 20-35, <https://pubs.acs.org/doi/10.1021/acscatal.9b02580>.⁸² Further permissions related to the material excerpted should be directed to ACS.

The effect of potential cycling in Fe-free KOH was studied as seen in Figure 3.3 which shows the CVs of NiO_xH_y film at 10 mV/s performed initially and after each of the six cycles of 10 CVs at 100 mV/s in 1 M Fe-free KOH. The OER current of this film decreased with potential cycling with the appearance of an anodic wave at ~ 0.75 V and hysteresis. A slight cathodic shift in $E_{p,a}$ was seen only after the second scan with no additional shift seen with further cycling (except for the last cycle) while almost no change was seen in $E_{p,c}$. The variations in the electrochemistry of this system can be linked to presence of Fe traces in the purified electrolyte.

The amount of Ni in as-deposited $\text{NiO}_x\text{H}_y)_{1\text{mC}}$ ($N = 4$) was calculated to be $6.46 \pm 1.73 \text{ nmol/cm}^2$ and left almost unchanged at $6.34 \pm 1.85 \text{ nmol/cm}^2$ after anodization and $5.91 \pm 1.11 \text{ nmol/cm}^2$ after Tafel. Thus, an average decrease of $8.5 \pm 2.8\%$ was recorded. While the amount of Ni in as-deposited $\text{Ni}_{0.6}\text{Fe}_{0.4}\text{O}_x\text{H}_y)_{1\text{mC}}$ ($N = 4$) was calculated to be $4.46 \pm 1.11 \text{ nmol/cm}^2$ and left almost unchanged at $4.36 \pm 0.93 \text{ nmol/cm}^2$ after anodization and $4.13 \pm 1.04 \text{ nmol/cm}^2$ after Tafel. Thus, an average decrease of $7.4 \pm 2.6\%$ was recorded. This leads to the conclusion that film dissolution was not significant and thus was not the reason behind the decrease in OER currents with anodic conditioning and Tafel measurements.

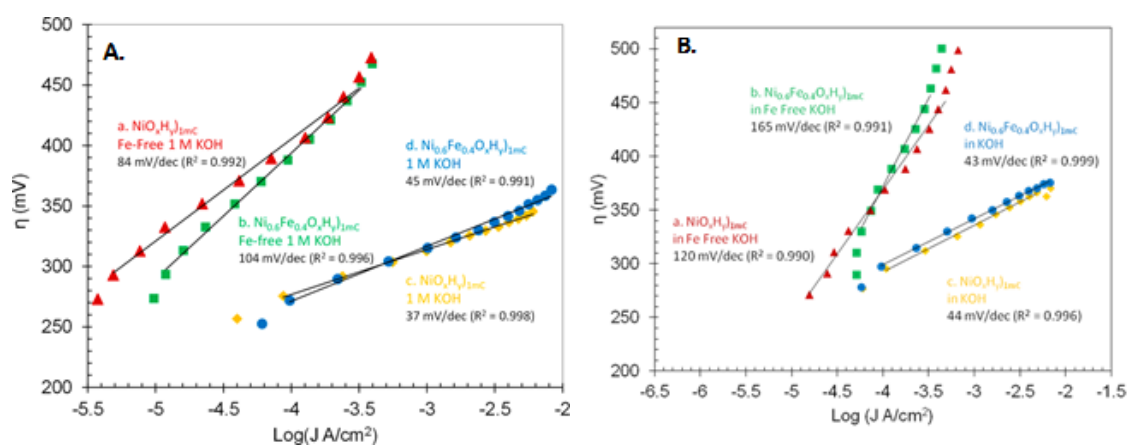


Figure 3.4: Tafel plots, overpotential η (mV) versus $\log(J \text{ A/cm}^2)$, for $\text{NiO}_x\text{H}_y)_{1\text{mC}}$ and $\text{Ni}_{0.6}\text{Fe}_{0.4}\text{O}_x\text{H}_y)_{1\text{mC}}$ films anodized in 1 M Fe-free KOH and measured in the same solutions (a-b) and $\text{NiO}_x\text{H}_y)_{1\text{mC}}$ and $\text{Ni}_{0.6}\text{Fe}_{0.4}\text{O}_x\text{H}_y)_{1\text{mC}}$ films anodized in 1 M unpurified KOH and measured in the same solution (c-d). These Tafel plots correspond to films whose CVs are presented in Figure 3.1-3.5 (A) and 3.2-3.6 (B). Figure used with permission from ACS; *ACS Catalysis* **2020** 10 (1), 20-35, <https://pubs.acs.org/doi/10.1021/acscatal.9b02580>.⁸² Further permissions related to the material excerpted should be directed to ACS.

Tafel plots of $\text{NiO}_x\text{H}_y)_{1\text{mC}}$ and $\text{Ni}_{0.6}\text{Fe}_{0.4}\text{O}_x\text{H}_y)_{1\text{mC}}$ films anodized in 1 M Fe-free KOH are presented in Figures 3.4. The Tafel slopes of $\text{NiO}_x\text{H}_y)_{1\text{mC}}$ equaled 84 and 120 mV/dec while those of $\text{Ni}_{0.6}\text{Fe}_{0.4}\text{O}_x\text{H}_y)_{1\text{mC}}$ equaled 104 and 165 mV/dec. Variations in Tafel slopes can be attributed to traces of Fe in the purified electrolyte and possible range of mixed α/β phases in the film. Nonetheless, the high Tafel slope values are an indication that in the absence of Fe in solution, the codeposition of Fe in $\text{Ni}_{0.6}\text{Fe}_{0.4}\text{O}_x\text{H}_y)_{1\text{mC}}$ did not lead to an increase in OER activity and thus a more active catalyst.

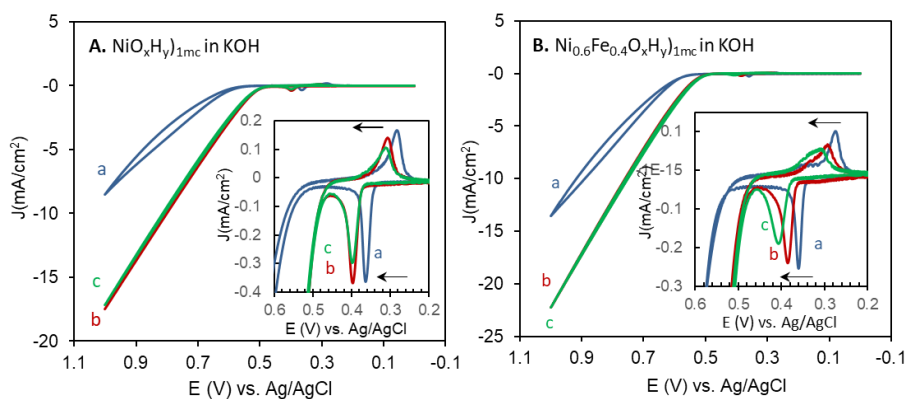


Figure 3.5: Cyclic voltammograms in 1 M KOH at $\text{NiO}_x\text{H}_y)_{1\text{mC}}$ (A) and $\text{Ni}_{0.6}\text{Fe}_{0.4}\text{O}_x\text{H}_y)_{1\text{mC}}$ (B) as a first scan (a, blue), after anodic conditioning in the same solution (b, red) and after Tafel measurements (c, green). The insets show the corresponding redox peaks and onset of oxygen evolution for the three scans shown. Scan rate is 10 mV/s. Figure used with permission from ACS; ACS Catalysis **2020** 10 (1), 20-35, <https://pubs.acs.org/doi/10.1021/acscatal.9b02580>.⁸² Further permissions related to the material excerpted should be directed to ACS.

Figure 3.5 shows CVs of $\text{NiO}_x\text{H}_y)_{1\text{mC}}$ and $\text{Ni}_{0.6}\text{Fe}_{0.4}\text{O}_x\text{H}_y)_{1\text{mC}}$ as-deposited (a), anodized (b) and after Tafel (c) in 1 M KOH, which contains traces of Fe impurities, done for comparison to the 1 M Fe-free KOH. OER activity of both films $\text{NiO}_x\text{H}_y)_{1\text{mC}}$ and $\text{Ni}_{0.6}\text{Fe}_{0.4}\text{O}_x\text{H}_y)_{1\text{mC}}$ increased with anodic conditioning in 1 M KOH with an anodic shift in both redox peaks and half wave potential, $E_{1/2}$, by 29 mV and 22 mV, respectively. This was similarly seen in the behavior of Ni-Bi in KBi.^{1, 7, 93} Similarly, an increase in OER currents was also seen in the anodization i-t traces performed in 1 M KOH in contrast to the decrease seen in 1 M Fe-free KOH (Figure 3.14).

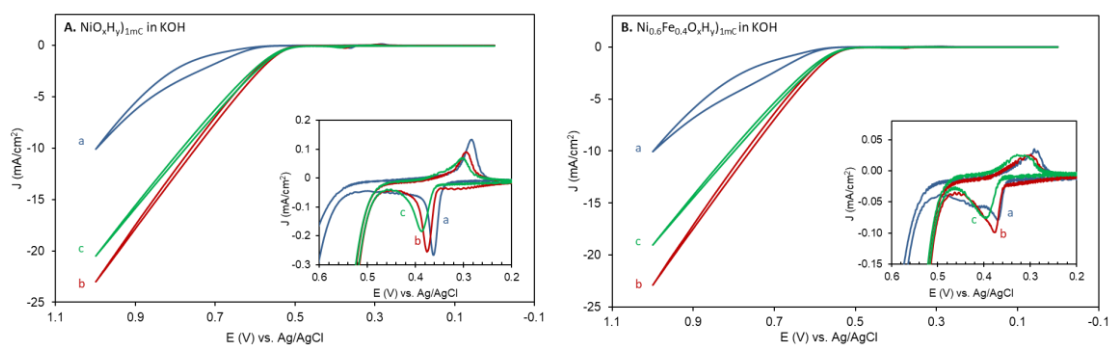


Figure 3.6: Cyclic voltammograms of the second set of films in 1 M KOH at $\text{NiO}_x\text{H}_y)_{1\text{mC}}$ (A) and $\text{Ni}_{0.6}\text{Fe}_{0.4}\text{O}_x\text{H}_y)_{1\text{mC}}$ (B) as a first scan (a, blue), after anodic conditioning in the same solution (b, red) and after Tafel measurements (c, green). The insets show the corresponding redox peaks and onset of oxygen evolution for the three scans shown. Scan rate is 10 mV/s. Figure used with permission from ACS; ACS *Catalysis* **2020** 10 (1), 20-35, <https://pubs.acs.org/doi/10.1021/acscatal.9b02580>.⁸² Further permissions related to the material excerpted should be directed to ACS.

OER currents remained high after Tafel or slightly decreased at high potentials, as seen in the other films examined in Figure 3.6, with a slight anodic shift in $E_{1/2}$ of 4

mV for $\text{NiO}_x\text{H}_y)_{1\text{mC}}$ and a greater anodic shift of 20 mV for $\text{Ni}_{0.6}\text{Fe}_{0.4}\text{O}_x\text{H}_y)_{1\text{mC}}$ (Figure 3.5). A similar trend with a slight anodic shift in anodized $\text{NiO}_x\text{H}_y)_{1\text{mC}}$ and $\text{Ni}_{0.6}\text{Fe}_{0.4}\text{O}_x\text{H}_y)_{1\text{mC}}$ and a further anodic shift after Tafel was seen in Figure 3.6. Films tested in 1 M KOH did not show any hysteresis or an anodic wave in addition to the reverse scan almost tracing the forward scan. Anodization in 1 M KOH also leads to the formation of a cathodic shoulder, denoted as A', positive to the main cathodic peak, denoted as A, which increases in size after Tafel and is more prominent in $\text{Ni}_{0.6}\text{Fe}_{0.4}\text{O}_x\text{H}_y)_{1\text{mC}}$.

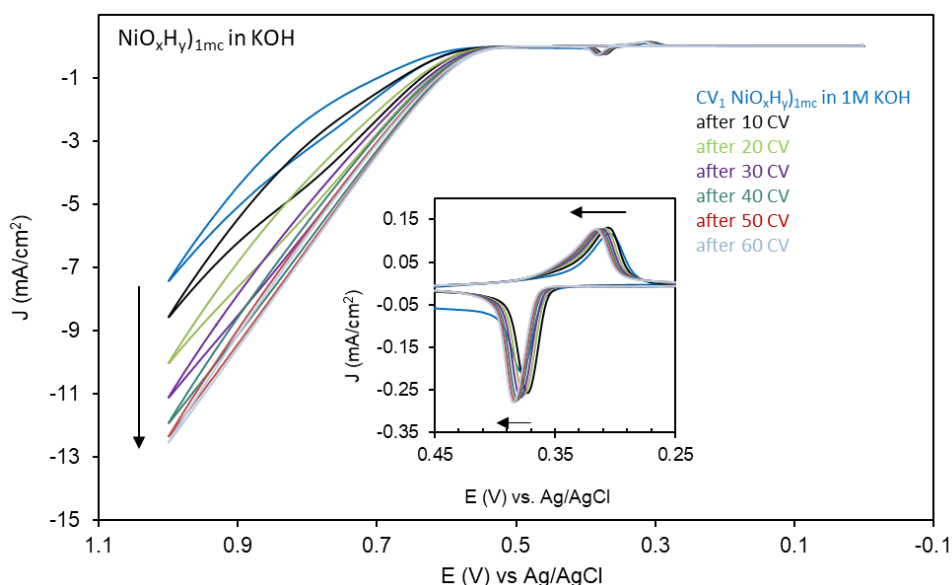


Figure 3.7: Cyclic voltammograms of $\text{NiO}_x\text{H}_y)_{1\text{mC}}$ film in 1 M KOH as a first scan (CV₁ blue) and then CVs acquired after 10 CVs were taken at 100 mV/s, repeated 6 times in the same solution. The insets show the $\text{Ni(OH)}_2/\text{NiOOH}$ redox peaks. The number of CVs (10-60) refers to the total number of scans acquired at 100 mV/s. Scan rate of all CVs in this figure is 10 mV/s. Figure used with permission from ACS; ACS *Catalysis* **2020** 10 (1), 20-35, <https://pubs.acs.org/doi/10.1021/acscatal.9b02580>.⁸² Further permissions related to the material excerpted should be directed to ACS.

The effect of potential cycling was also studied in 1 M KOH at $\text{NiO}_x\text{H}_y)_{1\text{mC}}$ (Figure 3.7) and resulted in a similar trend to anodized films in this electrolyte: a decrease in OER overpotential, increase in OER currents, anodic shifts in both redox peaks and loss of hysteresis.

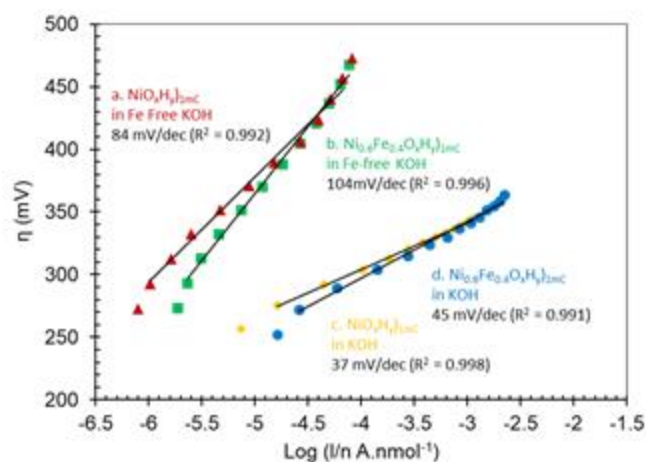


Figure 3.8: Normalized Tafel plots, overpotential η (mV) versus $\log(I/n \text{ A.nmol}^{-1})$, where nmol is for the electrochemically active Ni centers, for $\text{NiO}_x\text{H}_y)_{1\text{mC}}$, and $\text{Ni}_{0.6}\text{Fe}_{0.4}\text{O}_x\text{H}_y)_{1\text{mC}}$ films anodized in 1 M Fe-free KOH (a-b) and unpurified 1 M KOH (c-d), and measured in the same solution: for the Tafel plots in Figure 3.1 and 3.5 using $1.2e/\text{Ni}$ for determining nmol of Ni for all films in both solutions. Figure used with permission from ACS; *ACS Catalysis* **2020** 10 (1), 20-35, <https://pubs.acs.org/doi/10.1021/acscatal.9b02580>.⁸² Further permissions related to the material excerpted should be directed to ACS.

Tafel plots of $\text{NiO}_x\text{H}_y)_{1\text{mC}}$ and $\text{Ni}_{0.6}\text{Fe}_{0.4}\text{O}_x\text{H}_y)_{1\text{mC}}$ films anodized in 1 M KOH are presented in Figure 3.4. The Tafel slopes of $\text{NiO}_x\text{H}_y)_{1\text{mC}}$ equaled 37 and 44 mV/dec

while those of $(\text{Ni}_{0.6}\text{Fe}_{0.4}\text{O}_x\text{H}_y)_{1\text{mC}}$ equaled 45 and 43 mV/dec and fall in the literature range of ~ 40 mV/dec for thin Ni-Bi films in KBi and $\text{Ni}(\text{OH})_2$ films in unpurified KOH (with Fe traces).^{1, 7, 92-93, 95} Normalized Tafel plots in 1 M KOH and 1 M Fe-free KOH, using $1.2e/\text{Ni}$, are shown in Figure 3.8 where the currents are divided by the number of active Ni as calculated from the CVs acquired after Tafel. The plots show that OER activity is proportional over some overpotentials to active Ni centers.

b. Effect of Fe on Redox Peak Behavior

The presence of Fe during deposition did not lead to a shift in $E_{1/2}$ or a decrease in peak separation, ΔE_p . As-deposited $(\text{NiO}_x\text{H}_y)_{1\text{mC}}$ recorded an ΔE_p of 76 ± 3 mV ($N = 5$) and 79 ± 3 mV ($N = 10$) in 1 M Fe-free KOH and 1 M KOH, respectively, while $(\text{Ni}_{0.6}\text{Fe}_{0.4}\text{O}_x\text{H}_y)_{1\text{mC}}$ recorded an ΔE_p of 78 ± 6 mV ($N = 7$) and 76 ± 5 mV ($N = 9$) in 1 M Fe-free KOH and 1 M KOH, respectively. Codeposition of Fe in $\text{Ni}_x\text{Fe}_{1-x}$ -Bi films studied in KBi previously showed no shift in $E_{1/2}$ and a decrease in ΔE_p , which 112 ± 7 mV for $\text{Ni}_{0.6}\text{Fe}_{0.4}$ -Bi and 134 ± 8 mV for Ni-Bi.¹ An anodic shift in redox peaks was reported in certain previous studies where Fe was codeposited with Ni- or Co-oxides^{92, 94-95, 98-99, 107, 124}, however, this was not the trend in all cases and depended on the deposition and incorporation methods used in catalyst preparation.^{1, 124-126} Swierk et al. reported a decrease in ΔE_p with no anodic shift of redox peaks with Fe inclusion.¹²⁵ Scherson et al. reported a slight cathodic shift in redox peaks.¹²⁶ Boettcher et al. also reported that no shift in redox peaks with the incorporation of Fe from solution into cathodically deposited CoO_xH_y while an anodic shift was seen in cathodically codeposited $\text{Co}(\text{Fe})\text{O}_x\text{H}_y$.¹²⁴ An anodic shift was observed with anodization in Fe-containing electrolyte of anodically deposited films. Anodic codeposition of

$\text{Ni}(\text{Fe})\text{O}_x\text{H}_y$ might not have led to the inclusion of Fe into a $\text{Ni}(\text{OH})_2$ phase in which Fe either strongly interacts or is placed in sites which would have resulted in an anodic shift.

2. Effect of Fe Co-deposition in Thick $\text{Ni}_{0.6}\text{Fe}_{0.4}\text{O}_x\text{H}_y$ on the Electrochemical Behavior and OER in 1 M Fe-free KOH and 1 M Unpurified KOH

a. Effect of Fe on OER Catalysis

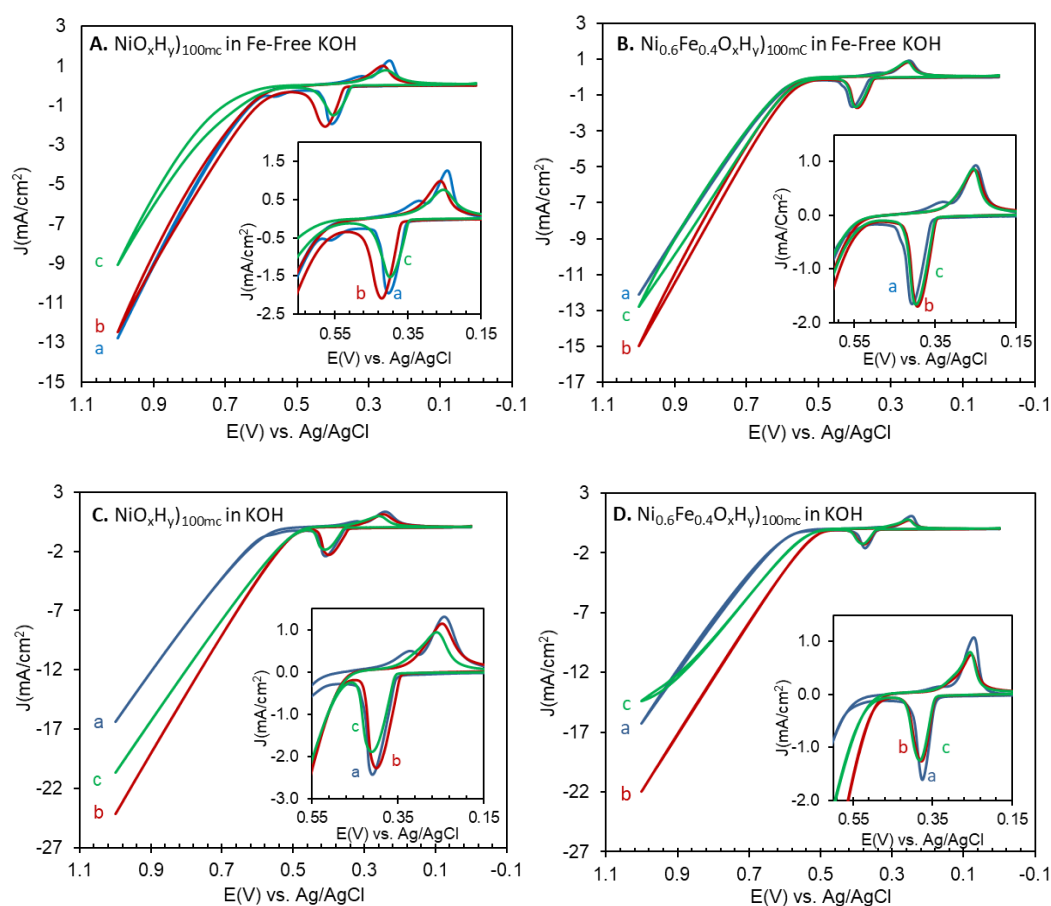


Figure 3.9: Cyclic voltammograms in 1 M Fe-free KOH (A, B) and in 1 M KOH (C, D) at NiO_xH_y)_{100mc} (A, C) and $\text{Ni}_{0.6}\text{Fe}_{0.4}\text{O}_x\text{H}_y$)_{100mc} (B, D) as a first scan (a, blue), after anodic conditioning in the same solution (b, red) and after Tafel measurements (c, green). The insets show the corresponding redox peaks and onset of oxygen evolution for the three scans shown. Scan rate is 10 mV/s. Figure used with permission from ACS; *ACS Catalysis* **2020** 10 (1), 20-35, <https://pubs.acs.org/doi/10.1021/acscatal.9b02580>.⁸² Further permissions related to the material excerpted should be directed to ACS.

The effect of film thickness was also examined at thicker $\text{NiO}_x\text{H}_y)_{100\text{mC}}$ and $\text{Ni}_{0.6}\text{Fe}_{0.4}\text{O}_x\text{H}_y)_{100\text{mC}}$ films electrodeposited at an anodic charge of 100 mC/cm^2 for ~ 30 min in 0.1 M KBi , unpurified from Fe traces. Figure 3.9 shows CVs of as-deposited, anodized and after Tafel $\text{NiO}_x\text{H}_y)_{100\text{mC}}$ and $\text{Ni}_{0.6}\text{Fe}_{0.4}\text{O}_x\text{H}_y)_{100\text{mC}}$ films in 1 M Fe-free KOH (A, B) and 1 M KOH (C, D). The Ni cathodic peak charges measured in 1 M Fe-free KOH for as-deposited $\text{NiO}_x\text{H}_y)_{100\text{mC}}$ ($N = 4$) and $\text{Ni}_{0.6}\text{Fe}_{0.4}\text{O}_x\text{H}_y)_{100\text{mC}}$ ($N = 7$) were $8.1 \pm 2.7 \text{ mC/cm}^2$ and $4.9 \pm 2.1 \text{ mC/cm}^2$, respectively, thus resulting in $60\% \pm 33\%$ Ni in $\text{Ni}_{0.6}\text{Fe}_{0.4}\text{O}_x\text{H}_y)_{100\text{mC}}$ to $\text{NiO}_x\text{H}_y)_{100\text{mC}}$. Similarly, the Ni cathodic peak charges measured in 1 M KOH for as-deposited $\text{NiO}_x\text{H}_y)_{100\text{mC}}$ ($N = 2$) and $\text{Ni}_{0.6}\text{Fe}_{0.4}\text{O}_x\text{H}_y)_{100\text{mC}}$ ($N = 4$) were $10 \pm 3.8 \text{ mC/cm}^2$ and $5.2 \pm 1.3 \text{ mC/cm}^2$, respectively, thus resulting in $52\% \pm 24\%$ Ni in $\text{Ni}_{0.6}\text{Fe}_{0.4}\text{O}_x\text{H}_y)_{100\text{mC}}$ to $\text{NiO}_x\text{H}_y)_{100\text{mC}}$. Though the films are deposited at a charge of 100 mC/cm^2 , they are only around 10-12 times thicker than the 1 mC/cm^2 films due to most of the charge used by OER during electrodeposition. Thicker films are more OER active actually due to larger area and sites, and possibly larger intake of Fe traces from the borate deposition solution.

The following number of moles of Ni, charge and equivalent Ni(OH)_2 thickness were calculated for the thicker films in Figure 3.9. $\text{Ni}_{0.6}\text{Fe}_{0.4}\text{O}_x\text{H}_y)_{100\text{mC}}$ (8.0 mC/cm^2 as-deposited) in 1 M Fe-free KOH contained 69 nmol/cm^2 , which decreased to 51 nmol/cm^2 after Tafel. $\text{NiO}_x\text{H}_y)_{100\text{mC}}$ (11.9 mC/cm^2 as-deposited) in Fe-free KOH contained 103 nmol/cm^2 , which decreased to 72 nmol/cm^2 after Tafel. While $\text{Ni}_{0.6}\text{Fe}_{0.4}\text{O}_x\text{H}_y)_{100\text{mC}}$ (6.2 mC/cm^2 as-deposited) in 1 M KOH contained 53 nmol/cm^2 , which decreased to 43 nmol/cm^2 after Tafel. $\text{NiO}_x\text{H}_y)_{100\text{mC}}$ (12.6 mC/cm^2 as-deposited) in KOH contained in 109 nmol/cm^2 , which decreased to 68 nmol/cm^2 after Tafel.

OER currents of $\text{NiO}_x\text{H}_y)_{100\text{mC}}$ and $\text{Ni}_{0.6}\text{Fe}_{0.4}\text{O}_x\text{H}_y)_{100\text{mC}}$ increased with anodization in 1 M KOH, and the redox peaks slightly shifted anodically for $\text{Ni}_{0.6}\text{Fe}_{0.4}\text{O}_x\text{H}_y)_{100\text{mC}}$ while only the cathodic peak slightly shifted anodically for $\text{NiO}_x\text{H}_y)_{100\text{mC}}$ (almost no change in the anodic peak).

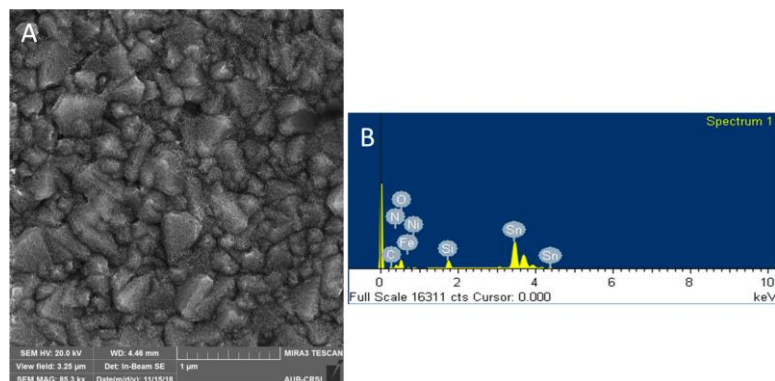


Figure 3.10: SEM image (A) and EDX spectrum (B) of an as-deposited $\text{Ni}_{0.6}\text{Fe}_{0.4}\text{O}_x\text{H}_y)_{100\text{mC}}$ film. Figure used with permission from ACS; ACS *Catalysis* **2020** *10* (1), 20-35, <https://pubs.acs.org/doi/10.1021/acscatal.9b02580>.⁸² Further permissions related to the material excerpted should be directed to ACS.

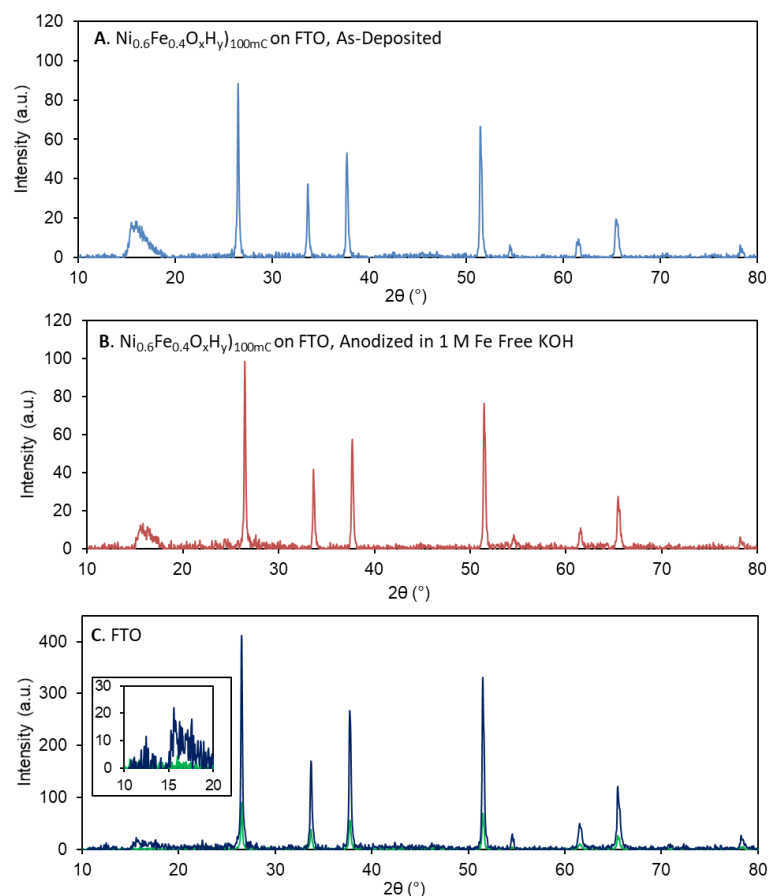


Figure 3.11: Powder X-ray diffraction (XRD) patterns for $\text{Ni}_{0.6}\text{Fe}_{0.4}\text{O}_x\text{H}_y$)_{100mC} on FTO, as-deposited (A) and anodized in 1 M Fe-free KOH (B), and two different FTO electrodes (C). Figure used with permission from ACS; *ACS Catalysis* **2020** *10* (1), 20-35, <https://pubs.acs.org/doi/10.1021/acscatal.9b02580>.⁸² Further permissions related to the material excerpted should be directed to ACS.

Figure 3.10 shows an SEM image of as-deposited $\text{Ni}_{0.6}\text{Fe}_{0.4}\text{O}_x\text{H}_y$)_{100mC}, which features nanoflake-like structures, and an EDX spectrum identifying both the Ni and Fe peaks. Figure 3.11 shows XRD spectra of $\text{Ni}_{0.6}\text{Fe}_{0.4}\text{O}_x\text{H}_y$)_{100mC} as-deposited (A) and anodized in 1 M Fe-free KOH (B) which only showed peaks characteristic of the FTO electrode (C), confirming the amorphous nature of the films reported by Nocera et al.⁹⁶ XRD spectra were also acquired for NiO_xH_y)_{100mC} and $\text{Ni}_{0.6}\text{Fe}_{0.4}\text{O}_x\text{H}_y$)_{100mC} as-deposited

and anodized in 1 M KOH and 1 M Fe-free KOH and showed similar results. The broad peak at around 15° in spectra A and B was seen in XRD spectra of some FTO surfaces (C, blue), though can be removed (C, green) with cleaning immediately prior to acquiring a spectrum, and therefore cannot be attributed to $\text{Ni}(\text{OH})_2$. Dinča et al. also reported similar findings with thick Ni-Bi films electrodeposited on ITO electrodes at 1 C/cm^2 showing only ITO diffraction peaks.⁵ The latter films were previously reported to be amorphous with ~ 2 nm nanocrystalline domains.⁹³

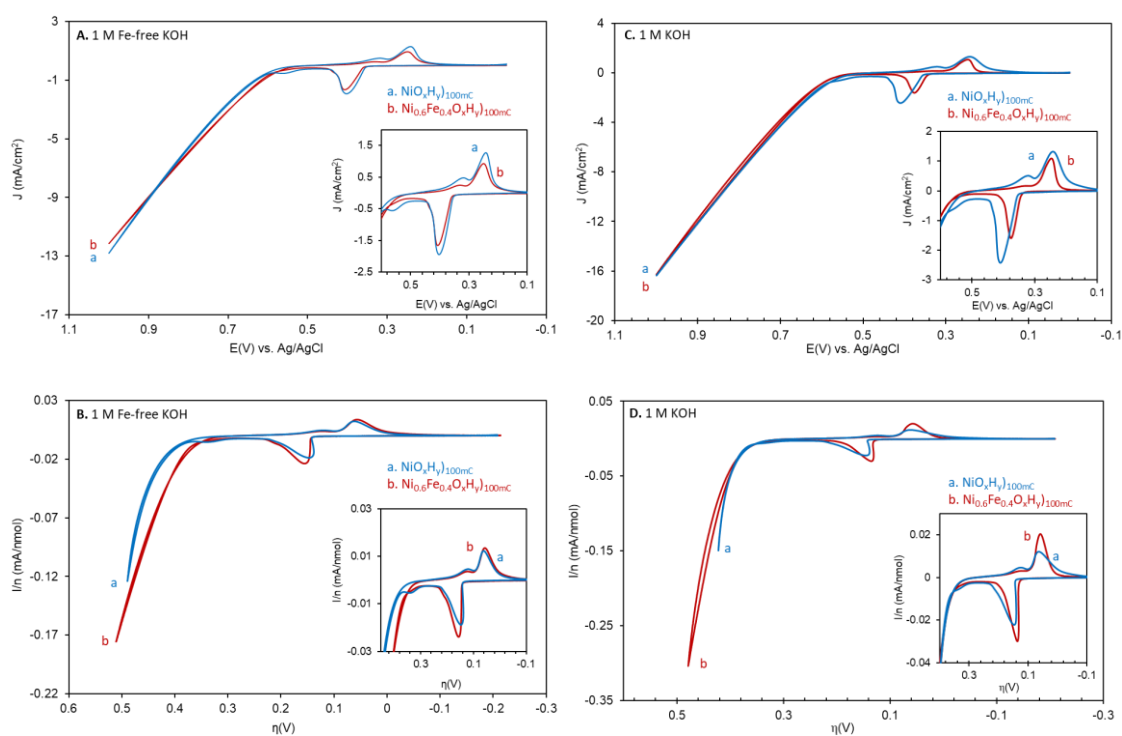


Figure 3.12: Cyclic Voltammograms, J (mA/cm^2) versus E (V) vs. Ag/AgCl (A, C), and normalized cyclic voltammograms, I/n (mA/nmol) versus η (V) (B, D), at NiO_xH_y _{100mC} (a, blue) and $\text{Ni}_{0.6}\text{Fe}_{0.4}\text{O}_x\text{H}_y$ _{100mC} (b, red) in 1 M Fe-free KOH (A-B) and in 1 M KOH (C-D) as a first scan. The insets show the $\text{Ni}(\text{OH})_2/\text{NiOOH}$ redox peaks and the onset of oxygen evolution for the three scans shown at each film. Scan rate is 10 mV/s. Figure used with permission from ACS; *ACS Catalysis* **2020** 10 (1), 20-35, <https://pubs.acs.org/doi/10.1021/acscatal.9b02580>.⁸² Further permissions related to the material excerpted should be directed to ACS.

The results do not show that OER activity of as-deposited $\text{Ni}_{0.6}\text{Fe}_{0.4}\text{O}_x\text{H}_y$)_{100mC} was higher than that of NiO_xH_y)_{100mC} when normalized to Ni content. Figure 3.12 shows CVs and normalized CVs (current divided by number of moles of active Ni vs. overpotential) of NiO_xH_y)_{100mC} and $\text{Ni}_{0.6}\text{Fe}_{0.4}\text{O}_x\text{H}_y$)_{100mC} in 1 M KOH and 1 M Fe-free KOH. CVs showed a similar OER onset between NiO_xH_y)_{100mC} and $\text{Ni}_{0.6}\text{Fe}_{0.4}\text{O}_x\text{H}_y$)_{100mC} in both solutions while normalized CVs showed better OER activity for $\text{Ni}_{0.6}\text{Fe}_{0.4}\text{O}_x\text{H}_y$)_{100mC} in 1 M Fe-free KOH but comparable activity in 1 M KOH with variation was observed for different films. Anodic co-deposition of Fe with Ni does not mainly lead to the placement of Fe in OER active sites, but during application of anodic bias for 30 min, Fe traces from KBi can calculate $\text{Ni}(\text{OH})_2$ sites for OER. Thicker $\text{Ni}_{0.6}\text{Fe}_{0.4}\text{O}_x\text{H}_y$)_{100mC} films, similar to thin $\text{Ni}_{0.6}\text{Fe}_{0.4}\text{O}_x\text{H}_y$)_{1mC}, needed anodic conditioning in Fe containing KOH to reach maximum OER activity even with its higher Fe content and longer deposition time in the presence of Fe in solution. $\text{Ni}_{0.6}\text{Fe}_{0.4}\text{O}_x\text{H}_y$)_{100mC} anodized in 1 M Fe-free KOH exhibited a moderate increase in OER activity at high potentials but with no change in OER onset and slight hysteresis. A decrease in currents at high potential was seen after Tafel but also with no change in onset and increased hysteresis, similar to $\text{Ni}_{0.6}\text{Fe}_{0.4}\text{O}_x\text{H}_y$)_{1mC} in 1 M Fe-free KOH. NiO_xH_y)_{100mC} showed comparable results but with almost no change in currents after anodization.

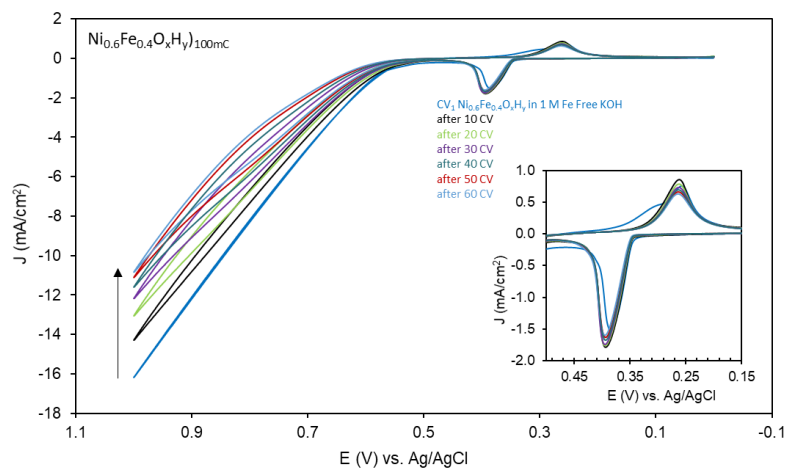


Figure 3.13: Cyclic voltammograms of $\text{Ni}_{0.6}\text{Fe}_{0.4}\text{O}_x\text{H}_y)_{100\text{mC}}$ film in 1 M Fe-free KOH, as a first scan (CV_1 blue) and then CVs acquired after 10 CVs were taken at 100 mV/s, repeated 6 times in the same solution. Scan rate of all CVs in this figure is 10 mV/s. The insets show the $\text{Ni}(\text{OH})_2/\text{NiOOH}$ redox peaks. The number of CVs (10-60) refers to the total number of scans acquired at 100 mV/s. Figure used with permission from ACS; *ACS Catalysis* **2020** *10* (1), 20-35, <https://pubs.acs.org/doi/10.1021/acscatal.9b02580>.⁸² Further permissions related to the material excerpted should be directed to ACS.

Figure 3.13 shows the potential cycling of $\text{Ni}_{0.6}\text{Fe}_{0.4}\text{O}_x\text{H}_y)_{100\text{mC}}$ in 1 M Fe-free KOH. This resulted in a less active catalyst with a progressive decrease in OER activity, a positive shift in OER onset (to higher potential) and an increase in hysteresis similar to results of the ultrathin films.

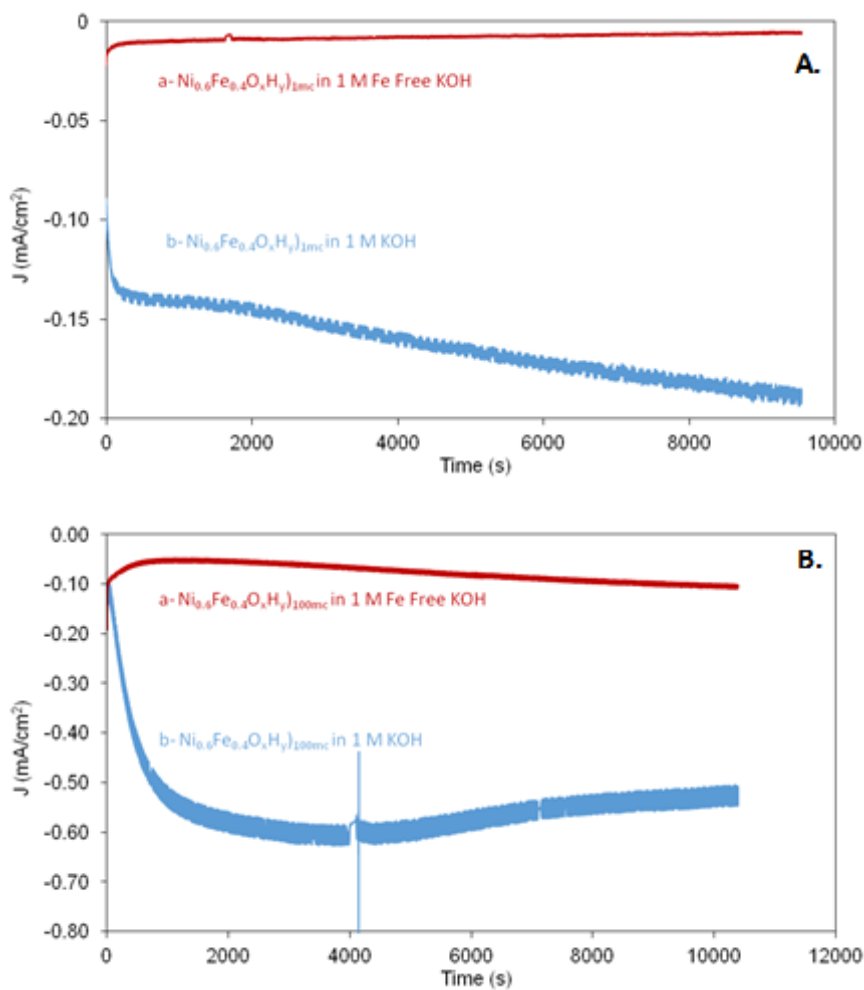


Figure 3.14: Anodization plots (i-t plots) of ultra-thin $\text{Ni}_{0.6}\text{Fe}_{0.4}\text{O}_x\text{H}_y$)_{100nm} (A) and thicker $\text{Ni}_{0.6}\text{Fe}_{0.4}\text{O}_x\text{H}_y$)_{1000nm} (B) films biased at 0.5 V vs. Ag/AgCl in 1 M Fe-free KOH (a, red traces) or unpurified 1 M KOH (b, blue traces) as indicated. Figure used with permission from ACS; *ACS Catalysis* **2020** 10 (1), 20-35, <https://pubs.acs.org/doi/10.1021/acscatal.9b02580>.⁸² Further permissions related to the material excerpted should be directed to ACS.

Figure 3.14 shows the anodization i-t curves of $\text{Ni}_{0.6}\text{Fe}_{0.4}\text{O}_x\text{H}_y$)_{100nm} (A) and $\text{Ni}_{0.6}\text{Fe}_{0.4}\text{O}_x\text{H}_y$)_{1000nm} (B) in 1 M Fe-free KOH (a) and 1 M KOH (b). OER currents decreased then slightly increased in 1 M Fe-free KOH at $\text{Ni}_{0.6}\text{Fe}_{0.4}\text{O}_x\text{H}_y$)_{1000nm} while the

currents greatly increased in 1 M KOH similar to thinner films. The slight increase in OER activity in thicker $\text{Ni}_{0.6}\text{Fe}_{0.4}\text{O}_x\text{H}_y$ films in 1 M Fe-free KOH (not observed in thinner $\text{Ni}_{0.6}\text{Fe}_{0.4}\text{O}_x\text{H}_y$ films) may be due to the larger amount of Fe in the film that might have leached out of the bulk and reactivated certain sites. $\text{NiO}_x\text{H}_y)_{100\text{mC}}$ showed a similar increase in current with anodization in 1 M Fe-free KOH (followed by a decrease after Tafel) which might be due to activation of Fe included from traces in the deposition solution.

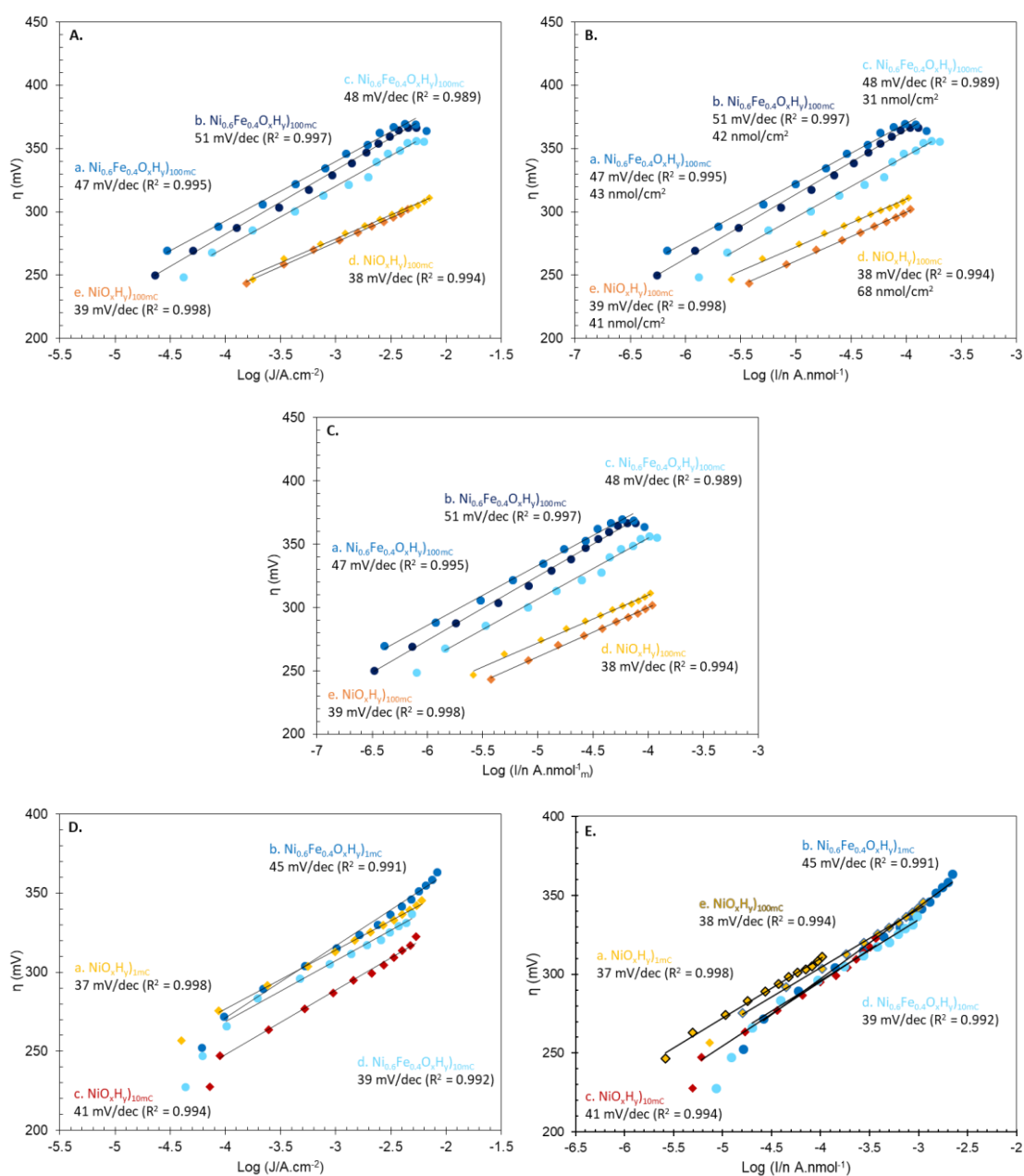


Figure 3.15: Tafel plots (A) and normalized Tafel plots (B) (C) for $\text{Ni}_{0.6}\text{Fe}_{0.4}\text{O}_x\text{H}_y$)_{100mC} (a-c) and NiO_xH_y)_{100mC} (d-e) films anodized in 1 M unpurified KOH and measured in the same solutions. Normalization was done using $1.2e/\text{Ni}$ for nmol of Ni (B) and for determining nmol of metal, assuming 40% Fe content, for $\text{Ni}_{0.6}\text{Fe}_{0.4}\text{O}_x\text{H}_y$)_{100mC} (C). Tafel plots (D) and normalized Tafel plots (E) for NiO_xH_y)_{1mC} (a), $\text{Ni}_{0.6}\text{Fe}_{0.4}\text{O}_x\text{H}_y$)_{1mC} (b), NiO_xH_y)_{10mC} (c) and $\text{Ni}_{0.6}\text{Fe}_{0.4}\text{O}_x\text{H}_y$)_{10mC} (d) films anodized in 1 M KOH and measured in the same solutions. Normalization was done using $1.2e/\text{Ni}$ for determining nmol of Ni in (E). Plot (d) from (B) has been added in (E) for comparison. Number of mole of Ni are calculated from post-Tafel. Note that Hg/HgO was used for one of the Tafel plots of NiO_xH_y)₁₀₀ (orange. A and B), in the rest used Ag/AgCl. Copyright Figure used with permission from ACS; *ACS Catalysis* **2020** 10 (1), 20-35, <https://pubs.acs.org/doi/10.1021/acscatal.9b02580>.⁸² Further permissions related to the material excerpted should be directed to ACS.

Figure 3.15 shows the Tafel plots and normalized Tafel plots of $\text{NiO}_x\text{H}_y)_{100\text{mC}}$ and $\text{Ni}_{0.6}\text{Fe}_{0.4}\text{O}_x\text{H}_y)_{100\text{mC}}$ in 1 M Fe-free KOH and 1 M KOH. $\text{Ni}_{0.6}\text{Fe}_{0.4}\text{O}_x\text{H}_y)_{100\text{mC}}$ and $\text{NiO}_x\text{H}_y)_{100\text{mC}}$ films of Figure 3.9.A exhibited Tafel slopes of 106 and 152 mV/dec in 1 M Fe-free KOH, respectively, and 47 and 38 mV/dec in 1 M KOH, respectively. The Tafel slopes were comparable to those of the thinner films confirming that OER activity is still low in the absence of Fe in solution even with Fe codeposition at higher loading. Tafel and normalized Tafel plots in 1 M KOH showed the lower OER activity of $\text{Ni}_{0.6}\text{Fe}_{0.4}\text{O}_x\text{H}_y)_{100\text{mC}}$ with respect to $\text{NiO}_x\text{H}_y)_{100\text{mC}}$, even when $\text{Ni}_{0.6}\text{Fe}_{0.4}\text{O}_x\text{H}_y)_{100\text{mC}}$ was normalized to nmol of Ni by assuming 40% Fe content to determine total nmol of metal (Figure 3.15.C). This normalization was done to take into account the total metal content in the co-deposited catalyst films (and not only the Ni content). Normalized Tafel plots of the thinner $\text{Ni}_{0.6}\text{Fe}_{0.4}\text{O}_x\text{H}_y)_{1\text{mC}}$, $\text{NiO}_x\text{H}_y)_{1\text{mC}}$, $\text{Ni}_{0.6}\text{Fe}_{0.4}\text{O}_x\text{H}_y)_{10\text{mC}}$ and $\text{NiO}_x\text{H}_y)_{10\text{mC}}$ showed similar activity in 1 M KOH (Figure 3.15).

Tafel plots and normalized Tafel plots of $\text{NiO}_x\text{H}_y)_{100\text{mC}}$ and $\text{Ni}_{0.6}\text{Fe}_{0.4}\text{O}_x\text{H}_y)_{100\text{mC}}$ in 1 M Fe-free KOH show a greater activity at $\text{Ni}_{0.6}\text{Fe}_{0.4}\text{O}_x\text{H}_y)_{100\text{mC}}$ (Figure 3.16- a, b, c) but this was not the general trend as other films showed variations (Figure 3.16- d, e). This might be due to the amount of Fe traces left in the purified.

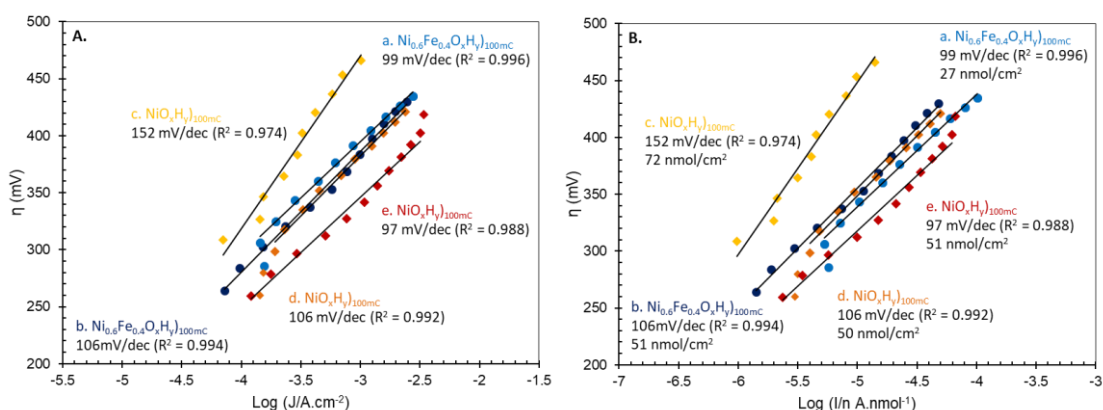


Figure 3.16: Tafel plots (A) and normalized Tafel plots (B) for $\text{Ni}_{0.6}\text{Fe}_{0.4}\text{O}_x\text{H}_y$ (a-b) and NiO_xH_y (c-e) films anodized in 1 M Fe-free KOH and measured in the same solutions. Normalization was done using $1.2e/\text{Ni}$ for determining nmol of Ni in (B). Number of mole of Ni is calculated from post-Tafel measurements. Figure used with permission from ACS; *ACS Catalysis* **2020** 10 (1), 20-35, <https://pubs.acs.org/doi/10.1021/acscatal.9b02580>.⁸² Further permissions related to the material excerpted should be directed to ACS.

Differences in electronic and mass transport resistance in films of various thicknesses leads to a variation in their OER activity with loading.¹²⁷ Electron and mass transport will depend on morphology and deposition techniques. Batchellor et al. reported that continuous cathodically deposited films resulted in decreased TOF with increasing film loading, but pulse deposited films resulted in increased TOF with loading.¹²⁷ It is possible that 1) higher Fe content in thicker films, 2) structural changes during anodization and 3) uptake of Fe from solution lead to changes in morphology and Fe distribution in the film. These changes possibly affect electronic and mass transport resistances and cause lower TOF at $\text{Ni}_{0.6}\text{Fe}_{0.4}\text{O}_x\text{H}_y$. As the lower activity of $\text{Ni}_{0.6}\text{Fe}_{0.4}\text{O}_x\text{H}_y$ was only seen in 1 M KOH, then it is related to the catalyst's

transformations specifically in this electrolyte and not its deposition. On the other hand, other $\text{Ni}_{0.6}\text{Fe}_{0.4}\text{O}_x\text{H}_y$)_{100mC} films in KOH maintained the general trend of increase in activity with increased loading possibly due to having no changes in nanostructuring at higher thicknesses.

b. Effect of Fe on Redox Peak Behavior

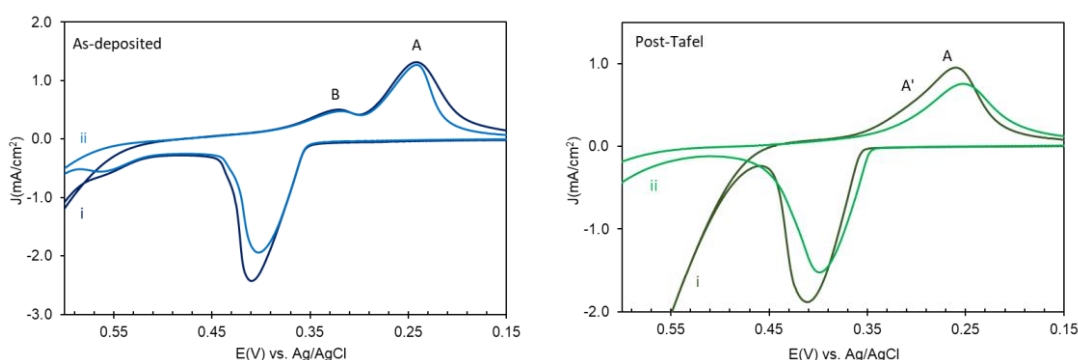


Figure 3.17: Cyclic Voltammograms acquired at 10 mV/s, between the same scan limits as in Figure 3.9, showing the region of the redox peaks and onset of oxygen evolution for NiO_xH_y)_{100mC} in unpurified 1 M KOH (i) and in Fe-free 1 M KOH (ii) as-deposited (blue) and after-Tafel measurements (green). Figure used with permission from ACS; *ACS Catalysis* **2020** *10* (1), 20-35, <https://pubs.acs.org/doi/10.1021/acscatal.9b02580>.⁸² Further permissions related to the material excerpted should be directed to ACS.

CVs of as-deposited NiO_xH_y)_{100mC} show minor redox peaks, denoted B, at 0.32 and 0.56 V in 1 M Fe-free KOH and at 0.32 and 0.55 V in 1 M KOH before the OER onset and at more positive potentials than the major redox peaks, denoted A, at 0.241 and 0.402 V in 1 M Fe-free KOH and at 0.242 and 0.410 V in 1 M KOH (Figure 3.17). These peaks are hypothesized to be for a quasi-reversible process possibly corresponding to one couple since the peaks cannot be seen in CVs after aging or

potential scanning.⁸² A cathodic shoulder can also be seen in $\text{Ni}_{0.6}\text{Fe}_{0.4}\text{O}_x\text{H}_y)_{1\text{mC}}$ and $\text{NiO}_x\text{H}_y)_{1\text{mC}}$ due to oxidation peak B merging with the OER onset. Boettcher et al. reported that small amounts of Ni(IV) at edge and corner sites or other sites is possibly linked to an oxidation peak at 0.6 V vs. Hg/HgO.⁹⁴ It can be that certain sites such as Ni edge and corner sites in $\alpha\text{-Ni(OH)}_2/\gamma\text{-NiOOH}$ are linked to the B peaks. Their disappearance could be due to the smoothing of these sites with dissolution/redeposition with no reformation with overcharging or potential scanning.

The major redox peaks in thicker as-deposited films is made of two combined peaks A and A'. The observed peak splitting might not be related to the increase in OER activity but Fe inclusion since it is also seen in CVs of $\text{NiO}_x\text{H}_y)_{1\text{mC}}$ after the addition of 0.16 mM Al^{3+} to 1 M Fe-free KOH (Figure 4.5). Though peak splitting was accompanied with an increase in OER activity for ultrathin films in 1 M KOH, greater splitting was seen after Tafel with a slight decrease or no change in activity. Hence, maximum activity could have been achieved at a certain surface Fe loading. A' was even observed in CVs of as-deposited thicker films due to the longer deposition time leading to Fe inclusion as both bulk Fe and surface Fe. Thus, the A' redox process is either due to Ni active sites with Fe inclusion or Ni neighboring Fe active sites as the A' peak is more dependent on the presence of Fe in solution.⁸²

The observed anodic wave at 0.75 V in 1 M Fe-free KOH is possibly attributed to the overcharging of $\beta\text{-NiOOH}$ to $\gamma\text{-NiOOH}$.⁸² Klaus et al. have previously reported an anodic peak at 0.7 V vs. Hg/HgO in Fe-free KOH which shifts anodically with aging accompanied by a decrease in OER activity.⁷⁷ A decrease in OER activity and increase in hysteresis but with no shift in A peaks was seen with CVs of $\text{NiO}_x\text{H}_y)_{1\text{mC}}$ after Tafel and after potential scanning in 1 M Fe-free KOH. The absence of shift in A peaks could

be due to γ -NiOOH, formed after overcharging, reducing directly to β -Ni(OH)₂ at potentials close to that for β -NiOOH, or the peaks being linked to a mixed α/β to γ/β transformation in thin films in Fe-free KOH.⁸²

B. Sustainability of the Active Site in the Absence of Fe in Solution

The ability of the catalyst films to sustain their OER activity if they were activated initially postdeposition in Fe-containing solution and then moved to an Fe-free solution was investigated. NiO_xH_y films were deposited at 1 and 10 mC/cm² and anodized in 1 M Fe-containing KOH, then potentially cycled in 1 M Fe-free KOH. Figure 3.18 and 3.19 show the CVs of NiO_xH_y)_{1mC} and NiO_xH_y)_{10mC}, respectively: a first scan CV in 1 M Fe-free KOH (i), a first scan CV in 1 M KOH followed by anodization in this solution and a post-anodization CV (ii), a post-anodization CV in 1 M Fe-free KOH followed by potential cycling in 10 CVs at 100 mV/s and a CV at 10 mV/s acquired at 10 mV/s, repeated n times where $6 \leq n \leq 25$ (iii).

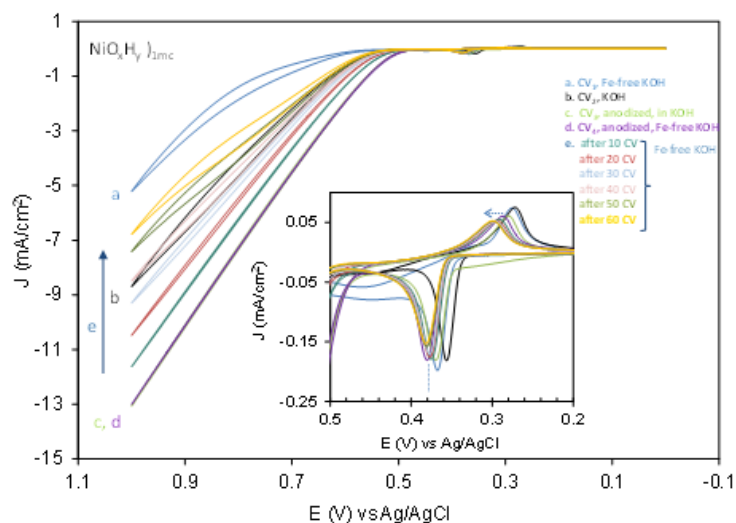


Figure 3.18: Cyclic Voltammograms for $\text{NiO}_x\text{H}_y)_{1mC}$ as (a) a first scan for the as-deposited film in 1 M Fe-free KOH, (b) a second scan after the film was moved to 1 M KOH, (c) after anodization in 1 M KOH, (d) after the anodized film was moved back into Fe-free KOH, and (e) scans acquired in Fe-free KOH after increments of 10 CVs were taken at 100 mV/s in this solution, this was repeated 6 times; some of the CVs are shown. Scan rate is 10 mV/s. Figure used with permission from ACS; ACS

Catalysis **2020** *10* (1), 20-35, <https://pubs.acs.org/doi/10.1021/acscatal.9b02580>.⁸²

Further permissions related to the material excerpted should be directed to ACS.

The initial CV of as-deposited $\text{NiO}_x\text{H}_y)_{1mC}$ in 1 M Fe-free displayed lower OER activity than that in 1 M KOH (Figure 3.18). While the CVs after anodization in both solutions had similar OER activity with a 9 mV cathodic shift in $E_{1/2}$ of major redox peaks in 1 M Fe-free KOH. The OER activity progressively decreased with potential cycling in 1 M Fe-free KOH accompanied with the appearance of a second oxidation wave and an increase in hysteresis. The number of moles of active Ni in the film equaled to 4.94 nmol/cm² in the first CV in Fe-free KOH after anodization which slightly decreased after 60 CVs to 4.46 nmol/cm² proving that the decrease in OER

activity was not due to the dissolution of Ni. An anodic shift of 8 mV in $E_{1/2}$ was seen in the cathodic peak after cycling with a decrease in peak separation from 93 mV to 82 mV.

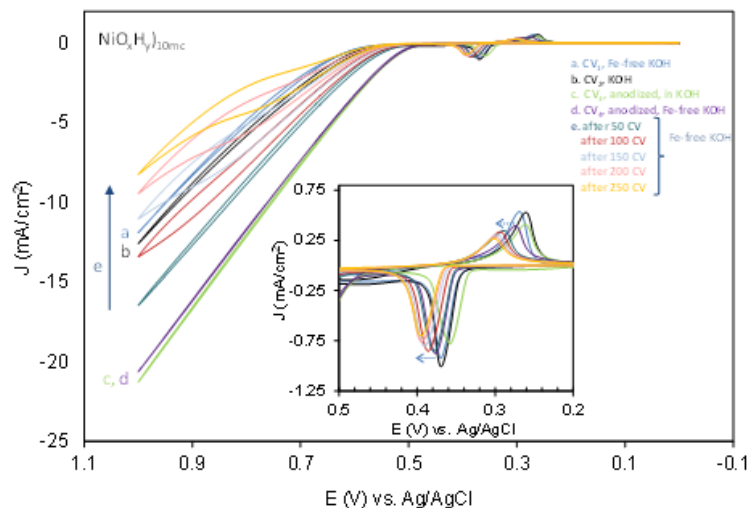


Figure 3.19: Cyclic Voltammograms for $\text{NiO}_x\text{H}_y)_{10\text{mC}}$ as (a) a first scan for the as-deposited film in 1 M Fe-free KOH, (b) a second scan after the film was moved to 1 M KOH, (c) after anodization in 1 M KOH, (d) after the anodized film was moved back into Fe-free KOH, and (e) scans acquired in Fe-free KOH after increments of 10 CVs were taken at 100 mV/s in this solution, this was repeated 25 times; some of the CVs are shown. Scan rate is 10 mV/s. Figure used with permission from ACS; ACS

Catalysis **2020** 10 (1), 20-35, <https://pubs.acs.org/doi/10.1021/acscatal.9b02580>.⁸²

Further permissions related to the material excerpted should be directed to ACS.

A similar result was seen in $\text{NiO}_x\text{H}_y)_{10\text{mC}}$ with the same initial OER activity after anodization in both solutions and a decrease in activity after potential cycling in the purified solution (Figure 3.19). For this thicker film, potential scanning was done until the activity of the film decreased less than that of the as-deposited film with the appearance of the second wave and hysteresis. The amount of Ni in the film in the first

CV in Fe-free KOH after anodization equaled to 21 nmol/cm², slightly increased to 22 nmol/cm² after 60 CVs and then decreased to around 15 nmol/cm² after 250 CVs. No dissolution of Ni was seen after 60 CVs, but some dissolution was observed after 250 CVs, however, this does not explain the decrease in activity when compared to the amount of Ni (4.94 nmol/cm²) in anodized NiO_xH_y)_{10mC} scanned in Fe-free KOH after activation (Figure 3.18). Anodic and cathodic shifts in major redox peaks were seen after potential cycling with a 10 mV shift in E_{1/2} after 60 CVs (0.326 V to 0.336 V) followed by a 12 mV shift after 250 CVs (0.336 V to 0.348 V), and a decrease in ΔE_p from 103 to 92 mV after 60 CVs followed by a slight increase to 94 mV after 250 CVs. Thus, the electrochemical behavior of the film shows that the activated catalyst is reverting back to its original inactive form in the absence of Fe in solution, and the present Fe in the film was sufficient to stop inactivation in the Fe-free electrolyte.

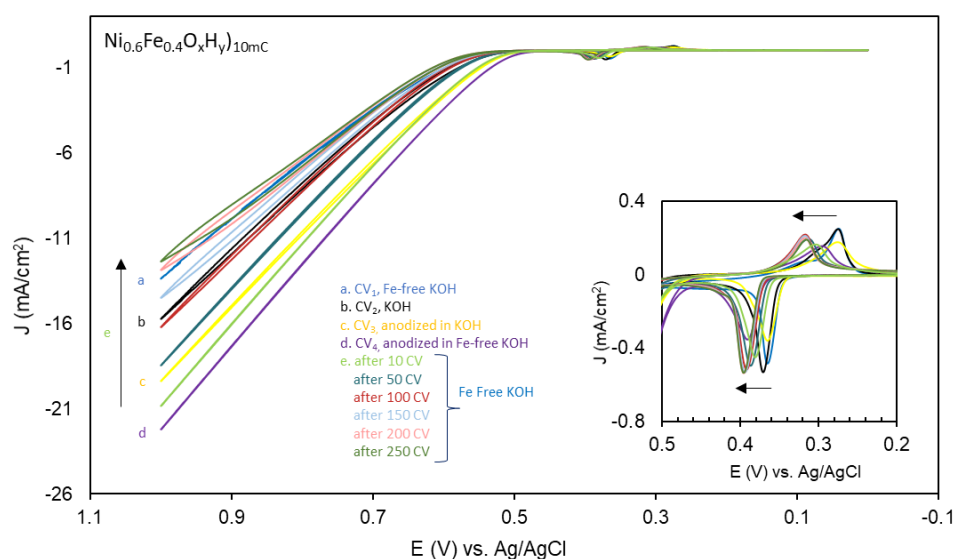


Figure 3.20: Cyclic voltammograms for Ni_{0.6}Fe_{0.4}O_xH_y)_{10mC} as follows: a) a first CV for the as-deposited film in 1 M Fe-free KOH, b) a second CV after the film was moved to 1 M KOH, c) CV after anodization in 1 M KOH, d) CV of anodized film moved back into 1 M Fe-free KOH, and e) CVs acquired in 1 M Fe-free KOH after increments of 10 CVs were taken at 100 mV/s in this solution, this was repeated 25 times, some of the CVs are shown. Scan rate is 10 mV/s. Figure used with permission from ACS; *ACS Catalysis* **2020** *10* (1), 20-35, <https://pubs.acs.org/doi/10.1021/acscatal.9b02580>.⁸² Further permissions related to the material excerpted should be directed to ACS.

Codeposited $\text{Ni}_{0.6}\text{Fe}_{0.4}\text{O}_x\text{H}_y$)_{10mC} showed similar results with an increase in OER activity after anodization in 1 M KOH followed by a gradual decrease in activity and increase in hysteresis with potential cycling in 1 M Fe-free KOH (Figure 3.20). A decrease of 19 mV in ΔE_p with no change in $E_{1/2}$ after the first 10 CVs was seen followed by an anodic shift of 13 mV in $E_{1/2}$ (343 to 356 mV). A cathodic shift in the anodic peak was also recorded after the first 10 CVs followed by an anodic shift which could imply an initial leaching of Fe. With continued cycling, an anodic shift was observed in $E_{1/2}$, and an increase in reversibility. Both are linked to the presence of Fe in $\text{Ni}(\text{OH})_2$.

C. Dependence of OER Activity at Ni(Fe)-Oxo/Hydroxide on the Presence of Fe in Solution

1. Possible Deactivation Mechanism

A Ni bulk site in $\text{Ni}(\text{OH})_2$ can be substituted by Fe or Fe can deposit on the catalyst surface. Carter et al. reported that the mechanistic path with low-coordination Fe in $\beta\text{-NiOOH}$ led to a decrease in OER overpotential based on DFT studies.¹¹⁴ In this work, supporting the previous claim, no promotion of OER activity in both ultrathin and thicker codeposited NiFe-oxo/hydroxo films was seen, and OER activity was not sustained in the absence of Fe in solution in both Fe-activated NiO_xH_y and $\text{Ni}_{0.6}\text{Fe}_{0.4}\text{O}_x\text{H}_y$ films. High Tafel slopes in the range of 100 mV/dec or higher were measured for ultrathin and thicker codeposited $\text{Ni}_{0.6}\text{Fe}_{0.4}\text{O}_x\text{H}_y$ films in Fe-free KOH. OER activity decreased after anodic conditioning in Fe-free KOH. Activation in Fe-

containing solution was needed for anodically codeposited NiFe-oxo/hydroxo films at 6:4 Ni:Fe ratio. These results support an initial hypothesis that Fe co-deposited during anodic co-deposition in bulk Ni(OH)₂ sites is not the cause of promotion of OER. It is thought that Fe occupies a surface site after incorporation from solution after deposition and is not in full coordination to lattice O atoms¹¹⁴ leading to films with high OER activity and Tafel slopes of 40 mV/dec. Even if activated, in the absence of Fe in solution, the active sites in the film are not sustained and thus return to an OER less active or inactive form. If Fe leaching out is the cause of this deactivation, then the probable Fe redeposition is forming inactive sites (with Ni redeposition after dissolution in KOH) as Fe traces in solution were the cause of the increased OER activity in unpurified KOH. Moreover, Fe leaching is generally accompanied by with a cathodic shift, a change in E_{1/2} or increased reversibility; all of which were not observed during film deactivation upon potential cycling in Fe-free solution. The anodic shifts support Fe moving to a bulk site.

Despite the dynamic nature of Ni(OH)₂ electrocatalysts, codeposited Fe is not leading to active OER catalysis via Fe relocation from an inactive bulk site to an active surface site. An anodic shift in major redox peaks is seen with deactivation of the films in Fe-free KOH similar to its activation after anodization in KOH and is an indication of Fe going in the NiO_xH_y bulk.¹²⁸ This transfer from surface to bulk Fe is hypothesized to be the reason behind the decrease in OER activity in Fe-free KOH. The anodic shift in major redox peaks previously reported did not appear in NiO_xH_y)_{1mC} films after anodization, Tafel or potential cycling in 1 M Fe-free KOH (Figure 3.1, 3.2 and 3.3). It can be concluded not be due to a phase transformation to β-Ni(OH)₂ whose redox peak potentials are more positive than α/γ.^{77, 80, 129} In addition, the decrease in peak separation

is also linked to surface Fe moving into the bulk leading to a decrease in OER activity. Increased reversibility is seen with an increase in reversibility of the α/γ couple and stabilization by Fe. In this study, similar to the reports of Corrigan⁹² and Fayad¹ et al., a decrease in peak separation and thus an increase in reversibility were reported with Fe codeposition in thicker films in both electrolytes: for $\text{Ni}_{0.6}\text{Fe}_{0.4}\text{O}_x\text{H}_y$)_{100mC}, $\Delta E_p = 121 \pm 22$ mV (N = 5) in Fe-free KOH and 127 ± 4 mV (N = 3) in 1 M KOH compared to NiO_xH_y)_{100mC}, $\Delta E_p = 145 \pm 14$ mV (N = 3) in Fe-free KOH and 157 ± 16 mV (N = 2) in 1 M KOH.

2. Examining Other Possibilities for Deactivation

Another explanation of deactivation in Fe-free solution is Fe leaching out of the film and not redepositing due to either low amounts of Fe in solution or absorption by traces of $\text{Ni}(\text{OH})_2$, dissolved from film or remaining colloids from the purification treatment. Boettcher et al. noted an increase in Ni-Bi peaks with cycling attributed to traces of Ni in KBi after purification from Fe, which we also saw in purified 1 M KBi.⁹⁵ This was not seen in $\text{Ni}(\text{OH})_2$ peaks in 1 M Fe-free KOH in our study. An FTO electrode was tested in the purified solution showing a decrease in the initially low OER activity with potential cycling (Figure 3.21). Therefore, there is no indication of Ni deposition.

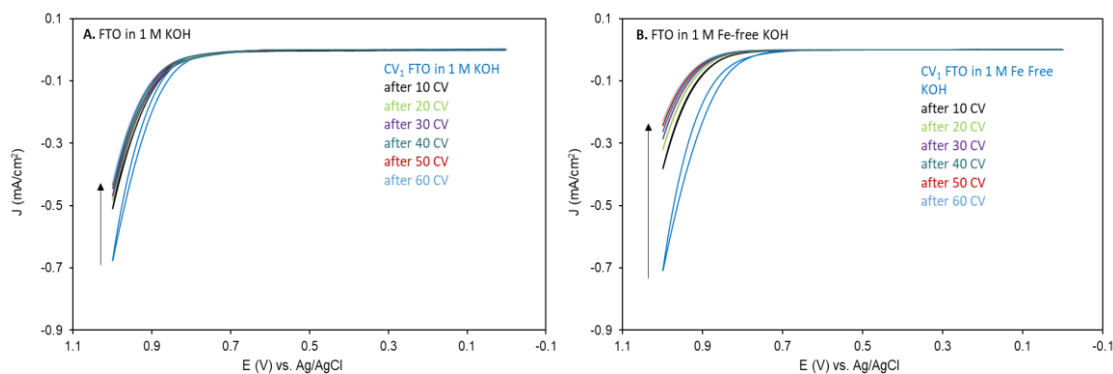


Figure 3.21: Cyclic voltammograms of FTO in 1 M KOH (A) and 1 M Fe-free KOH (B) as a first scan (CV_1 blue) and then CVs acquired after 10 CVs were taken at 100 mV/s, repeated 6 times in the same solution. Scan rate of all CVs in this figure is 10 mV/s. The number of CVs (10-60) refers to the total number of scans acquired at 100 mV/s. Figure used with permission from ACS; *ACS Catalysis* **2020** 10 (1), 20-35, <https://pubs.acs.org/doi/10.1021/acscatal.9b02580>.⁸² Further permissions related to the material excerpted should be directed to ACS.

Ni leaches out during catalysis or potential cycling as evidenced by the decrease in redox peak charges. Thus, the solution could have contained traces of Ni that can ‘absorb’ Fe from solution, or deposit on Fe sites. Fe-free KOH was spiked with nmol level Fe to simulate the amount of Fe supposedly leached during OER. 1.2 nmol of Fe^{3+} were added to 20 mL of 1 M Fe-free KOH equating to 25% of the Ni content in NiO_xH_y (1_{mC} (4.78 nmol/cm^2)) and a total of 60 nM Fe^{3+} (~ 3 ppb) in solution. This resulted in an increase in OER activity with anodization as seen in Figure 3.22 indicating that even this low Fe can get into active sites and activate the films. However, the activity was not sustained with potential cycling after anodization, and the loss of activity was accompanied by an anodic shift.

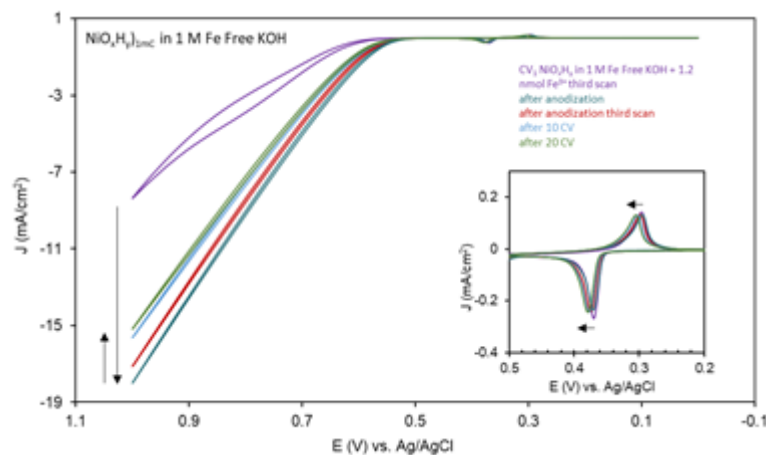


Figure 3.22: Cyclic voltammograms of $\text{NiO}_x\text{H}_y)_{1\text{mC}}$ film after the addition of 1.2 nmol Fe^{3+} and three scans in 1 M Fe-free KOH. CVs as first and third scan after anodic conditioning in the same solution were acquired. 10 CVs were taken at 100 mV/s in the same solution followed by a CV at 10 mV/s; this was repeated 2 times. Scan rate for the CVs in this figure is 10 mV/s. The number of CVs (10-20) refers to the total number of scans acquired at 100 mV/s. Figure used with permission from ACS; ACS *Catalysis* **2020** *10* (1), 20-35, <https://pubs.acs.org/doi/10.1021/acscatal.9b02580>.⁸² Further permissions related to the material excerpted should be directed to ACS.

OER currents decreased in another experiment with the addition of 1.2 nmol followed by potential cycling. Spiking was increased to 2.4 nmol of Fe, equivalent to 40% of Ni content in film, and led to an increase in OER activity with potential cycling, decreased hysteresis and anodic shift in redox peaks. A further addition to reach a total of 21 nmol of Fe significantly increased OER currents with the disappearance of hysteresis after the first 10 CVs. Further cycling lead to minimal change in activity but a gradual anodic shift in redox peaks (Figure 3.23). The experiments show that dissolution of Ni or its presence in Fe-free KOH because of the cleaning process that

used $\text{Ni}(\text{OH})_2$ is not preventing low amounts of Fe in solution from activating the films, supporting the proposed deactivation mechanism that Fe is moving to bulk sites.

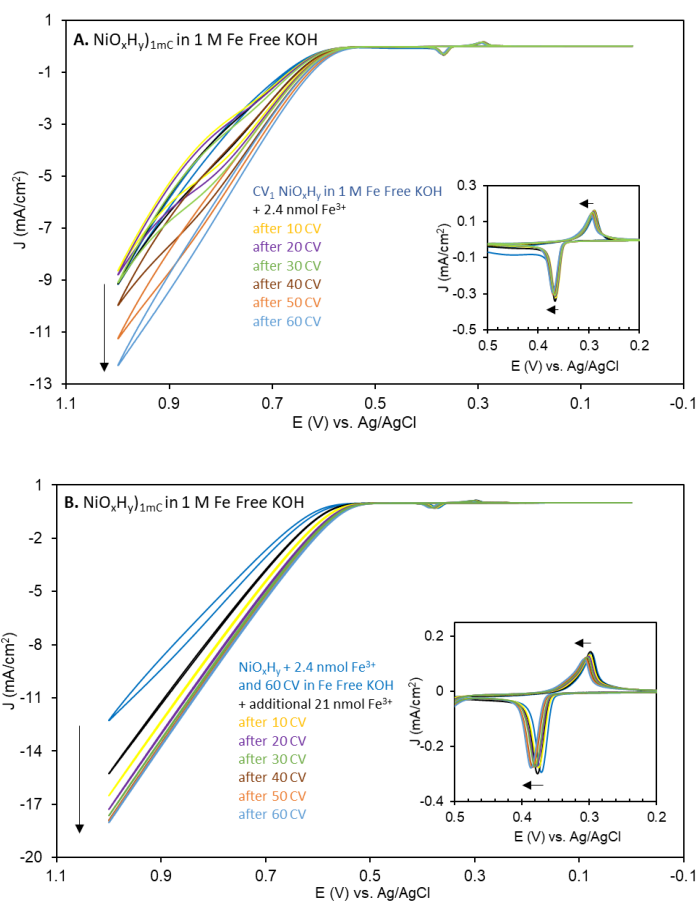


Figure 3.23: Cyclic voltammograms of NiO_xH_y film as a first scan in 1 M Fe-free KOH before and immediately after addition of 2.4 nmol Fe^{3+} . 10 CVs were acquired at 100 mV/s in the same solution followed by a CV at 10 mV/s; this was repeated 6 times (A). A CV was acquired immediately before and after the addition of a total of 21 nmol Fe^{3+} . 10 CVs were acquired at 100 mV/s followed by a CV at 10 mV/s; this repeated 6 times (B). Scan rate for the CVs in this figure is 10 mV/s. The inset shows the anodic shift in $\text{Ni}(\text{OH})_2/\text{NiOOH}$ redox peaks. The number of CVs (10-60) refers to the total number of scans acquired at 100 mV/s. Figure used with permission from ACS; *ACS Catalysis* **2020** *10* (1), 20-35, <https://pubs.acs.org/doi/10.1021/acscatal.9b02580>.⁸²

Further permissions related to the material excerpted should be directed to ACS.

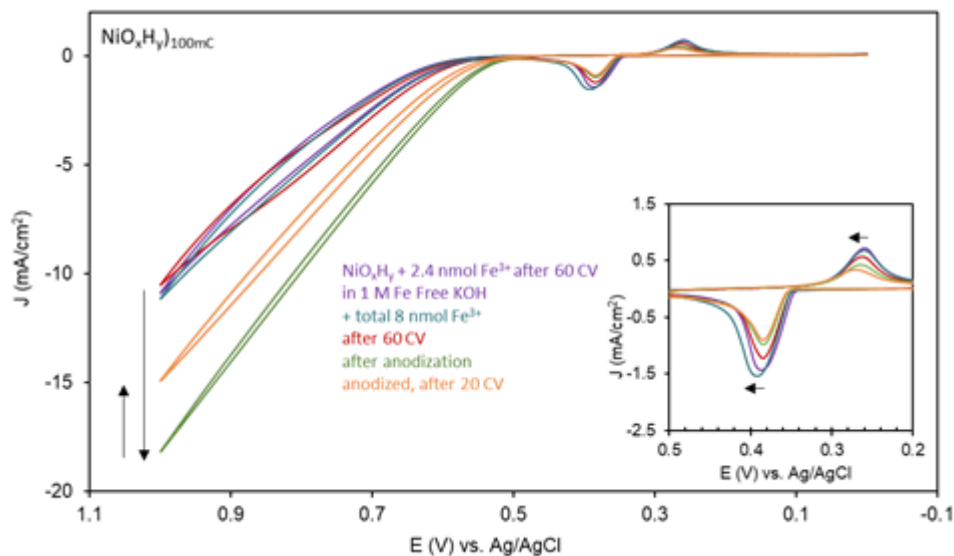


Figure 3.24: Cyclic voltammograms of $\text{NiO}_x\text{H}_y)_{100\text{mC}}$ film in 1 M Fe-free KOH after addition of 2.4 nmol Fe^{3+} and 60 CVs at 100 mV/s were acquired. A CV was acquired after the addition of a total of 8 nmol Fe^{3+} . Similarly, 10 CVs were acquired at 100 mV/s followed by a CV at 10 mV/s; this was repeated 6 times. A CV after anodization was taken followed by 10 CVs at 100 mV/s and a CV at 10 mV/s; this was repeated 2 times. Scan rate for the CVs in this figure is 10 mV/s. The inset shows the slight anodic shift in $\text{Ni(OH)}_2/\text{NiOOH}$ redox peaks post Fe^{3+} addition and anodic conditioning. The number of CVs (10-60) refers to the total number of scans acquired at 100 mV/s. Figure used with permission from ACS; *ACS Catalysis* **2020** 10 (1), 20-35, <https://pubs.acs.org/doi/10.1021/acscatal.9b02580>.⁸² Further permissions related to the material excerpted should be directed to ACS.

Similar experiments were conducted for thicker $\text{NiO}_x\text{H}_y)_{100\text{mC}}$ (69.5 nmol/cm²) films with 8 nmol Fe addition, an equivalent of ~ 10% of Ni content. Figure 3.24 showed no increase in OER activity with potential cycling but showed increase in OER with 1 h of anodization. However, with potential cycling after anodization, the activity

decreased and thus was not sustained at this low amount of Fe. This shows that a minimum amount of Fe is needed to sustain OER activity. Thus, deactivation is not due to the incapability of low levels of Fe in purified solution to activate OER sites but rather the relocation of active surface Fe to inactive bulk Fe (as seen with the anodic shift and increased reversibility).

3. Examining Possible Effects of Other Impurities

a. Examining the Effect of Pt Addition

The effects of metal impurities, other than Fe, from KOH electrolyte and counter electrolyte were briefly examined. In this work, Pt is used as the counter electrode as it is unaffected by anodic bias and will not form its oxide because it supports cathodic currents, and is known to be OER inactive.¹³⁰ Several previous studies have also used Pt as a counter electrode,^{77, 104, 131} and other studies have employed Pt as a substrate for OER catalysts.¹³¹⁻¹³² Nonetheless, redeposited Pt could possibly block or alter active sites in the catalyst leading to changes in its OER activity and electrochemistry. The effects of Pt leaching on the activity and electrochemical features of OER were examined before and after the KOH solutions were spiked with K_2PtCl_4 (aq) and cycled. Cathodic ORR and Pt-oxide reduction currents and HER/HOR currents were seen in the CV of $NiO_x(Hy)_{1mC}$ following the addition of 4 μ L of 50 mM K_2PtCl_4 (aq, aged) to aerated 1 M KOH thus indicating Pt deposition (Figure 3.25). Nonetheless, no changes in OER activity, cathodic NiOOH peak splitting and the anodic shift were observed after the addition of aged K_2PtCl_4 in both unpurified KOH and Fe-free KOH.⁸² Therefore, the Pt counter electrode has no effect on the OER activity and the electrochemical behavior of the working electrode in both electrolytes.

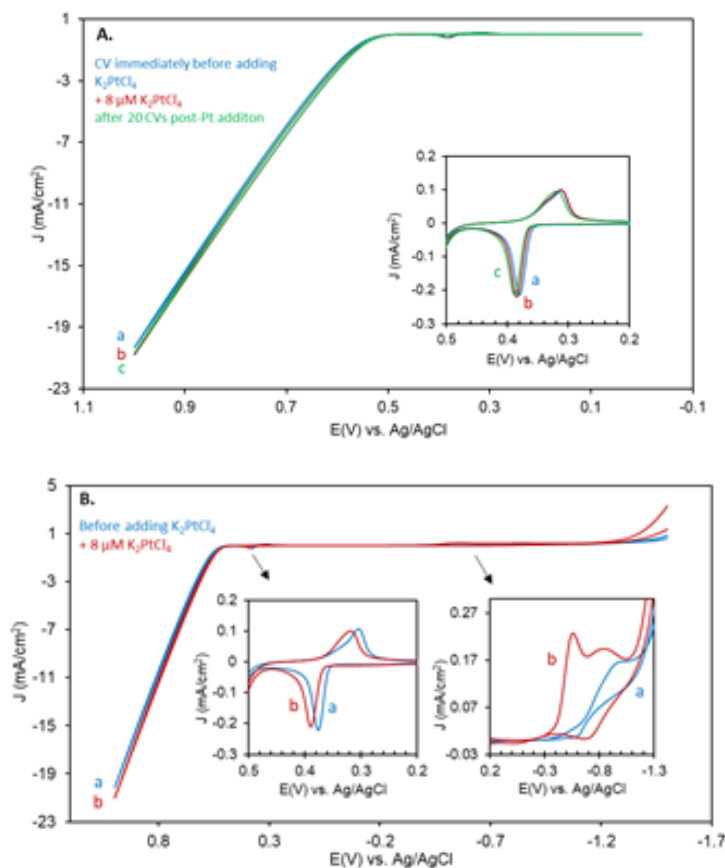


Figure 3.25: CVs of $\text{NiO}_x\text{H}_y)_{1\text{mC}}$ in unpurified (and aerated) 1 M KOH after 10 CVs at 100 mV/s immediately before (a, blue) and after the addition of 8 μM K_2PtCl_4 (b, red), and then after 20 CVs at 100 mV/s (c, green) showing the usual anodic shift and splitting of the peaks (A). A CV scan from -1.5 V to 1 V before (a, blue) and after the addition of 8 μM K_2PtCl_4 (b, red), note that there are 40 CVs at 100 mV/s between these two CVs hence the anodic shift in the peaks (B). Scan rate is 10 mV/s. Figure used with permission from ACS; *ACS Catalysis* **2020** 10 (1), 20-35, <https://pubs.acs.org/doi/10.1021/acscatal.9b02580>.⁸² Further permissions related to the material excerpted should be directed to ACS.

b. Discussion of Other Possible Impurities in KOH

KOH electrolyte also contains several impurities such as $\leq 0.0005\%$ Fe, $\leq 0.001\%$ Al, $\leq 0.0005\%$ Ni, and $\leq 0.0005\%$ heavy metals: Ag, As, Bi, Cd, Cu, Hg, Pb, Sb, Sn and Mo. Previous studies have reported that glass components of the setup etch in 1 M KOH and contaminate the solution with Fe and other elements such as Al, Pb, B and Si.^{94, 133-134} In this study, the glass components used were the FTO substrate, though low Fe content, the reference electrode enclosure, the cell, and solution containers. However, for Fe-free KOH measurements, plastic containers and cell were used. Subbaraman et al. reported the presence of traces of transition metals such as Co, Cu, Cr, Ni and Fe (though in smaller amounts of 11-23 fold more on average) in different sources of KOH (such as the one used in this work) after ICPMS analysis.¹³⁵ These transition metals could be found at concentrations higher than that of Fe, such as Al, or lower; nonetheless, these metals are able to replace Ni or Fe sites in Ni(OH)₂ and lead to various effects on OER activity and electrochemical behavior. Previous studies have reported that Co promotes the OER activity of Ni-oxide,¹²² Cr changes the film morphology¹¹⁵ and Al poisons the activity in KBi.¹ However, no study has been done on their combined effect at these low levels or if the purification also removes them, which requires further investigation.

4. Differences from Literature

a. Differences in Deposition Technique and Initial Catalyst Structure with Fe Co-deposition

Previous studies reported that deactivation of codeposited NiFe catalysts was not similarly seen in Fe-free KOH in contrast to this work.^{83, 92, 94, 136} Though the reasons

behind these differences in OER activity are still unclear, they can be attributed to the deposition technique and concentration and purification method of electrolyte used. The formation and sustainability of active sites and overall dynamics of Ni(Fe)O_xH_y catalysts is dependent on film loading (thickness), nature, pH and ionic strength of the electrolyte, as-deposited film structure, and substrate specifically for ultrathin films. Catalyst deposition techniques form a variety of crystalline and nanocrystalline sizes and preliminary Fe sites, and vary between studies but generally include cathodic deposition where the hydroxide is precipitated via increased pH due to nitrate reduction, anodic deposition, oxide synthesis, and spin coating followed by low-temperature annealing.^{76, 124, 137-140} Various crystalline domain sizes can be formed from anodic and cathodic deposition,^{62, 93-94, 96, 124, 130, 140} specifically amorphous catalysts via anodic deposition.^{5, 93, 140}

Interestingly, Fe is able to be deposited on Ni(OH)₂ films when an anodic bias is applied in the presence of Fe traces in solution, while thicker films, which were deposited also at an anodic bias for a longer time (30 min) in a solution of 4:6 Fe:Ni ratio, still needed further activation, indicating that the presence of Ni is blocking active sites. To understand this aspect more, further electrochemical studies and structural characterizations are needed to investigate the effect of the different deposition techniques, film thicknesses, substrates and electrolyte composition.

b. Different Deposition Methods at Other Transition Metal Based OER Catalyst Systems

Boettcher et al. investigated the effect of mode of inclusion of Fe on the OER of cathodically and anodically deposited CoO_xH_y films in Fe-free KOH.¹²⁴ They reported a

decrease in activity of CoO_xH_y , which was previously activated from Fe in solution, with potential cycling in Fe-free KOH due to a 60% decrease in Fe content (Fe leaching) from surface and edge sites.¹²⁴ Cathodically codeposited $\text{Co(Fe)O}_x\text{H}_y$ films showed stable OER activity over potential cycling (20 cycles) in Fe-free KOH with only a 10% decrease in Fe.¹²⁴ Cathodically deposited CoO_xH_y showed no shift in redox peaks even after Fe inclusion from solution and OER activity decrease with cycling in Fe-free KOH due to weak interaction between this Fe and Co.¹²⁴ Anodically deposited CoO_xH_y showed two redox peaks after Fe inclusion and cycling due to a strong interaction between Co and Fe leading to the formation of an anodically shifted second peak.¹²⁴ Thus, the decrease in OER activity cannot be linked to this Fe which also was not easily removed with cycling in Fe-free KOH.¹²⁴ Anodically deposited CoO_xH_y also showed no further shift with potential cycling in Fe-free KOH even after its decrease in activity¹²⁴ which was in contrast to the behavior of $\text{Ni(Fe)O}_x\text{H}_y$ in this work. Thus, there is a general dependence of the dynamic nature of the active sites on the deposition method with certain differences between Ni- and Co- based films

D. Conclusions

This chapter investigated the effect of mode of inclusion of Fe on OER at NiO_xH_y in the presence and absence of Fe in solution. It is concluded from these studies that:

- 1) High OER activity is not due to Fe inclusion during $\text{Ni}_{0.6}\text{Fe}_{0.4}\text{O}_x\text{H}_y$ anodic deposition.

- 2) High OER activity is not retained in the absence of Fe in solution during catalysis at $\text{Ni(Fe)O}_x\text{H}_y$ films activated for OER in Fe-containing electrolyte after deposition. The hypothesis that high OER activity is due to Fe-activated surface sites rather than bulk-Fe inclusion is supported by the electrochemical behavior of the catalysts.
- 3) The deactivation mechanism likely behind the loss of OER activity of activated NiFe-oxo/hydroxide films in Fe-free KOH is due to Fe moving from active surface-Fe sites with low coordination to higher coordination bulk-Fe sites.
- 4) Future studies are needed to investigate the differences between surface and bulk phases of the catalyst, and the mechanism of dissolution and redeposition of the catalyst in the presence and absence of Fe in solution, and the optimum concentration of Fe in solution needed to sustain maximum OER catalysis at $\text{Ni(Fe)O}_x\text{H}_y$ films
- 5) Further studies are needed to investigate how the sustainability of the active site and any deactivation mechanism depend on different deposition methods as they lead to different initial phase crystallinity, and how this depends on film thickness.

CHAPTER IV

INVESTIGATION OF THE EFFECTS OF ALUMINUM IN NICKEL HYDROXIDE FILMS ON OXYGEN EVOLUTION REACTION CATALYSIS

With the increase in environmental awareness, the use of fossil fuels is gradually being replaced by alternative green energy sources such as wind and solar energy. A main concern with these methods lies in the storage of electrical energy for use during the time of day when production is scarce. Thus, recent studies have focused on the generation of hydrogen fuel via water splitting as a promising energy storage technique. To increase efficiency of this process, the slow kinetics of the oxygen evolution reaction^{23, 141-142} must be overcome with the use of transition non-noble metal electrocatalysts of high abundance, alkaline stability and activity such as cobalt and nickel.^{1, 29, 61, 77, 92, 101-105, 118-120, 122, 143} The incorporation of a second and third metal ion into the metal oxide has been shown to enhance or reduce activity depending on the nature of the additional ion.^{1, 29, 61, 77, 92, 101-105, 118-120, 122, 143} Ni-FeOOH has been reported to surpass the efficiency of its single metal counterpart, NiOOH, and even rare-metal oxides such as IrO₂ thus acting as highly efficient non-noble metal OER catalyst.¹⁰¹

Previous studies have shown that aluminum as a ternary metal in Ni-FeOOH enhances OER activity.^{103, 144-145} In other earlier work in our lab, we found that adding Al³⁺ to a solution of borate resulted in reducing the OER catalytic activity of the Ni-borate catalyst.¹ While other studies showed that codeposited Ni-Al oxide is as active as Ni-Fe oxide.^{103, 145} This prompted us to study the effect of Al in film or in solution and in the presence or absence of Fe. Aluminum acts as a substitutional dopant in Ni(OH)₂/NiOOH specifically stabilizing α -Ni(OH)₂ over β -Ni(OH)₂.¹⁴⁶⁻¹⁴⁹ Ni-AlOOH

films have had varying reported OER behavior as studied in Fe-containing electrolytes depending on their synthesis technique unlike Ni-FeOOH films.^{103, 144-145, 149-150} Baker et al. reported Ni-Al-Fe-OOH catalysts prepared via atomic layer deposited Ni-Al-O and preconditioned in KOH to form the oxyhydroxide phase and incorporate Fe into the film.¹⁴⁴ The catalyst enhanced OER activity compared to its Ni-OOH and Ni-Fe-OOH counterparts in Fe-containing 0.1 M KOH and slightly in 0.1 M Fe-free KOH.¹⁴⁴ They then suggested that Al does not act as an active site but does not negatively affect OER activity and instead promotes the active sites by inducing more negatively charged oxygen bridging ligands of Al (in comparison to those of Ni) which interact with neighboring Ni and Fe centers leading to an increase in their electron density.¹⁴⁴

As previously hypothesized by our group, the enhancement in OER activity post-anodization in Fe-containing electrolyte is due to surface site modification rather than bulk inclusion of Fe in NiFe-Bi films.¹ Supporting this claim, the addition of Al³⁺ into the electrolyte was found in an earlier study to suppress OER activity of the catalyst film while having a similar effect on the redox peak positions as the addition of Fe³⁺, which anodically shifted with potential cycling in the presence of Al as they do in the presence of Fe.¹

In the literature, Al doped Ni-based catalyst films were tested mainly in Fe-containing electrolytes with very scarce reports of testing in Fe-free electrolyte.^{1, 144-145} Thus, the effect of Al doping on its own, without the interference of Fe, is not fully understood. Al has been incorporated into Ni-oxide catalysts via electrochemical co-deposition, atomic layer deposition, calcination, powder precipitation and other methods^{1, 144-146, 149-150} Upon co-deposition, Al acts as a substitutional dopant replacing Ni in the Ni(OH)₂ lattice,¹⁴⁴ which we will refer to as “bulk Al”, similar to Fe. Similar

to the study with Fe, this work investigates differences in the effect of Al when included in the film during deposition of Ni(OH)₂ or post-deposition by adding Al³⁺ to the electrolyte and effect on OER catalysis in the presence and absence of Fe in solution during conditioning and during catalysis. The sustainability of OER catalysis in the absence of Fe in solution for NiAl-oxo/hydroxide films was questioned as well. Thus, the effect of mode of inclusion of Al in Ni-oxo/hydroxide films at different thickness, ultrathin and thicker films, on OER activity and electrochemical characteristics was studied in both Fe-containing KOH and KBi and in Fe-free KOH electrolytes.

A. Effect of the Al in Solution on Ni-oxo/hydroxide Films

Ni-oxo/hydroxide, NiO_xH_y, and Ni_{0.6}Al_{0.4}-oxo/hydroxide, Ni_{0.6}Al_{0.4}O_xH_y, films were deposited on FTO glass electrodes via anodic electrodeposition at 0.953 V vs. Ag/AgCl from 0.4 mM Ni(NO₃)₂ or mixed Ni(NO₃)₂:Al(NO₃)₃ of 6:4 ratio in 0.1 M KBi of pH ~ 9.20 at different thicknesses set by fixing the deposition charge at 1, 100 or 400 mC/cm². The deposition time of films with deposition charge 1 and 100 mC/cm² was in the range of 30-60 s and 1200-1600 s respectively. They were then rinsed and moved to a glass cell for testing in 1 M unpurified KOH or 1 M KBi or a non-glass polypropylene cell for testing in 1 M Fe-free KOH. Films are referred to according to their deposition charge, Ni:Al ratio in the deposition solution and electrolyte, such as Ni_{0.6}Al_{0.4}O_xH_y)_{1mC} in KOH and Ni_{0.6}Al_{0.4}-Bi)_{1mC} in KBi.

1. Effect of Al Addition in 1 M KBi on Electrochemical Behavior and OER of Ni-Bi

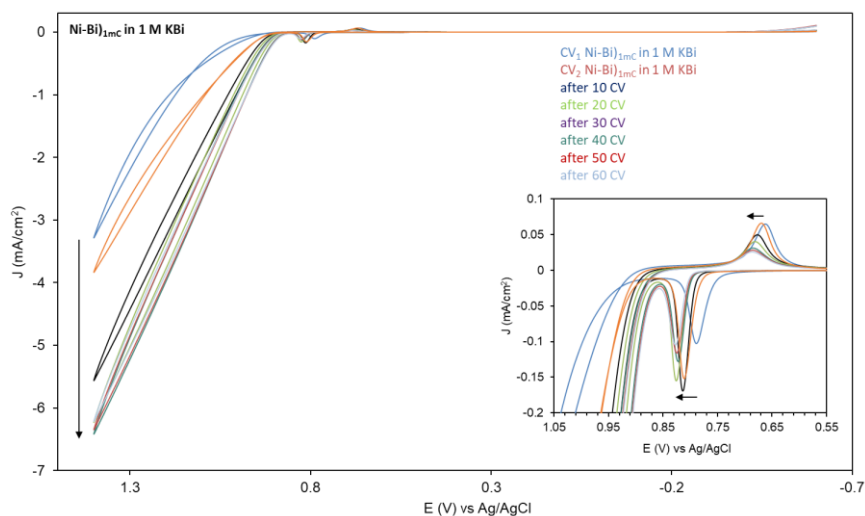


Figure 4.1: Cyclic voltammograms of Ni-Bi)_{1mC} film in 1 M KBi, as a first (CV₁ blue) and second scan (CV₂ orange) and CVs acquired after 10 CVs were taken at 100 mV/s, repeated 6 times in the same solution. Scan rate of all CVs in this figure is 10 mV/s. The inset shows the Ni(OH)₂/NiOOH redox peaks and onset of oxygen evolution. The number of CVs (10-60) refers to the total number of scans acquired at 100 mV/s.

The effect of the addition of Al³⁺ on OER at NiO_xH_y was studied at different concentrations, in several electrolytes and at different catalyst film thicknesses. As a background, the electrochemical behavior and OER of Ni-Bi)_{1mC} in 1 M KBi as a response to potential cycling was studied. Figure 4.1 shows a first scan CV of Ni-Bi)_{1mC} in 1 M KBi at 10 mV/s and after 10 CVs at 100 mV/s, repeated six times. With potential cycling, OER current increased, OER onset shifted negative and the redox peaks shift anodically while overall the cathodic peaks decreased in area and peak current. Since the KBi electrolyte has not been purified, the NiO_xH_y film will acquire Fe from the solution with cycling increasing its OER activity.¹

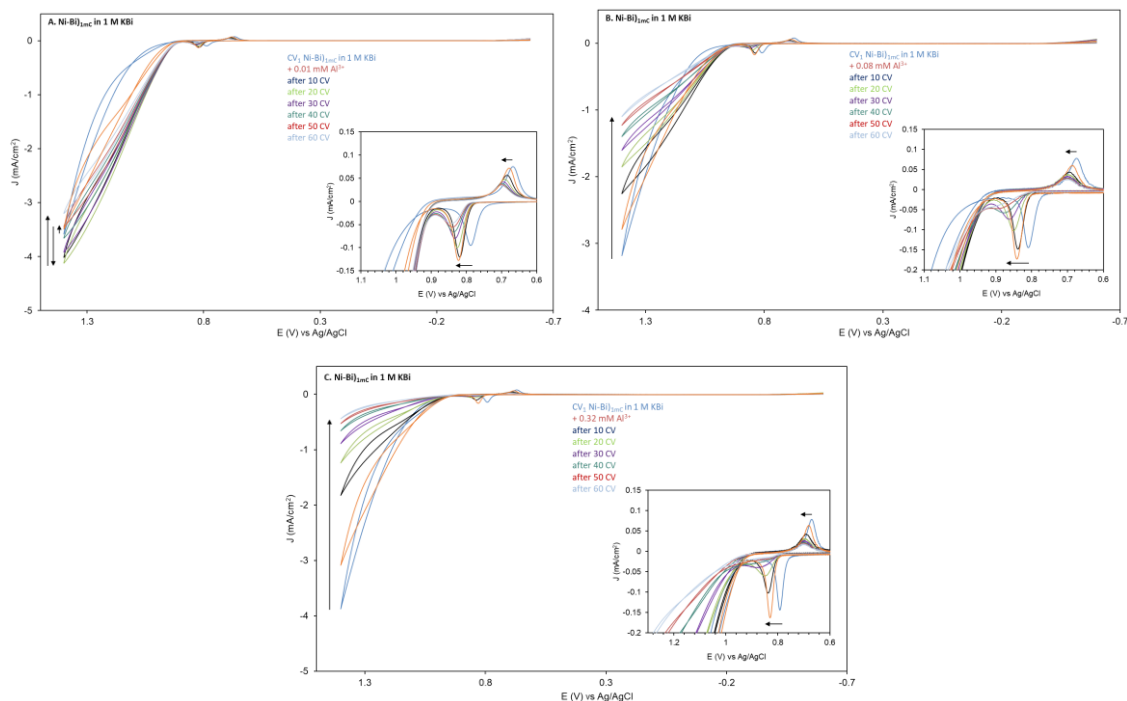


Figure 4.2: Cyclic voltammograms of Ni-Bi)_{1mC} film in 1 M KBi, as a first scan (CV₁ blue), a second scan after 0.01 mM (A), 0.08 mM (B) and 0.32 mM (C) Al³⁺ addition (orange) and CVs acquired after 10 CVs were taken at 100 mV/s, repeated 6 times in the same solution. Scan rate of all CVs in this figure is 10 mV/s. The inset shows the Ni(OH)₂/NiOOH redox peaks and onset of oxygen evolution. The number of CVs (10-60) refers to the total number of scans acquired at 100 mV/s.

Figure 4.2 shows a first scan CV at Ni-Bi)_{1mC} (3.14 ± 1.75 nmol/cm² active Ni content and 2.33 ± 1.08 nm thickness) in 1 M KBi at 10 mV/s before and after the addition of 0.01 mM (A), 0.08 mM (B) and 0.32 mM (C) Al³⁺ to the solution and then after 10 CVs at 100 mV/s, repeated six times. In Figure 4.2.A, after the addition of 0.01 mM Al³⁺, a decrease in OER onset and a very slight decrease in OER currents occurred. With potential cycling, OER currents further increased and onset decreased for the first 20 CVs followed by a decrease in currents for the remaining 40 CVs at high potentials and no change in onset. The Ni(OH)₂/NiOOH redox peaks shifted anodically after the

addition of Al^{3+} and potential cycling with almost no change in anodic peak charge (0.23 to 0.24 mC/cm^2) and in cathodic peak charge (constant at 0.17 mC/cm^2) in the first CV following the addition, and then a decrease with further potential cycling. With greater addition of Al^{3+} , presented in Figures 4.2.B and 4.2.C, an immediate decrease in OER activity was seen with the addition of Al^{3+} and potential cycling. The redox peaks maintained a similar trend whereby they shifted anodically with the addition and cycling, and the cathodic peak charges remained almost the same (0.47 to 0.49 mC/cm^2 and 0.46 to 0.45 mC/cm^2 at 0.08 and 0.32 mM Al^{3+} respectively) while the anodic peak charges increased (0.44 to 0.50 mC/cm^2 and 0.40 to 0.45 mC/cm^2 at 0.08 and 0.32 mM Al^{3+} respectively) with the addition (meaning first CV after addition) but then decreased with further potential cycling. The OER poisoning effect gradually increased with increasing Al^{3+} concentration as seen in Figure 4.2 where a steeper decrease in OER activity and redox peak size (a decrease of 50% and 94% in the cathodic and anodic peak charges, respectively, after 60 CVs) is observed with near deactivation and disappearance of the anodic peak at 0.32 mM Al^{3+} and more than the decrease seen at cycled $\text{Ni-Bi)}_{1\text{mC}}$.

A significant decrease of 92% and 94% in anodic peak charges was seen after the addition of 0.08 and 0.32 mM Al^{3+} to $\text{Ni-Bi)}_{1\text{mC}}$, respectively, and potential cycling in 1 M KBi (accompanied by a decrease in OER currents), compared to a decrease of 30% in anodic peak charge observed when $\text{Ni-Bi)}_{1\text{mC}}$ was cycled after 60 CVs in 1 M KBi without Al . On the other hand, the decrease in cathodic peak charges after the addition of 0.08 and 0.32 mM Al^{3+} to $\text{Ni-Bi)}_{1\text{mC}}$ and cycling (53% and 50% respectively) was more comparable (even less) to that at $\text{Ni-Bi)}_{1\text{mC}}$ alone after cycling (62%). The addition of smaller amount of Al^{3+} (0.01 mM) led to a smaller decrease in

anodic peak charge (by 41%) and cathodic peak charge (by 46%) than the addition of higher Al; thus, with peak charge decreases more comparable to the effect of cycling without Al.

The ratio of anodic to cathodic peak charge between the as-deposited Ni-Bi films and after 0.08 and 0.32 mM Al^{3+} and cycling significantly decreased from 0.93 to 0.16 and 0.88 to 0.10, respectively. The same trend was not observed at Ni-Bi before and after cycling without Al (increase from 1.58 to 2.88). Potential cycling therefore leads to decrease in cathodic peak charges, indicating dissolution, but it does not appear that this is more affected by the presence of Al in solution, or that when the scan is taken to higher potentials the $\text{Ni}(\text{OH})_2$ is redepositing. The presence of Al however significantly decreases the anodic peak charge possibly because of Al co-deposition with Ni in the film at these potentials or Al making the oxidation of Ni harder.

A similar poisoning effect by Al on OER activity was seen in the work of Fayad et al. where 0.16 mM Al^{3+} was added to $\text{Ni-Bi)}_{1\text{mC}}$ and $\text{Ni}_{0.6}\text{Fe}_{0.4}\text{-Bi)}_{1\text{mC}}$, and 0.08 mM Al^{3+} and 0.08 mM Fe^{3+} were added together to $\text{Ni-Bi)}_{1\text{mC}}$.¹ They also reported that the addition of Al^{3+} to $\text{Ni}_{0.6}\text{Fe}_{0.4}\text{-Bi)}_{1\text{mC}}$ in 1 M KBi caused a decrease in OER activity and the addition of Al^{3+} and Fe^{3+} in equal quantities to $\text{Ni-Bi)}_{1\text{mC}}$ in 1 M KBi led to an initial increase followed by subsequent decrease in OER activity with potential cycling.¹ Similar to the latter, when Al^{3+} was added to $\text{NiO}_x\text{H}_y)_{1\text{mC}}$ in 1 M KBi, the OER activity decreased even in the presence of trace Fe in solution. The presence of Al in solution therefore has two effects: 1) it decreases OER currents or prevents traces of Fe in solution from activating the films for OER in KBi, and 2) it affects the electrochemical behavior in that it causes a significant decrease in anodic peak currents, significantly more than affecting the cathodic peaks.

The decrease in cathodic peak can be attributed to dissolution, but this is also similarly observed in KBi in the absence of Al in solution. The inclusion of Al can be affecting the electrochemical activity of Ni(OH)₂ oxidation at its usual oxidation potential, and can be also blocking active surface sites preventing Fe from activating them. Al³⁺ might also be electrostatically interacting with the negatively charged OER rate-limiting intermediates found on the surface of the catalyst forming clusters of hydrated-cation and surface-adsorbed species which are OER inactive. This might be similar to the reported effect of Li⁺ on OER/ORR.¹⁵¹ Thus, Al possibly either affects the reaction barrier energy and reaction kinetics or blocks active sites.¹⁵²

2. Effect of Al Addition in KOH on the Electrochemical Behavior and OER of NiO_xH_y

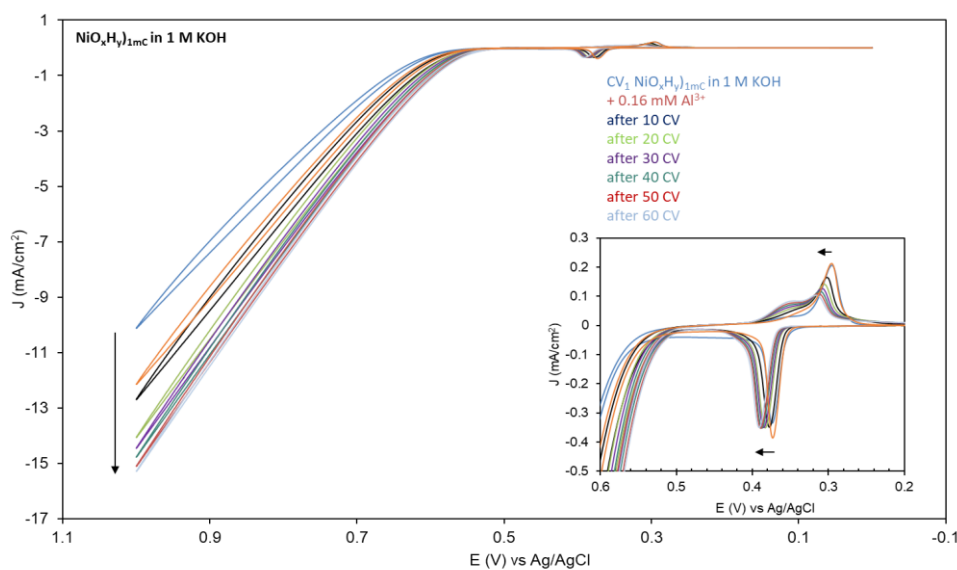


Figure 4.3: Cyclic voltammograms of NiO_xH_y)_{1mC} film in 1 M KOH, as a first scan (CV₁ blue), after the addition of 0.16 mM Al³⁺ (CV₂ orange) and CVs acquired after 10 CVs were taken at 100 mV/s, repeated 6 times in the same solution. Scan rate of all CVs in this figure is 10 mV/s. The inset shows the Ni(OH)₂/NiOOH redox peaks and onset of oxygen evolution. The number of CVs (10-60) refers to the total number of scans acquired at 100 mV/s.

Figure 4.3 shows a first scan CV at $\text{NiO}_x\text{H}_y)_{1\text{mC}}$ in 1 M KOH at 10 mV/s before and after the addition of 0.16 mM Al^{3+} to the solution and then after 10 CVs at 100 mV/s, repeated six times. An increase in OER activity and decrease in OER onset were seen after the addition of Al^{3+} and after potential cycling. This behavior is similar to the effect of potential cycling of $\text{NiO}_x\text{H}_y)_{1\text{mC}}$ in 1 M KOH (Figure 3.7) where the activity increased due to the incorporation of Fe from the unpurified KOH solution. The addition of Al in solution did not decrease the OER activity of the $\text{NiO}_x\text{H}_y)_{1\text{mC}}$ film as it did in 1 M KBi and did not significantly cause an immediate increase in OER activity as the addition of Fe in KOH.

As for the redox peaks, the first scan exhibited a minor shoulder which was more prominent in the cathodic peak similar to what was discussed in Chapter 3. With the addition of Al^{3+} and potential cycling, the cathodic peak split and developed a shoulder along with an anodic shift of both redox peaks as seen in the inset of Figure 4.3. The splitting of the peaks was notable in the presence of Al, and though it also occurs in the presence of Fe in solution, it is more prominent in the presence of Al. The cathodic peak charges decreased by 9% while the anodic peak charges increased by 20% after Al addition and potential cycling unlike the significant decrease seen in 1 M KBi. A comparable decrease in peaks was seen when $\text{NiO}_x\text{H}_y)_{1\text{mC}}$ was cycled in KOH without Al. This indicates that the amount of active Ni did not decrease with the addition of Al^{3+} in 1 M KOH as it did in 1 M KBi nor is Al resulting in lower oxidation of Ni at this peak potential. The presence of Al in KOH does not clearly indicate a competition with Fe for active surface sites, unlike in KBi, as seen with the decrease in OER onset and increase in OER currents. We note that even at this high Al concentration compared to Fe traces ($\leq 0.0005\%$), the OER activity did not decrease

but rather increased; this indicates that sites are being activated with Fe inclusion from traces in KOH, and that Al does not block OER activity in KOH.

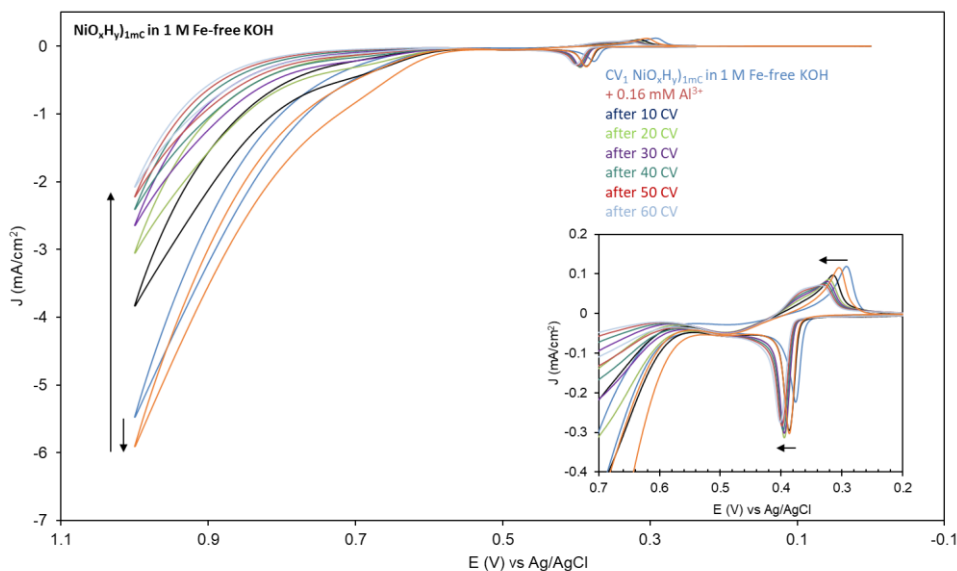


Figure 4.4: Cyclic voltammograms of $\text{NiO}_x\text{H}_y)_{1\text{mC}}$ film in 1 M Fe-free KOH, as a first scan (CV_1 blue), after the addition of 0.16 mM Al^{3+} (CV_2 orange) and CVs acquired after 10 CVs were taken at 100 mV/s, repeated 6 times in the same solution. Scan rate of all CVs in this figure is 10 mV/s. The inset shows the $\text{Ni(OH)}_2/\text{NiOOH}$ redox peaks and onset of oxygen evolution. The number of CVs (10-60) refers to the total number of scans acquired at 100 mV/s.

We also studied the effect of Al on the electrochemical behavior and OER at $\text{NiO}_x\text{H}_y)_{1\text{mC}}$ in the absence of Fe in solution. Figure 4.4 shows a first scan CV at $\text{NiO}_x\text{H}_y)_{1\text{mC}}$ in 1 M Fe-free KOH at 10 mV/s before and after the addition of 0.16 mM Al^{3+} to the solution and then after 10 CVs at 100 mV/s, repeated six times. A slight increase in OER activity is seen after the Al^{3+} addition followed by decrease in activity with potential cycling. Similar to the same experiment in 1 M KOH, the redox peaks

exhibit an anodic shift with the cathodic peak splitting. However, the redox peak charges slightly increased with both the addition of Al^{3+} and potential cycling in 1 M Fe-free KOH. When potential cycling in Fe-free KOH in the absence of Al, the peaks remain generally in the same position, and do not split (Figure 3.3). The splitting of peaks and the anodic shift are therefore a result of incorporation of Al in the NiO_xH_y film. In the absence of Fe in solution, the peak charges did not decrease in 1 M Fe-free KOH after Al addition and potential cycling (0.93 mC/cm^2 and 0.64 mC/cm^2 cathodic and anodic as-deposited, respectively, compared to 1.16 mC/cm^2 and 0.67 mC/cm^2 cathodic and anodic post-addition and cycling, respectively) which indicates that NiO_xH_y is not dissolving.

The difference observed in catalytic and electrochemical behavior between 1 M KBi and 1 M KOH may be because of the difference in solubility of Al^{3+} and the complexes it forms in each solution. It is possible that Al blocks active sites on the catalyst surface when added in solution or that Al competes with Fe for surface-sites in KBi. An increase in OER activity is seen in 1 M KOH with Al^{3+} addition and potential cycling, possibly due to the high solubility of Al^{3+} in solutions of $\text{pH} > 13$ such as 1 M KOH, forming aluminate ions, $\text{Al}(\text{OH})_4^-$,¹⁵³⁻¹⁵⁵ which does not occur in 1 M KBi of $\text{pH} \sim 9.2$. Perhaps, Al in the form of aluminate in solution has no poisoning effect on OER and thus Fe traces in solution enhance OER activity without any competition or blocking. However, Al^{3+} also fully dissolves and forms aluminate in 1 M Fe-free KOH, also of $\text{pH} > 13$, but due to the absence of Fe traces in this solution, the film deactivates and OER activity decreases similar to Figure 3.3 where $(\text{NiO}_x\text{H}_y)_{1\text{mC}}$ is cycled in 1 M Fe-free KOH. There is still evidence of Al inclusion in these films from the anodic shift in their peaks and peak splitting with Al in Fe-free KOH. These different Al complexes are

possibly occupying different sites or are competing with OER active sites. Further studies on the effect of Al in solution on NiO_xH_y film conductivity and impedance are needed.

Peak splitting is observed in the $\text{Ni}(\text{OH})_2/\text{NiOOH}$ redox peaks of $\text{NiO}_x\text{H}_y)_{1\text{mC}}$ after the addition of Al^{3+} and potential cycling in 1 M Fe-free KOH and in 1 M KOH, which was not observed for $\text{NiO}_x\text{H}_y)_{1\text{mC}}$ after potential cycling in 1 M Fe-free KOH with no metal ion addition. This must indicate Al deposition in the catalyst film and its effect on the electrochemical behavior of $\text{Ni}(\text{OH})_2$. The significant effect of Al in solution on catalyst film oxidation seen with the disappearance of redox peaks with Al addition in KBi was not similarly observed in KOH. Thus, Al in KBi leads to a less stable Ni-Bi catalyst.

Interestingly, the peak splitting behavior exhibited with Al^{3+} is similar to when 0.16 mM Fe^{3+} is added to $\text{NiO}_x\text{H}_y)_{1\text{mC}}$ in 1 M KOH and when 0.16 mM Ce^{3+} or 0.16 mM La^{3+} to $\text{NiO}_x\text{H}_y)_{1\text{mC}}$ in 1 M KOH. Moreover, a slight cathodic shoulder can be seen with the potential cycling of $\text{NiO}_x\text{H}_y)_{1\text{mC}}$ in 1 M unpurified KOH (Figure 3.7) but not in 1 M Fe-free KOH where the peaks remain unchanged (Figure 3.3). This leads to the hypothesis that this peak splitting behavior is mainly attributed to electronic interactions between Ni and the guest metals when included in the NiO_xH_y structure, post-deposition, resulting in the presence of two different Ni sites with different interactions on the surface and in the bulk, even as minute impurities in the electrolyte.

DFT calculations supported by experimental work have suggested that dissolved Al^{3+} acts as a substitutional dopant at Ni sites and that the insertion of Al leads to significant electronic changes rather than structural ones by increasing the conductivity of the system.¹⁴⁴ They also showed that Al sites neighboring Fe sites have no significant

effect on OER activity and energetics and thus surface site doping with Al does not enhance OER.¹⁴⁴ Moreover, in this case, Al does not negatively impact the activity but possibly changes the ratio of metal ions of γ -Fe/NiOOH lattice, increasing the number of M^{3+} ions, and the catalyst morphology.¹⁴⁴

B. Effect of the Co-deposition of Al on Ni-oxo/hydroxide Films

1. Effect of Al Co-deposition in Thin $Ni_{0.6}Al_{0.4}Bi$ on the Electrochemical Behavior and OER in 1 M KBi

Films	Charge _{as-dep} (mC/cm ²)	Charge _{anod} (mC/cm ²)	nmol _{Ni} /cm ² _{as-dep}	nmol _{Ni} /cm ² _{anod}
Ni-Bi _{1mC} (<i>N</i> = 3)	0.47 ± 0.09	0.56 ± 0.12	4.09 ± 0.75	4.87 ± 1.04
Ni_{0.6}Al_{0.4}-Bi _{1mC} (<i>N</i> = 3)	0.35 ± 0.03	0.40 ± 0.08	3.06 ± 0.24	3.44 ± 0.67
Films	Thickness _{as-dep} (nm)	Thickness _{anod} (nm)	Monolayers _{eq} [Ni(OH) ₂] _{as-dep}	Monolayers _{eq} [Ni(OH) ₂] _{anod}
Ni-Bi _{1mC} (<i>N</i> = 3)	3.03 ± 0.56	3.61 ± 0.77	3.79 ± 0.69	4.51 ± 0.97
Ni_{0.6}Al_{0.4}-Bi _{1mC} (<i>N</i> = 3)	2.27 ± 0.18	2.55 ± 0.50	2.84 ± 0.23	3.19 ± 0.62

Table 4.1: Average cathodic peak charge, number of moles of active Ni, thickness and monolayer equivalence of Ni(OH)₂ for as-deposited and anodized Ni-Bi)_{1mC} and Ni_{0.6}Al_{0.4}-Bi)_{1mC} films measured in 1 M KBi.

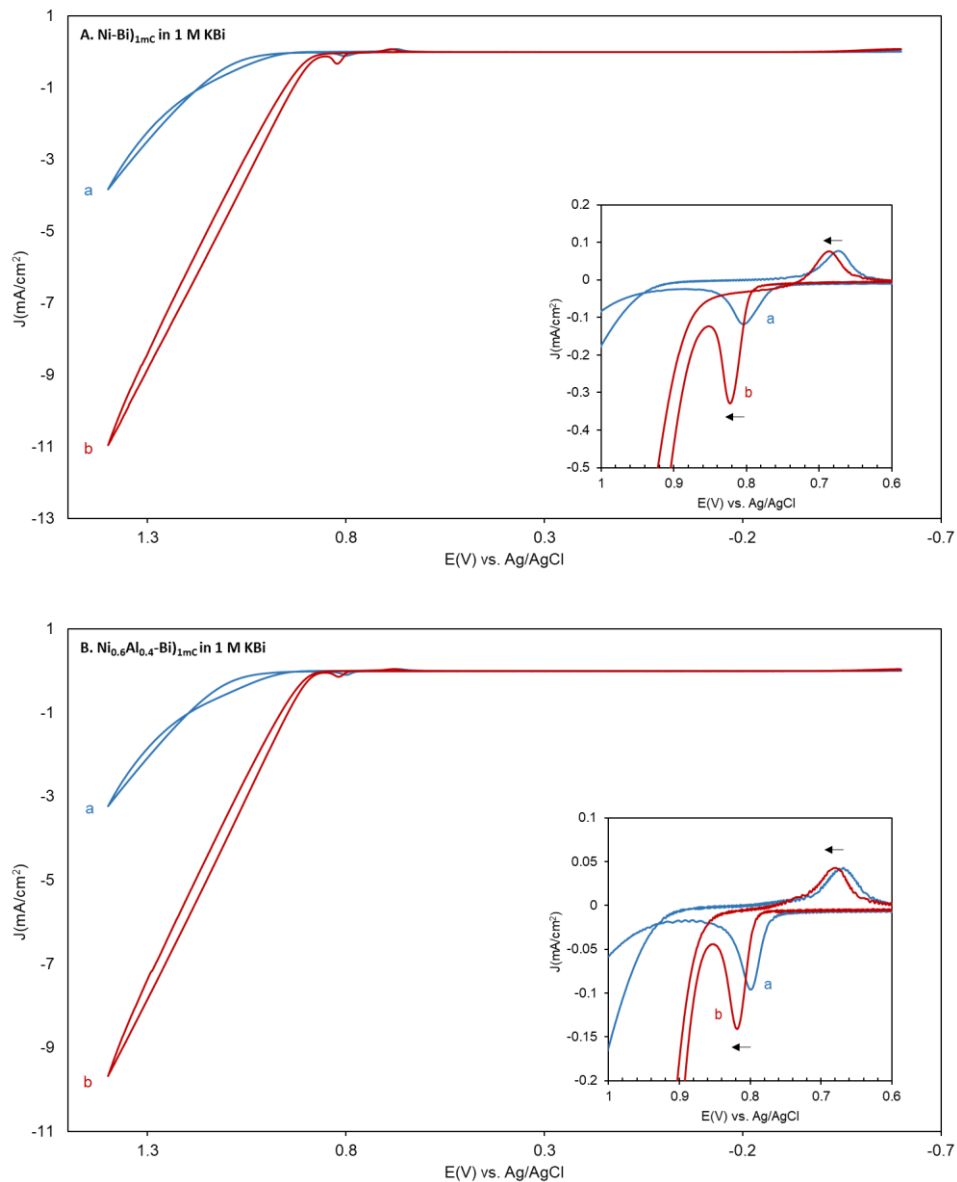


Figure 4.5: Cyclic voltammograms in 1 M KBi at $\text{Ni-Bi)}_{1\text{mC}}$ (A) and $\text{Ni}_{0.6}\text{Al}_{0.4}\text{-Bi)}_{1\text{mC}}$ (B) as a first scan (a, blue) and after anodic conditioning in the same solution (b, red). The insets show the corresponding redox peaks and onset of oxygen evolution for the three scans shown. Scan rate is 10 mV/s.

As Al addition in solution was observed to lower OER activity and affect the oxidation of Ni-Bi in KBi, we investigated the effects of co-deposited Al in $\text{Ni}_{0.6}\text{Al}_{0.4}\text{-Bi)}$ on the electrochemical behavior and OER in 1 M KBi. The films were deposited as

previously indicated by anodic electrodeposition on FTO at 0.953 V vs. Ag/AgCl from 0.4 mM Ni(NO₃)₂ or mixed Ni(NO₃)₂:Al(NO₃)₃ of 6:4 ratio in 0.1 M KBi of pH ~ 9.20 at different thicknesses set by fixing the deposition charge at 1, 100 or 400 mC/cm². Figure 4.5 shows CVs of Ni-Bi)_{1mC} (A) and Ni_{0.6}Al_{0.4}-Bi)_{1mC} (B) at 10 mV/s in 1 M KBi: as-deposited (a) and after anodic conditioning (b). A sharp anodic peak can be seen at 0.80 ± 0.00 V and 0.81 vs. ± 0.00 V Ag/AgCl (N = 3) for Ni_{0.6}Al_{0.4}-Bi)_{1mC} (2.27 ± 0.18 nm thick and 2.84 ± 0.23 Ni(OH)₂ monolayers) and Ni-Bi)_{1mC} (3.03 ± 0.56 nm thick and 3.79 ± 0.70 Ni(OH)₂ monolayers), respectively, representing the oxidation of Ni(OH)₂ to NiOOH, and a cathodic peak at 0.67 ± 0.00 V and 0.67 ± 0.01 V vs. Ag/AgCl, respectively, representing the corresponding reduction reaction. The average cathodic peak charges equaled 0.35 ± 0.03 mC (N = 3) and 0.47 ± 0.09 mC (N = 3) for as-deposited Ni_{0.6}Al_{0.4}-Bi)_{1mC} and Ni-Bi)_{1mC}, respectively, which increased to 0.40 ± 0.08 mC and 0.56 ± 0.12 mC, respectively, after anodic conditioning. The average Ni content was 75 ± 15 % in as-deposited Ni_{0.6}Al_{0.4}-Bi)_{1mC} relative to Ni-Bi)_{1mC}.

Films	As-Deposited				Anodized			
	E _{p,a} (mV)	E _{p,c} (mV)	ΔE _p (mV)	E _{1/2} (mV)	E _{p,a} (mV)	E _{p,c} (mV)	ΔE _p (mV)	E _{1/2} (mV)
<i>Ni-Bi</i>) _{1mC} (N = 3)	805 ± 4	672 ± 5	133 ± 2	739 ± 5	822 ± 6	686 ± 3	136 ± 4	754 ± 4
<i>Ni_{0.6}Al_{0.4}-Bi</i> (N = 3)	796 ± 4	672 ± 4	124 ± 6	734 ± 2	822 ± 4	689 ± 9	133 ± 7	755 ± 6
<i>Ni_{0.4}Al_{0.6}-Bi</i> (N = 4)	788 ± 13	686 ± 7	102 ± 14	737 ± 8	822 ± 9	703 ± 7	119 ± 13	762 ± 5

Table 4.2: Average anodic and cathodic peak positions, peak separation and half-wave potentials for as-deposited and anodized Ni-Bi)_{1mC}, Ni_{0.6}Al_{0.4}-Bi)_{1mC} and Ni_{0.4}Al_{0.6}-Bi)_{1mC} films measured in 1 M KBi. E_p and E_{1/2} values are reported vs. Ag/AgCl.

The anodic peak of Ni-Bi)_{1mC} and Ni_{0.6}Al_{0.4}-Bi)_{1mC} anodically shifted by 18 mV and 19 mV after anodic conditioning, respectively, while the cathodic peak anodically shifted by 13 mV and 11 mV after anodic conditioning, respectively. The average peak shifts showed a similar trend with variation. On average, a similar trend was observed: the anodic peak shifted anodically by 17 ± 7 mV and 26 ± 5 mV (N = 3) after anodic conditioning for Ni-Bi)_{1mC} and Ni_{0.6}Al_{0.4}-Bi)_{1mC}, respectively, while the cathodic peak shifted anodically by 14 ± 6 mV and 17 ± 10 mV after anodic conditioning, respectively.

The half-wave potentials, $E_{1/2}$, for Ni-Bi)_{1mC} and Ni_{0.6}Al_{0.4}-Bi)_{1mC} (N =3 for both) were 0.739 ± 0.005 V and 0.734 ± 0.002 V, respectively, showing no significant shift due to the co-deposition of Al. A similar observation was reported earlier with Fe co-deposition in Ni-Bi although studies in the literature showed that Fe and Al inclusion caused an anodic shift for cathodically deposited (Ni-Fe-Bi) and KOH-activated oxide (Ni-Al-O) films.^{1, 144} The peak separation, ΔE_p , for as-deposited Ni-Bi)_{1mC}, Ni_{0.6}Al_{0.4}-Bi)_{1mC} and Ni_{0.4}Al_{0.6}-Bi)_{1mC} were 133 ± 2 mV, 124 ± 6 mV and 102 ± 14 mV, respectively, which, after anodic conditioning, was 136 ± 4 mV, 133 ± 7 mV and 119 ± 13 mV, respectively. As-deposited films at 6:4 Ni:Al ratio exhibited slightly better redox peak reversibility on average compared to the Ni films, while films at 4:6 Ni:Al ratio exhibited increased reversibility possibly due to the higher Al content. The latter was analogous to the effect of Fe inclusion in Ni-Bi where peak separation decreased from 134 mV to 112 mV and 106 mV at 6:4 and 4:6 Ni:Fe ratios, respectively.¹

Corrigan reported that Fe inclusion in NiO_x decreased peak separation from 101 mV to 80 mV⁹² and 150 mV to 125 mV.⁹⁷ After anodic conditioning, a slight increase in ΔE_p was seen for the Ni_xAl_{1-x}-Bi)_{1mC} films indicating a decrease in reversibility similar

to the decrease in reversibility post-anodization seen in previously studied Ni-Bi)_{1mC} films and Ni_xFe_{1-x}-Bi)_{1mC} films.¹ A greater effect of anodization on decreasing reversibility was observed for Al-containing films, possibly due to Al leaching and dissolution out of the catalyst film. On the other hand, as-deposited Ni-Bi)_{1mC} exhibited a significant increase in ΔE_p from 122 mV to 148 mV with the addition of 0.32 mM of Al³⁺ and from 148 mV to 180 mV after 30 CVs, and an increase in ΔE_p from 135 mV to 156 mV with the addition of 0.08 mM of Al³⁺ and from 156 mV to 178 mV after 50 CVs (ΔE_p was not calculated after 40-60 CVs and after 60 CVs with the 0.32 and 0.08 mM Al³⁺ addition, respectively, due to anodic peak dissolution). A similar increase in ΔE_p was not observed when Ni-Bi)_{1mC} was potentially cycled in KBi without Al (increase from 127 to 141 mV). This in turn possibly indicates Al inclusion and incorporation into the Ni-Bi film differently depending on the deposition method.

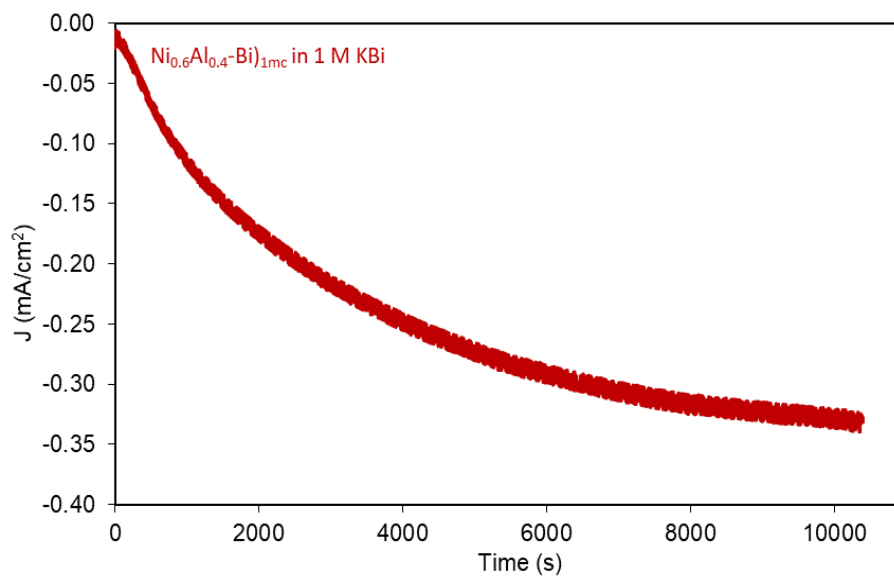


Figure 4.6: Anodization plot (i-t plot) of an ultra-thin Ni_{0.6}Al_{0.4}-Bi)_{1mC} film biased at 0.903 V vs. Ag/AgCl in 1 M KBi.

The OER activity of both $(\text{Ni-Bi})_{1\text{mC}}$ and $(\text{Ni}_{0.6}\text{Al}_{0.4}\text{-Bi})_{1\text{mC}}$ was comparable, as deposited and after anodic conditioning as seen in CVs and Tafel plots, leading to the conclusion that anodization was the reason for catalyst activation and not the co-deposition of Al. Moreover, the anodization i-t curves, such as in Figure 4.6, showed a similar trend to the $\text{Ni}_{0.6}\text{Fe}_{0.4}\text{O}_x\text{H}_y$ catalyst films in 1 M KOH (Figure 3.14) with an increase in OER current due to the incorporation of Fe from the unpurified KBi solution. Thus, the OER catalytic activity is attributed to the deposition of Fe traces from solution in both films as reported.⁹⁶

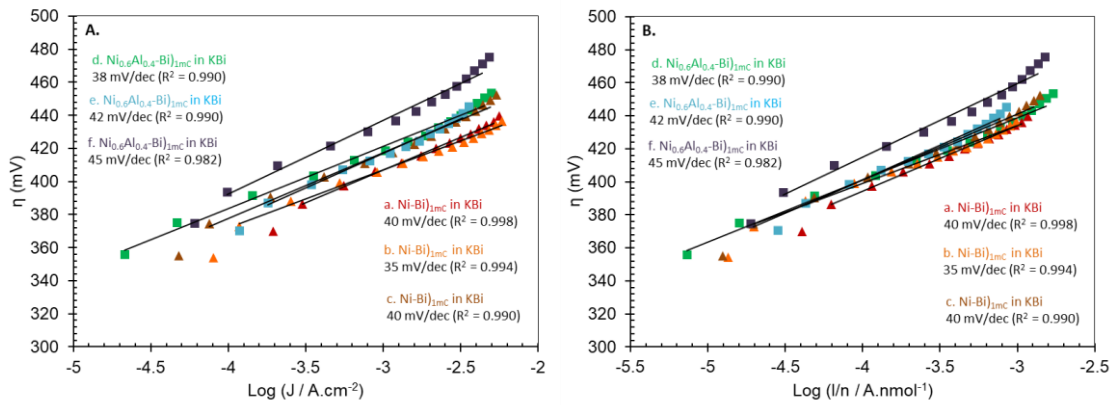


Figure 4.7: Tafel plots (A) and normalized Tafel plots (B) for $(\text{Ni-Bi})_{1\text{mC}}$ (red, orange and brown; ▲) and $(\text{Ni}_{0.6}\text{Al}_{0.4}\text{-Bi})_{1\text{mC}}$ (blue, green and purple; ■) anodized in 1 M KBi and measured in the same solution with the corresponding slopes for the best fit linear plot.

Figure 4.7 shows Tafel plots (A) and normalized Tafel plots (B) of the $(\text{Ni-Bi})_{1\text{mC}}$ and $(\text{Ni}_{0.6}\text{Al}_{0.4}\text{-Bi})_{1\text{mC}}$ films. The Tafel slopes of the $(\text{Ni-Bi})_{1\text{mC}}$ and $(\text{Ni}_{0.6}\text{Al}_{0.4}\text{-Bi})_{1\text{mC}}$ from Figure 4.5 after anodization were 40 mV/dec and 38 mV/dec, respectively, which was comparable to the slopes measured in the literature for Ni-Bi.^{1, 7, 93, 95} Fayad et al. reported Tafel slopes between 30 and 40 mV/dec for $(\text{Ni-Bi})_{1\text{mC}}$.¹ Corrigan observed

slope of 40 mV/dec for NiO_x thin films,⁹² Nocera et al. reported slopes of 30 mV/dec for thin Ni-Bi⁷ and Boettcher et al. reported slopes of 46 mV/dec for slightly thicker Ni-Bi)_{10mC}.⁹⁵ Little variation was seen in the Tafel slopes of other Ni_{0.6}Al_{0.4}-Bi)_{1mC} and Ni-Bi)_{1mC} films (N = 3 for each) with an average of 42 ± 3 mV/dec and 38 ± 3 mV/dec, respectively. Normalized Tafel plots show a proportionality of OER activity to Ni centers over a range of overpotential (380 – 450 mV) in 1 M KBi. It can be concluded that Fe traces in solution are the reason behind the enhancement in OER activity in both films and that Al incorporation in Ni_{0.6}Al_{0.4}-Bi)_{1mC} and any possible leaching at these levels is not causing a significant poisoning of OER activity or change in OER mechanism to affect Tafel slopes nor does its presence destabilize the films.

Films	Tafel Slope (mV/dec)	TOF_{SS-asdep} (s⁻¹) (@η ~ 400 mV)	TOF_{SS-anod} (s⁻¹) (@η ~ 400 mV)
Ni-Bi)_{1mC} (N = 3)	38 ± 3	0.317 ± 0.023 (η = 400 ± 3 mV)	0.269 ± 0.036 (η = 400 ± 3 mV)
Ni_{0.6}Al_{0.4}-Bi)_{1mC} (N = 3)	42 ± 3	0.259 ± 0.085 (η = 404 ± 6 mV)	0.231 ± 0.075 (η = 404 ± 6 mV)

Table 4.3: Average Tafel slope, apparent TOF for O₂ per second per Ni center calculated at an overpotential of ~ 400 mV from steady-state current measurements under stirring for as-deposited and anodized Ni-Bi)_{1mC} and Ni_{0.6}Al_{0.4}-Bi)_{1mC} films measured in 1 M KBi.

Steady-state turnover frequency (TOF) for OER per Ni center were calculated, at an overpotential of ~400 mV, to further evaluate the effect of codeposited Ni_{0.6}Al_{0.4}-

$\text{Bi})_{1\text{mC}}$ in comparison to $\text{Ni-Bi})_{1\text{mC}}$ using the equation: $\text{TOF} = \frac{J \times A}{4 \times F \times n_{\text{Ni}}}$, where J is the steady-state current density obtained from the Tafel plots of each catalyst film (A/cm^2), A is the geometric electrode area (cm^2), F is Faraday's constant and n is the number of moles of active Ni (mol). The average steady-state $\text{TOF}_{400\text{mV}}$ for as-deposited $\text{Ni}_{0.6}\text{Al}_{0.4}\text{-Bi})_{1\text{mC}}$ (N = 3) equaled to $0.26 \pm 0.08 \text{ s}^{-1}$ and for as-deposited $\text{Ni-Bi})_{1\text{mC}}$ (N = 3) equaled to $0.32 \pm 0.02 \text{ s}^{-1}$. While the average steady-state $\text{TOF}_{400\text{mV}}$ for anodized $\text{Ni}_{0.6}\text{Al}_{0.4}\text{-Bi})_{1\text{mC}}$ (N = 3) equaled to $0.23 \pm 0.07 \text{ s}^{-1}$ and for anodized $\text{Ni-Bi})_{1\text{mC}}$ (N = 3) equaled to $0.27 \pm 0.04 \text{ s}^{-1}$. The ratios of the average steady-state $\text{TOF}_{400\text{mV}}$ for as-deposited $\text{Ni}_{0.6}\text{Al}_{0.4}\text{-Bi})_{1\text{mC}}$ to $\text{Ni-Bi})_{1\text{mC}}$ and anodized $\text{Ni}_{0.6}\text{Al}_{0.4}\text{-Bi})_{1\text{mC}}$ to $\text{Ni-Bi})_{1\text{mC}}$ equaled to 0.82 and 0.86, respectively. This indicates that the presence of co-deposited Al is lowering the TOF for as-deposited and anodized films. The poisoning effect of codeposited Al in $\text{Ni}_{0.6}\text{Al}_{0.4}\text{-Bi})_{1\text{mC}}$ is thus seen in both as-deposited and anodized films through the TOF values at an overpotential of $\sim 400 \text{ mV}$. Therefore, even though Al co-deposition did not affect the Tafel slope and therefore the mechanism of OER, its presence decreased the OER activity per Ni site, either by possibly blocking sites or affecting morphology and thus access to sites.

2. Effect of Al Co-deposition in Thin $Ni_{0.6}Al_{0.4}O_xH_y$)_{1mC} on the Electrochemical Behavior and OER in 1 M Fe-free KOH

Films	Charge _{as-dep} (mC/cm ²)	Charge _{anod} (mC/cm ²)	Charge _{tafel} (mC/cm ²)	nmol _{Ni} /cm ² _{as-dep}	nmol _{Ni} /cm ² _{anod}	nmol _{Ni} /cm ² _{tafel}
NiO_xH_y) _{1mC} (N = 5)	0.68 ± 0.24	0.67 ± 0.24	0.68 ± 0.13	5.85 ± 2.04	5.76 ± 2.06	5.91 ± 1.11
$Ni_{0.6}Al_{0.4}O_xH_y$) _{1mC} (N = 8)	0.62 ± 0.28	0.59 ± 0.26	0.54 ± 0.23	5.33 ± 2.43	5.07 ± 2.22	4.68 ± 2.03

Films	Thickness _{as-dep} (nm)	Thickness _{anod} (nm)	Thickness _{tafel} (nm)	Monolayers _{eq} [Ni(OH) ₂] _{as-dep}	Monolayers _{eq} [Ni(OH) ₂] _{anod}	Monolayers _{eq} [Ni(OH) ₂] _{tafel}
NiO_xH_y) _{1mC} (N = 5)	4.34 ± 1.51	4.27 ± 1.53	4.39 ± 0.83	5.42 ± 1.89	5.34 ± 1.91	5.48 ± 1.03
$Ni_{0.6}Al_{0.4}O_xH_y$) _{1mC} (N = 8)	3.95 ± 1.80	3.76 ± 1.65	3.47 ± 1.51	4.94 ± 2.25	4.70 ± 2.06	4.34 ± 1.89

Table 4.4: Average cathodic peak charge, number of moles of active Ni, thickness and monolayer equivalence of Ni(OH)₂ for as-deposited, anodized and after Tafel

NiO_xH_y)_{1mC} and $Ni_{0.6}Al_{0.4}O_xH_y$)_{1mC} films measured in 1 M Fe-free KOH.

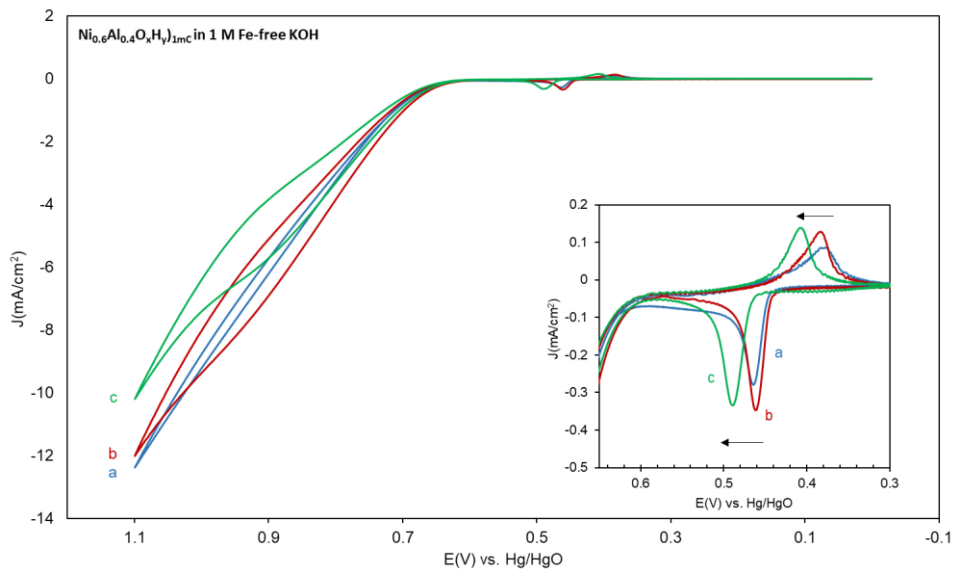


Figure 4.8: Cyclic voltammograms in 1 M Fe-free KOH at $\text{Ni}_{0.6}\text{Al}_{0.4}\text{O}_x\text{H}_y)_{1\text{mC}}$ as a first scan (a, blue), after anodic conditioning in the same solution (b, red) and after Tafel measurements (c, green). The insets show the corresponding redox peaks and onset of oxygen evolution for the three scans shown. Scan rate is 10 mV/s.

We further investigated the effects of co-deposited Al with NiO_xH_y on the electrochemical behavior and OER in 1 M Fe-free KOH, in the absence of Fe traces in solution, as-deposited, after anodization and Tafel measurements. Figure 4.8 shows CVs of $\text{Ni}_{0.6}\text{Al}_{0.4}\text{O}_x\text{H}_y)_{1\text{mC}}$ at 10 mV/s in 1 M Fe-free KOH: as-deposited (a), after anodic conditioning (b) and after Tafel measurements (c). A sharp anodic peak can be seen at 0.46 ± 0.01 V vs. Hg/HgO and a cathodic peak at 0.38 ± 0.01 V vs. Hg/HgO. The average cathodic peak charges, that are used to calculate the amount of electrochemically active Ni, equaled 0.62 ± 0.28 mC/cm² (N = 8) for as-deposited $\text{Ni}_{0.6}\text{Al}_{0.4}\text{O}_x\text{H}_y)_{1\text{mC}}$ (3.95 ± 1.80 nm thick and 4.94 ± 2.25 Ni(OH)₂ monolayers) which decreases to 0.54 ± 0.23 mC/cm² after Tafel measurements. The average Ni content was 91 ± 52 % in as-deposited $\text{Ni}_{0.6}\text{Al}_{0.4}\text{O}_x\text{H}_y)_{1\text{mC}}$ relative to $\text{NiO}_x\text{H}_y)_{1\text{mC}}$, while we note that

this was not observed in measurements in KBi of similarly prepared films. Al co-deposition thus causes a large variation in the Ni content of these co-deposited films. This variation was not observed with Fe co-deposition in $\text{Ni}_{0.6}\text{Fe}_{0.6}\text{O}_x\text{H}_y$ catalyst films, which led to a Ni content of $73 \pm 29\%$ in 1 M Fe-free KOH.

As seen in Figure 4.8, CVs of as-deposited $\text{Ni}_{0.6}\text{Al}_{0.4}\text{O}_x\text{H}_y)_{1\text{mC}}$ in 1 M Fe-free KOH showed small cathodic and anodic shoulders before the major $\text{Ni}(\text{OH})_2/\text{NiOOH}$ redox peaks. After anodization, the shoulders did not appear and the OER onset remained unchanged with a slight decrease in OER current at high potential. Similar to the $\text{NiO}_x\text{H}_y)_{1\text{mC}}$ and $\text{Ni}_{0.6}\text{Fe}_{0.4}\text{O}_x\text{H}_y)_{1\text{mC}}$ films in the same solution, an anodic wave at $\sim 0.85 - 0.95$ V vs. Hg/HgO accompanied by hysteresis can be seen - a characteristic behavior in Fe-free solution. After Tafel measurements, CVs showed a decrease in OER current with no change in OER onset and the same anodic wave at $\sim 0.85 - 0.95$ V vs. Hg/HgO with greater hysteresis.

Films	As-Deposited				Anodized			
	$E_{p,a}$	$E_{p,c}$	ΔE_p	$E_{1/2}$	$E_{p,a}$	$E_{p,c}$	ΔE_p	$E_{1/2}$
	(mV)	(mV)	(mV)	(mV)	(mV)	(mV)	(mV)	(mV)
$NiO_xH_y)_{1mC}$ ($N = 5$)	457 ± 5	382 ± 5	76 ± 3	420 ± 5	453 ± 7	382 ± 3	71 ± 6	418 ± 4
$Ni_{0.6}Al_{0.4}O_xH_y)_{1mC}$ ($N = 8$)	466 ± 16	386 ± 16	80 ± 5	426 ± 16	466 ± 11	393 ± 16	73 ± 6	429 ± 13
Films	Tafel							
	$E_{p,a}$	$E_{p,c}$	ΔE_p	$E_{1/2}$				
	(mV)	(mV)	(mV)	(mV)				
$NiO_xH_y)_{1mC}$ ($N = 5$)	460 ± 18	387 ± 10	73 ± 7	424 ± 14				
$Ni_{0.6}Al_{0.4}O_xH_y)_{1mC}$ ($N = 8$)	474 ± 16	400 ± 19	74 ± 9	437 ± 17				

Table 4.5: Average anodic and cathodic peak positions, peak separation and half-wave potentials for as-deposited, anodized and after Tafel $NiO_xH_y)_{1mC}$ and $Ni_{0.6}Al_{0.4}O_xH_y)_{1mC}$ films measured in 1 M Fe-free KOH. E_p and $E_{1/2}$ values are reported vs. Hg/HgO.

The anodic peak of $Ni_{0.6}Al_{0.4}O_xH_y)_{1mC}$ cathodically shifted by 3 mV with anodic conditioning but anodically shifted by 25 mV after Tafel measurements while the cathodic peak anodically shifted by 6 mV with anodic conditioning and by 30 mV after Tafel measurements. The average peak shifts showed a similar trend with variation shown in Table 4.5. On average ($N = 8$), the anodic peak did not shift after anodic conditioning but shifted anodically by 8 mV after Tafel measurements while the cathodic peak shifted anodically by 7 mV after anodic conditioning and by 14 mV with Tafel measurements. In Fe-free KOH, the inclusion of Al did not cause a smaller ΔE_p as observed in KBi, but on average $E_{1/2}$ was slightly more anodic at $Ni_{0.6}Al_{0.4}O_xH_y)_{1mC}$ than of $NiO_xH_y)_{1mC}$ films.

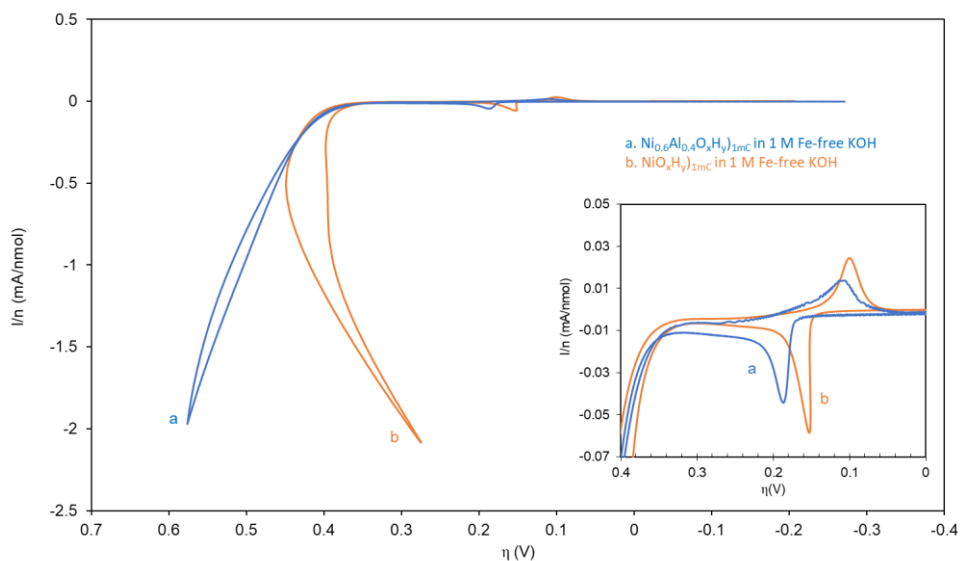


Figure 4.9: Normalized cyclic voltammograms, I/n (mA/nmol) vs. η (V), at $\text{Ni}_{0.6}\text{Al}_{0.4}\text{O}_x\text{H}_y)_{1\text{mC}}$ (a, blue) and $\text{NiO}_x\text{H}_y)_{1\text{mC}}$ (b, orange) films in 1 M Fe-free KOH as a first scan. The inset shows the $\text{Ni}(\text{OH})_2/\text{NiOOH}$ redox peaks and onset of oxygen evolution. Scan rate is 10 mV/s.

Baker et al. reported that the co-deposition of Al leads to more anodically shifted redox peaks when comparing Ni-Al-O to Ni-O in iron-free KOH with a peak difference of ~ 50 mV.¹⁴⁴ We observe on average significantly smaller anodic shifts between $\text{NiO}_x\text{H}_y)_{1\text{mC}}$ and $\text{Ni}_{0.6}\text{Al}_{0.4}\text{O}_x\text{H}_y)_{1\text{mC}}$ in Fe-free KOH. They also reported a slight enhancement in OER activity in Ni-Al-O over Ni-O in iron-free KOH.¹⁴⁴ This improvement was not seen in this work for as-deposited films in the CVs or the normalized CVs, I/n versus η , (Figure 4.9) in 1 M Fe-free KOH. Figure 4.9 shows similar OER onset and similar I/n at low overpotential for both of $\text{NiO}_x\text{H}_y)_{1\text{mC}}$ and $\text{Ni}_{0.6}\text{Al}_{0.4}\text{O}_x\text{H}_y)_{1\text{mC}}$. The differences in electrochemical behavior and OER activity of co-deposited $\text{Ni}(\text{Al})\text{O}_x\text{H}_y$ between our work and the literature might be due to the different deposition methods used to prepare the catalyst film where Baker et al. used atomic

layer deposition to form Ni-Al-O which was preconditioned in 0.1 M Reagent grade KOH (which contains traces of Fe) to form the hydroxide species.¹⁴⁴

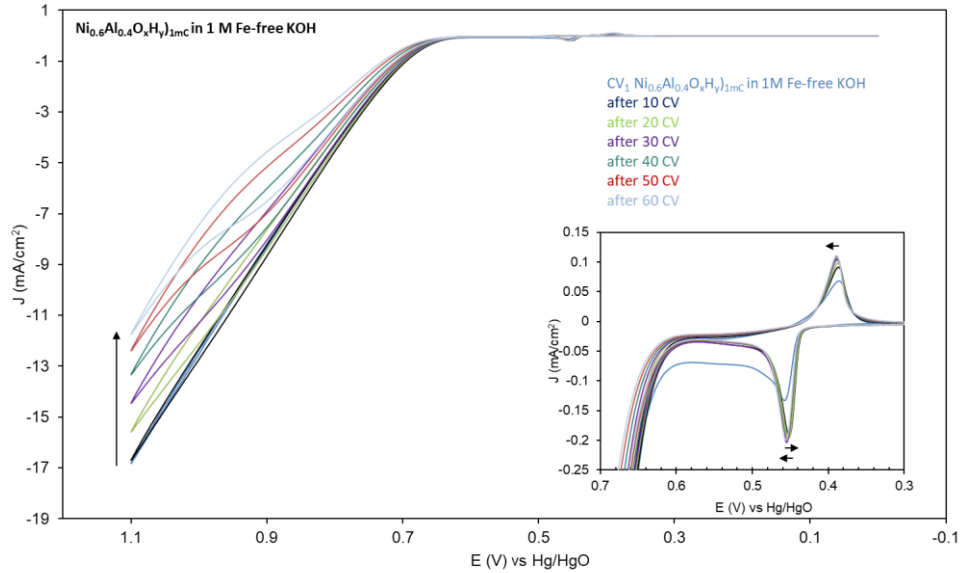


Figure 4.10: Cyclic voltammograms of $\text{Ni}_{0.6}\text{Al}_{0.4}\text{O}_x\text{H}_y$)_{1mC} film in 1 M Fe-free KOH, as a first scan (CV₁ blue) and CVs acquired after 10 CVs were taken at 100 mV/s, repeated 6 times in the same solution. Scan rate of all CVs in this figure is 10 mV/s. The inset shows the Ni(OH)₂/NiOOH redox peaks and onset of oxygen evolution. The number of CVs (10-60) refers to the total number of scans acquired at 100 mV/s.

We studied the electrochemical behavior of $\text{Ni}_{0.6}\text{Al}_{0.4}\text{O}_x\text{H}_y$)_{1mC} when subjected to potential scanning in 1 M Fe-free KOH. Figure 4.10 shows a first scan CV at $\text{Ni}_{0.6}\text{Al}_{0.4}\text{O}_x\text{H}_y$)_{1mC} in 1 M Fe-free KOH at 10 mV/s and then after 10 CVs at 100 mV/s, repeated six times. The as-deposited film did not experience any hysteresis but after potential cycling an anodic wave at ~ 0.9 V appeared similar to the effect of anodic conditioning (low anodic bias) in 1 M Fe-free KOH. The OER currents decreased

(while the OER onset slightly shifted anodically) with potential cycling similar to Figure 3.3 where $\text{NiO}_x\text{H}_y)_{1\text{mC}}$ was cycled in 1 M Fe-free KOH.

The major $\text{Ni}(\text{OH})_2/\text{NiOOH}$ redox peaks charges increased from 0.39 to 0.44 mC/cm^2 for the cathodic peak and from 0.36 to 0.49 mC/cm^2 for the anodic peak initially after the first 10 CVs followed by a gradual minor increase with more potential cycling. The anodic peak slightly shifted cathodically from 0.458 to 0.452 V with the first 10 CVs followed by a slight and gradual anodic shift with every 10 CVs to reach 0.456 V after 60 CVs while a very slight anodic shift from 0.386 to 0.389 V was observed for the cathodic peak after 60 CVs.

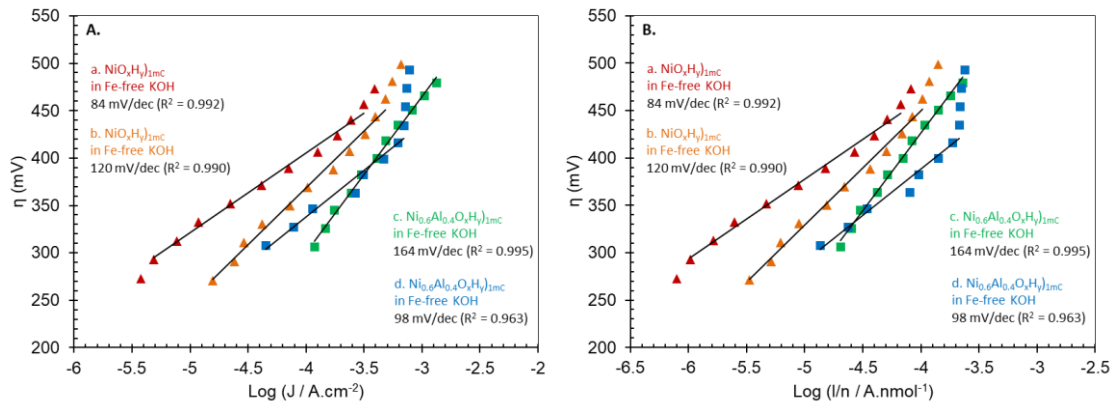


Figure 4.11: Tafel plots (A), overpotential η (mV) versus $\log(J / \text{A}/\text{cm}^2)$, and normalized Tafel plots (B), overpotential η (mV) versus $\log(I/n / \text{A}/\text{nmol})$, for two $\text{NiO}_x\text{H}_y)_{1\text{mC}}$ (red, orange; \blacktriangle) and two $\text{Ni}_{0.6}\text{Al}_{0.4}\text{O}_x\text{H}_y)_{1\text{mC}}$ (green, blue; \blacksquare) films anodized in 1 M Fe-free KOH and measured in the same solution with the corresponding slopes for the best fit linear plot.

Figure 4.11 shows Tafel plots (overpotential η vs. $\log J$) (A) and normalized Tafel plots (overpotential η vs. $\log I/n$) of $\text{NiO}_x\text{H}_y)_{1\text{mC}}$ and $\text{Ni}_{0.6}\text{Al}_{0.4}\text{O}_x\text{H}_y)_{1\text{mC}}$ films

including those from Figure 3.1, 3.2 and 4.8 in 1 M Fe-free KOH. The Tafel slope of the $\text{Ni}_{0.6}\text{Al}_{0.4}\text{O}_x\text{H}_y$)_{1mC} after anodization and measurements in 1 M Fe-free KOH was 164 mV/dec. Tafel slopes of other $\text{Ni}_{0.6}\text{Al}_{0.4}\text{O}_x\text{H}_y$)_{1mC} films were similarly high in value ranging from 81 to 108 mV/dec. The high Tafel slope is similar to those reported in the literature⁹⁴ and Chapter 3, such as 84 and 104 mV/dec respectively, for NiO_xH_y)_{1mC} and $\text{Ni}_{0.6}\text{Fe}_{0.4}\text{O}_x\text{H}_y$)_{1mC} in the same solution. Tafel slopes of NiO_xH_y)_{1mC} (N = 2) and $\text{Ni}_{0.6}\text{Al}_{0.4}\text{O}_x\text{H}_y$)_{1mC} (N = 8) averaged at 102 ± 25 mV/dec and 111 ± 29 mV/dec, respectively.

Despite a higher Tafel slope, TOF calculated at 400 mV overpotential (within Tafel region) show (Table 4.6) a higher OER activity per Ni for $\text{Ni}_{0.6}\text{Al}_{0.4}\text{O}_x\text{H}_y$)_{1mC} in comparison to NiO_xH_y)_{1mC} in Fe-free KOH. A wide variation in TOF_{400mV} of $\text{Ni}_{0.6}\text{Al}_{0.4}\text{O}_x\text{H}_y$)_{1mC} was calculated. Two of these measurements (N = 2 in Table 4.6) were conducted vs. Hg/HgO reference electrodes which were filled with and stored in 1 M Fe-free (purified) NaOH. The cell setup was also thoroughly rinsed with Fe-free solution. Even then, while suspecting the effect of Fe coupled with Al, the TOF of the two $\text{Ni}_{0.6}\text{Al}_{0.4}\text{O}_x\text{H}_y$)_{1mC} films investigated was still higher than that of NiO_xH_y)_{1mC}, but further experiments are needed to study NiO_xH_y)_{1mC} under similar conditions. Initial results showed a possible effect of Al in the absence of Fe on increasing TOF even though Tafel slopes were on average not lower at NiO_xH_y)_{1mC} (no OER improvement seen at Tafel slopes).

Films	Tafel Slope (mV/dec)	TOF _{SS-asdep} (s ⁻¹) (@η ~ 400 mV)	TOF _{SS-anod} (s ⁻¹) (@η ~ 400 mV)
NiO_xH_y)_{1mC} (N = 2)	102 ± 25	0.093 ± 0.035 (η = 407 ± 0 mV)	0.091 ± 0.033 (η = 407 ± 0 mV)
Ni_{0.6}Al_{0.4}O_xH_y)_{1mC} (N = 2)	131 ± 47	0.209 ± 0.097 (η = 400 ± 0 mV)	0.212 ± 0.104 (η = 400 ± 0 mV)
Ni_{0.6}Al_{0.4}O_xH_y)_{1mC} (N = 8)	111 ± 29	0.765 ± 0.862 (η = 398 ± 5 mV)	0.749 ± 0.794 (η = 398 ± 5 mV)

Table 4.6: Average Tafel slope, apparent TOF for O₂ per second per Ni center calculated at an overpotential of ~ 400 mV from steady-state current measurements under stirring for as-deposited and anodized NiO_xH_y)_{1mC} and Ni_{0.6}Al_{0.4}O_xH_y)_{1mC} films measured in 1 M Fe-free KOH.

3. Effect of Al Co-deposition in Thin $Ni_{0.6}Al_{0.4}O_xH_y)_{1mC}$ on the Electrochemical Behavior and OER in 1 M Unpurified KOH:

Films	Charge _{as-dep} (mC/cm ²)	Charge _{anod} (mC/cm ²)	Charge _{tafel} (mC/cm ²)	nmol _{Ni} /cm ² _{as-dep}	nmol _{Ni} /cm ² _{anod}	nmol _{Ni} /cm ² _{tafel}
$NiO_xH_y)_{1mC}$ (<i>N</i> = 8)	0.85 ± 0.19	0.72 ± 0.20	0.67 ± 0.24	7.31 ± 1.69	6.25 ± 1.75	5.83 ± 2.09
$Ni_{0.6}Al_{0.4}O_xH_y)_{1mC}$ (<i>N</i> = 4)	0.39 ± 0.06	0.32 ± 0.10	0.33 ± 0.11	3.36 ± 0.51	2.73 ± 0.88	2.85 ± 0.93

Films	Thickness _{as-dep} (nm)	Thickness _{anod} (nm)	Thickness _{tafel} (nm)	Monolayers _{Seq} [Ni(OH) ₂] _{as-dep}	Monolayers _{Seq} [Ni(OH) ₂] _{anod}	Monolayers _{Seq} [Ni(OH) ₂] _{tafel}
$NiO_xH_y)_{1mC}$ (<i>N</i> = 8)	5.42 ± 1.25	4.63 ± 1.30	4.32 ± 1.55	6.77 ± 1.56	5.79 ± 1.63	5.40 ± 1.94
$Ni_{0.6}Al_{0.4}O_xH_y)_{1mC}$ (<i>N</i> = 4)	2.49 ± 0.38	2.02 ± 0.65	2.21 ± 0.69	3.12 ± 0.48	2.53 ± 0.82	2.64 ± 0.87

Table 4.7: Average cathodic peak charge, number of moles of active Ni, thickness and monolayer equivalence of Ni(OH)₂ for as-deposited and anodized $NiO_xH_y)_{1mC}$ and $Ni_{0.6}Al_{0.4}O_xH_y)_{1mC}$ films measured in 1 M KOH.

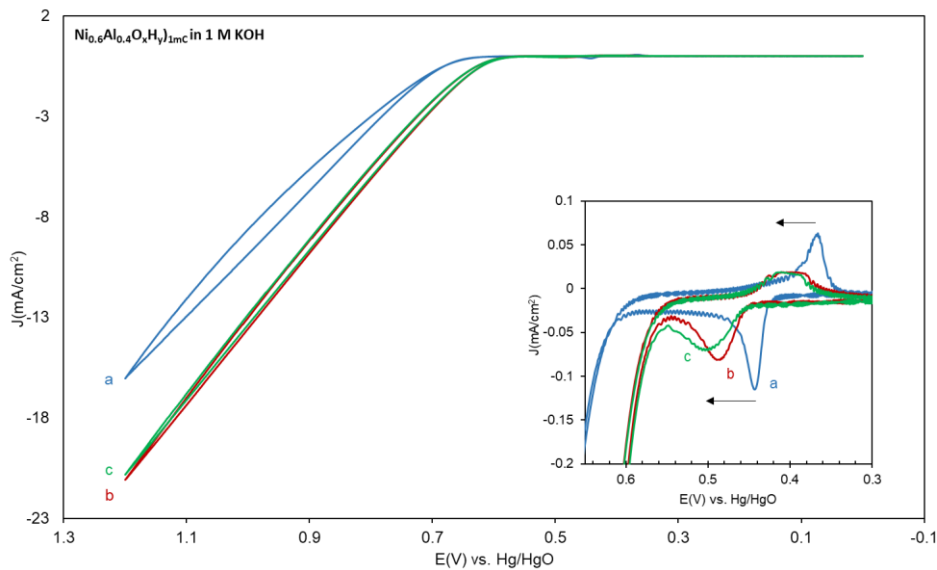


Figure 4.12: Cyclic voltammograms in 1 M KOH at $\text{Ni}_{0.6}\text{Al}_{0.4}\text{O}_x\text{H}_y)_{1\text{mC}}$ as a first scan (a, blue), after anodic conditioning in the same solution (b, red) and after Tafel measurements (c, green). The insets show the corresponding redox peaks and onset of oxygen evolution for the three scans shown. Scan rate is 10 mV/s.

We investigated the effects of co-deposited Al with NiO_xH_y on the electrochemical behavior and OER in 1 M unpurified KOH (in the presence of Fe traces in solution) as-deposited, after anodization and Tafel measurements. Figure 4.12 shows CVs of $\text{Ni}_{0.6}\text{Al}_{0.4}\text{O}_x\text{H}_y)_{1\text{mC}}$ at 10 mV/s in 1 M KOH: as-deposited (a), after anodic conditioning (b) and after Tafel measurements (c). A sharp anodic peak can be seen at 0.45 ± 0.00 V vs. Hg/HgO ($N = 4$) and a sharp cathodic peak at 0.37 ± 0.01 V vs. Hg/HgO. The average peak charges equaled 0.39 ± 0.06 mC/cm² ($N = 4$) for as-deposited $\text{Ni}_{0.6}\text{Al}_{0.4}\text{O}_x\text{H}_y)_{1\text{mC}}$ (2.49 ± 0.38 nm thick and 3.12 ± 0.48 Ni(OH)₂ monolayers) which decreases to 0.32 ± 0.10 mC/cm² after anodic conditioning and stayed almost constant at 0.33 ± 0.11 mC/cm² after Tafel measurements. The average Ni content was 63 ± 15 % in as-deposited $\text{Ni}_{0.6}\text{Al}_{0.4}\text{O}_x\text{H}_y)_{1\text{mC}}$ ($N = 4$) relative to $\text{NiO}_x\text{H}_y)_{1\text{mC}}$

($N = 2$; using measurements done vs. Hg/HgO of $\text{nmol}_{\text{Ni}} = 5.37 \pm 0.95 \text{ nmol/cm}^2$) and did not show the same variation as the measurements in Fe-free KOH.

CVs of as-deposited $\text{Ni}_{0.6}\text{Al}_{0.4}\text{O}_x\text{H}_y$)_{1mc} in 1 M KOH showed similar shoulders with the anodic and cathodic peaks, where the cathodic shoulder was more prominent than the anodic shoulder, before the major $\text{Ni}(\text{OH})_2/\text{NiOOH}$ redox peaks. After anodization, unlike the films in 1 M Fe-free KOH, the OER onset decreased and currents increased. The anodization i-t curves (Figure 4.13) showed a similar trend to $\text{Ni}_{0.6}\text{Fe}_{0.4}\text{O}_x\text{H}_y$)_{1mc} (Figure 3.14) and NiO_xH_y)_{1mc} in 1 M KOH with an increase in OER current with anodic bias, in contrast to the decrease in OER current seen in 1 M Fe-free KOH for all catalysts studied. After Tafel measurements, no significant change to the OER onset and currents occurred and thus films maintained high OER activity.

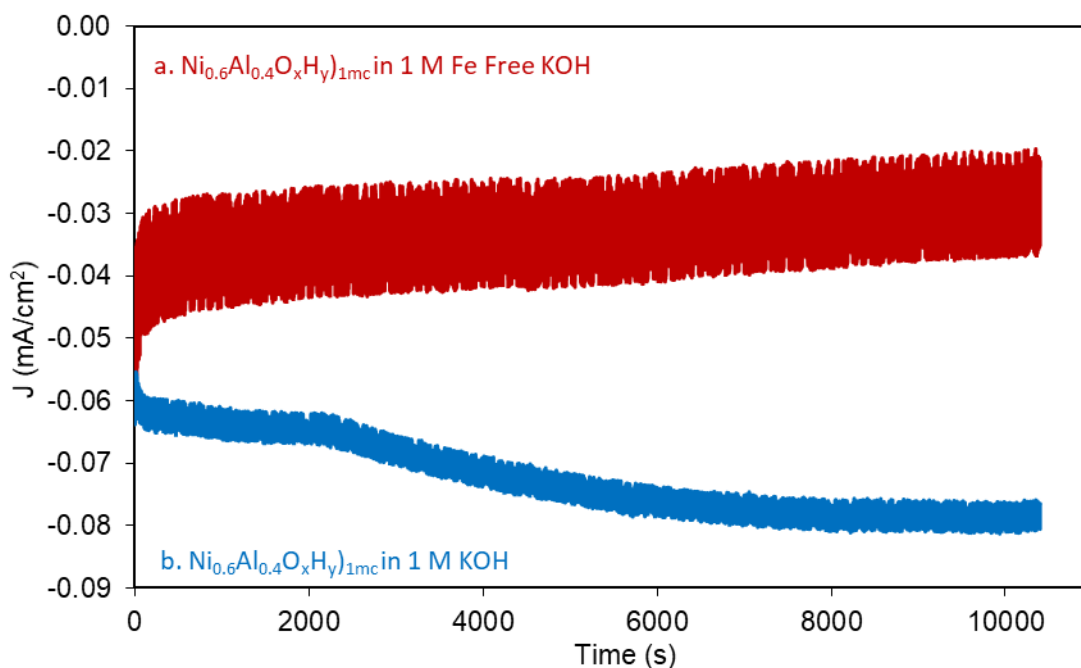


Figure 4.13: Anodization plots (i-t plots) of ultra-thin $\text{Ni}_{0.6}\text{Al}_{0.4}\text{O}_x\text{H}_y$)_{1mc} films biased at 0.58 V vs. Hg/HgO in 1 M Fe-free KOH (a, red traces) or unpurified 1 M KOH (b, blue traces) as indicated.

Films	As-Deposited				Anodized			
	$E_{p,a}$	$E_{p,c}$	ΔE_p	$E_{1/2}$	$E_{p,a}$	$E_{p,c}$	ΔE_p	$E_{1/2}$
	(mV)	(mV)	(mV)	(mV)	(mV)	(mV)	(mV)	(mV)
$NiO_xH_y)_{1mC}$ ($N = 8$)	454 ± 8	376 ± 8	79 ± 3	414 ± 9	460 ± 8	381 ± 7	79 ± 5	422 ± 8
$Ni_{0.6}Al_{0.4}O_xH_y)_{1mC}$ ($N = 4$)	447 ± 5	372 ± 7	75 ± 3	410 ± 6	468 ± 23	390 ± 18	79 ± 8	429 ± 20
Films	Tafel							
	$E_{p,a}$	$E_{p,c}$	ΔE_p	$E_{1/2}$				
	(mV)	(mV)	(mV)	(mV)				
$NiO_xH_y)_{1mC}$ ($N = 8$)	477 ± 17	395 ± 16	82 ± 5	436 ± 16				
$Ni_{0.6}Al_{0.4}O_xH_y)_{1mC}$ ($N = 4$)	486 ± 29	400 ± 16	86 ± 13	443 ± 22				

Table 4.8: Average anodic and cathodic peak positions, peak separation and half-wave potentials for as-deposited, anodized and after Tafel $NiO_xH_y)_{1mC}$ and $Ni_{0.6}Al_{0.4}O_xH_y)_{1mC}$ films measured in 1 M KOH. E_p and $E_{1/2}$ values are reported vs. Hg/HgO.

In contrast to the films in 1 M Fe-free KOH, cathodic peak splitting occurred leading to a wider peak after anodization and Tafel measurements while the anodic peak widened after anodization and Tafel measurements. No anodic wave or hysteresis were seen after conditioning and after Tafel with the reverse scan almost tracing the forward scan. The anodic peak of $Ni_{0.6}Al_{0.4}O_xH_y)_{1mC}$ anodically shifted by 42 mV and 57 mV after anodic conditioning and Tafel measurements, respectively, while the cathodic peak anodically shifted by 44 mV and 45 mV after anodic conditioning and Tafel measurements, respectively, with these shifts attributed to Fe going in the bulk of the film. The average peak shifts for different films showed a similar trend with variation (Table 4.8). While $E_{1/2}$ was on average more cathodic for $Ni_{0.6}Al_{0.4}O_xH_y)_{1mC}$, a slight

anodic shift was observed after anodization and Tafel, and ΔE_p was similar only with slightly more reversibility on average for as-deposited $\text{Ni}_{0.6}\text{Al}_{0.4}\text{O}_x\text{H}_y$)_{1mC} films.

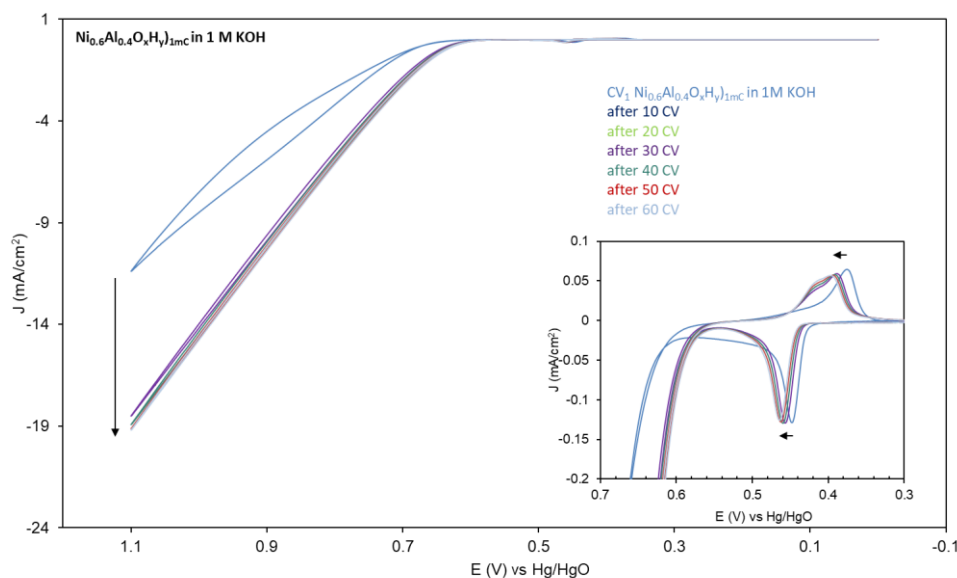


Figure 4.14: Cyclic voltammograms of $\text{Ni}_{0.6}\text{Al}_{0.4}\text{O}_x\text{H}_y$)_{1mC} film in 1 M KOH, as a first scan (CV_1 blue) and CVs acquired after 10 CVs were taken at 100 mV/s, repeated 6 times in the same solution. Scan rate of all CVs in this figure is 10 mV/s. The inset shows the $\text{Ni}(\text{OH})_2/\text{NiOOH}$ redox peaks and onset of oxygen evolution. The number of CVs (10-60) refers to the total number of scans acquired at 100 mV/s.

We also studied the effect of multiple potential cycling on $\text{Ni}_{0.6}\text{Al}_{0.4}\text{O}_x\text{H}_y$)_{1mC} in 1 M KOH. Figure 4.14 shows a first scan CV at $\text{Ni}_{0.6}\text{Al}_{0.4}\text{O}_x\text{H}_y$)_{1mC} in 1 M KOH at 10 mV/s and then after 10 CVs at 100 mV/s, repeated six times. The OER onset decreased and currents increased with potential cycling (after the first 10 CVs then remained the same) similar to Figure 3.7 where NiO_xH_y)_{1mC} was cycled in 1 M KOH. The major $\text{Ni}(\text{OH})_2/\text{NiOOH}$ redox peaks showed almost no change in charges after potential cycling; however, the cathodic peak gradually widened and split. An anodic shift of the

redox peaks was observed with cycling. The general behavior is thus similar to what was observed with anodic bias, but different in terms of the splitting of the peaks and anodic shift from the behavior of $\text{Ni}_{0.6}\text{Al}_{0.4}\text{O}_x\text{H}_y)_{1\text{mC}}$ in Fe-free KOH.

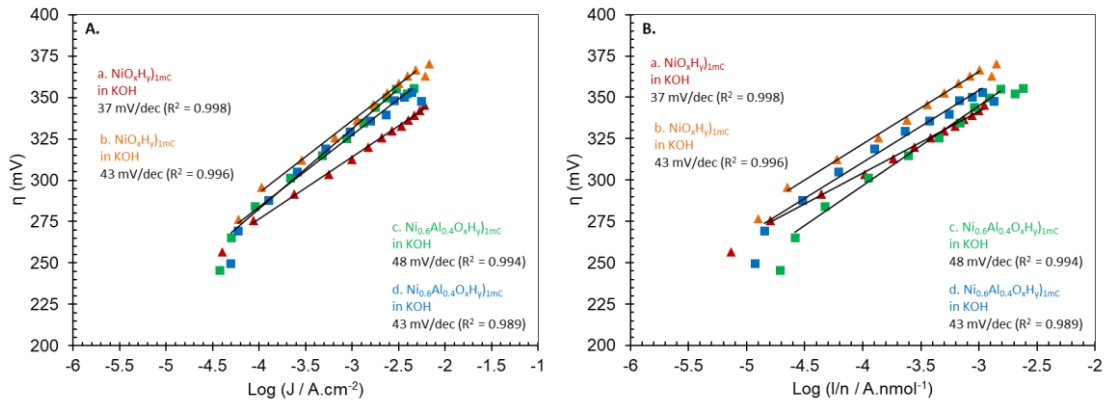


Figure 4.15: Tafel plots (A), overpotential η (mV) versus $\log(J / \text{A}\cdot\text{cm}^{-2})$, and normalized Tafel plots (B), overpotential η (mV) versus $\log(I/n / \text{A}\cdot\text{nmol}^{-1})$, for $\text{NiO}_x\text{H}_y)_{1\text{mC}}$ (red, orange; \blacktriangle) and $\text{Ni}_{0.6}\text{Al}_{0.4}\text{O}_x\text{H}_y)_{1\text{mC}}$ (green, blue; \blacksquare) anodized in 1 M KOH and measured in the same solution with the corresponding slopes for the best fit linear plot.

Figure 4.15 shows Tafel plots (A) and normalized Tafel plots (B) of $\text{NiO}_x\text{H}_y)_{1\text{mC}}$ and $\text{Ni}_{0.6}\text{Al}_{0.4}\text{O}_x\text{H}_y)_{1\text{mC}}$ films in 1 M KOH including those from Figure 3.5, 3.6 and 4.12. The Tafel slope of the $\text{Ni}_{0.6}\text{Al}_{0.4}\text{O}_x\text{H}_y)_{1\text{mC}}$ after anodization and measurements in 1 M KOH was 48 mV/dec and thus in the 40 mV/dec range as seen in Chapter 3 for $\text{NiO}_x\text{H}_y)_{1\text{mC}}$ and $\text{Ni}_{0.6}\text{Fe}_{0.4}\text{O}_x\text{H}_y)_{1\text{mC}}$ (37 and 45 mV/dec respectively) and in the literature in Fe-containing solutions such as KBi and unpurified KOH.^{1, 7, 92-93, 95, 144} Little variation was seen in the Tafel slopes of other $\text{Ni}_{0.6}\text{Al}_{0.4}\text{O}_x\text{H}_y)_{1\text{mC}}$ films with an average ($N=2$) of 46 ± 3 mV/dec in 1 M KOH. Tafel and normalized Tafel plots showed similar

OER activity at both $\text{NiO}_x\text{H}_y)_{1\text{mC}}$ and $\text{Ni}_{0.6}\text{Al}_{0.4}\text{O}_x\text{H}_y)_{1\text{mC}}$ in KOH. Normalized Tafel plots show a proportionality of OER activity to Ni centers over a range of overpotential in 1 M KOH. TOF calculated at ~ 300 mV overpotential (within Tafel region) show (Table 4.9) a higher OER activity per Ni for $\text{Ni}_{0.6}\text{Al}_{0.4}\text{O}_x\text{H}_y)_{1\text{mC}}$ in comparison to $\text{NiO}_x\text{H}_y)_{1\text{mC}}$ in KOH.

Films	Tafel Slope (mV/dec)	TOF _{SS-asdep} (s ⁻¹) (@ $\eta \sim 300$ mV)	TOF _{SS-anod} (s ⁻¹) (@ $\eta \sim 300$ mV)
$\text{NiO}_x\text{H}_y)_{1\text{mC}}$ (N = 3)	43 \pm 5	0.143 \pm 0.081 ($\eta = 299 \pm 2$ mV)	0.168 \pm 0.097 ($\eta = 299 \pm 2$ mV)
$\text{Ni}_{0.6}\text{Al}_{0.4}\text{O}_x\text{H}_y)_{1\text{mC}}$ (N = 2)	45 \pm 3	0.194 \pm 0.026 ($\eta = 303 \pm 3$ mV)	0.228 \pm 0.087 ($\eta = 303 \pm 3$ mV)

Table 4.9: Average Tafel slope, apparent TOF for O₂ per second per Ni center calculated at an overpotential of ~ 300 mV from steady-state current measurements under stirring for as-deposited and anodized $\text{NiO}_x\text{H}_y)_{1\text{mC}}$ and $\text{Ni}_{0.6}\text{Al}_{0.4}\text{O}_x\text{H}_y)_{1\text{mC}}$ films measured in 1 M KOH.

The amount of Ni in as-deposited $\text{Ni}_{0.6}\text{Al}_{0.4}\text{O}_x\text{H}_y)_{1\text{mC}}$ (N = 8) in 1 M Fe-free KOH was 5.33 ± 2.43 nmol/cm² and decreased to 4.68 ± 2.03 nmol/cm² after Tafel measurements, thus recording a 12.3 ± 7.7 % average decrease post-Tafel. Similarly, the amount of Ni in as-deposited $\text{Ni}_{0.6}\text{Al}_{0.4}\text{O}_x\text{H}_y)_{1\text{mC}}$ (N = 4) in 1 M KOH was 3.36 ± 0.51 nmol/cm² which decreased to 2.73 ± 0.88 nmol/cm² after anodic conditioning and slightly increased to 2.85 ± 0.94 nmol/cm² after Tafel measurements, thus recording a

15.2 ± 5.5 % average decrease post-Tafel. Thus, anodic bias and potential cycling do not cause significant dissolution of the co-deposited catalyst.

Baker et al. reported that Ni-Al-OOH was more active Ni-OOH in both Fe-containing KOH (leading to the formation of Ni-Al-Fe-OOH and Ni-Fe-OOH) and Fe-free KOH.¹⁴⁴ However, co-deposition of Al into NiO_xH_y films showed no significant effect on the OER activity of NiO_xH_y in Fe-containing KOH in our study unlike previously reported studies^{103, 144-145} but showed slight enhancement in Fe-free solution as seen in the Tafel plots. This leads to the possibility that the presence of Fe in solution leads to comparable OER activity between Ni_{0.6}Al_{0.4}O_xH_y)_{1mC} and NiO_xH_y)_{1mC} while in the absence of Fe from solution, higher OER activity was seen with Al co-deposition in NiO_xH_y)_{1mC}.

4. Thicker Films in 1 M Fe-free KOH and 1 M KOH

The effect of catalyst film thickness on OER activity and electrochemistry in Fe-free and unpurified KOH was also studied for thicker Ni_{0.6}Al_{0.4}-Bi deposited at 100 mC, termed Ni_{0.6}Al_{0.4}O_xH_y)_{100mC}. Film deposition takes up to 30 min in unpurified 0.1 M KBi which contains traces of Fe allowing the catalyst to possibly deposit Fe from the solution as well.

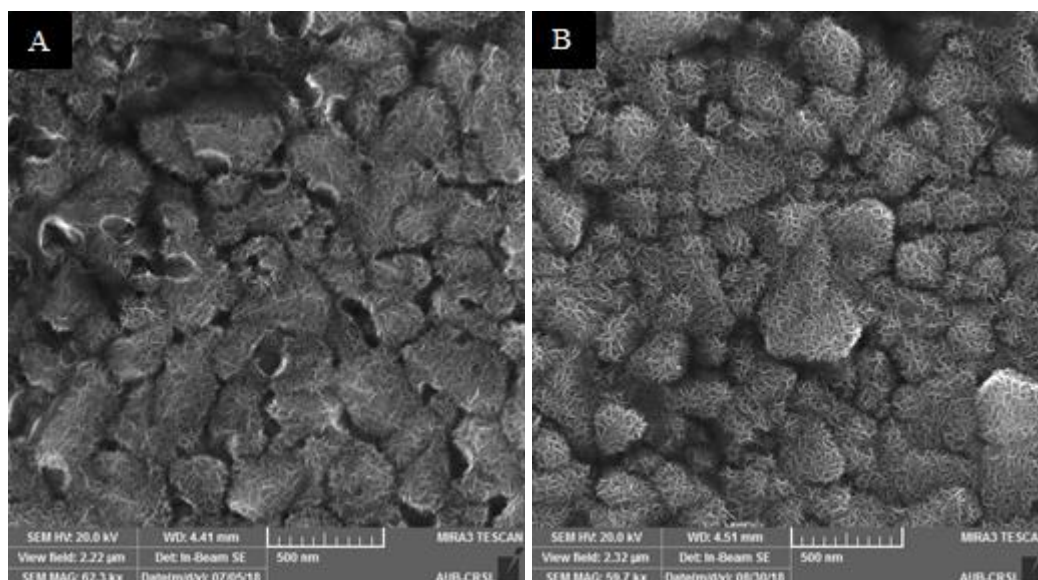


Figure 4.16: SEM images of $\text{Ni}_{0.6}\text{Al}_{0.4}\text{O}_x\text{H}_y)_{400\text{mC}}$ deposited by passing a charge of 400 mC/cm^2 on FTO: as-deposited (A) and after anodic conditioning in 1 M KOH (B).

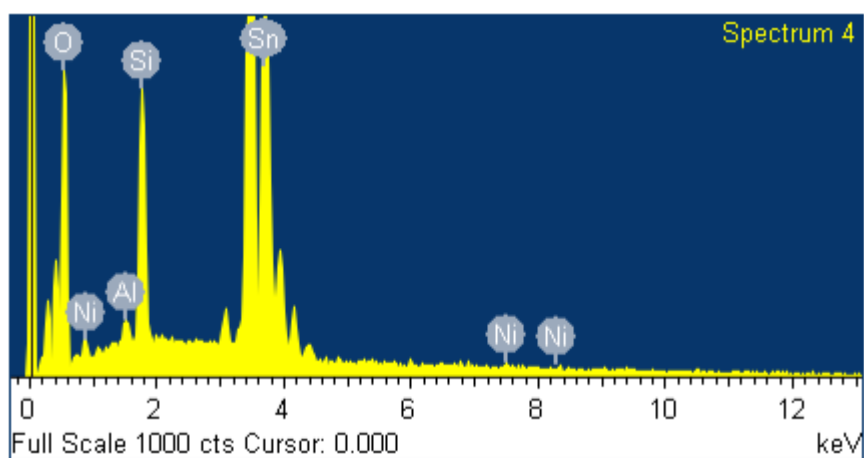


Figure 4.17: EDX spectrum of as-deposited $\text{Ni}_{0.6}\text{Al}_{0.4}\text{O}_x\text{H}_y)_{400\text{mC}}$ showing both Ni and Al peaks.

SEM images of thicker as-deposited $\text{Ni}_{0.6}\text{Al}_{0.4}\text{O}_x\text{H}_y)_{400\text{mC}}$ and KOH-anodized $\text{Ni}_{0.6}\text{Al}_{0.4}\text{O}_x\text{H}_y)_{400\text{mC}}$ demonstrate the nanoflake-like structure of the catalyst. The morphology of the film became flakier after anodization. Baker et al. reported that

morphology is linked to the nature of active sites in the catalyst and that morphological changes occur with Al-doping.¹⁴⁴ However, at this SEM resolution, similar structures are seen in the SEM images of $\text{Ni}_{0.6}\text{Al}_{0.4}\text{O}_x\text{H}_y$, $\text{Ni}_{0.6}\text{Fe}_{0.4}\text{O}_x\text{H}_y$ and NiO_xH_y films. EDX spectrum shows Ni peaks at ~ 0.85 , 7.50 and 8.30 keV and an Al peak at ~ 1.50 keV and thus assuring their presence in the film during anodic co-deposition.

Films	Charge _{as-dep} (mC/cm ²)	Charge _{anod} (mC/cm ²)	Charge _{tafel} (mC/cm ²)	nmol _{Ni} /cm ² _{as-dep}	nmol _{Ni} /cm ² _{anod}	nmol _{Ni} /cm ² _{tafel}
NiO_xH_y _{100mC} (<i>N</i> = 4)	8.10 ± 2.72	6.72 ± 1.95	6.00 ± 1.84	70.0 ± 23.5	58.0 ± 16.9	51.8 ± 15.9
$\text{Ni}_{0.6}\text{Al}_{0.4}\text{O}_x\text{H}_y$ _{100mC} (<i>N</i> = 6)	5.29 ± 2.43	4.61 ± 2.06	4.23 ± 2.57	45.7 ± 21.0	39.8 ± 17.8	36.5 ± 22.2

Films	Thickness _{as-dep} (nm)	Thickness _{anod} (nm)	Thickness _{tafel} (nm)	Monolayers _{eq} [Ni(OH) ₂] _{as-dep}	Monolayers _{eq} [Ni(OH) ₂] _{anod}	Monolayers _{eq} [Ni(OH) ₂] _{tafel}
NiO_xH_y _{100mC} (<i>N</i> = 4)	51.9 ± 17.4	43.0 ± 12.5	38.4 ± 11.8	64.9 ± 21.8	53.8 ± 15.6	48.0 ± 14.8
$\text{Ni}_{0.6}\text{Al}_{0.4}\text{O}_x\text{H}_y$ _{100mC} (<i>N</i> = 6)	33.9 ± 15.6	29.5 ± 13.2	27.1 ± 16.4	42.3 ± 19.5	36.9 ± 16.5	33.9 ± 20.5

Table 4.10: Average cathodic peak charge, number of moles of active Ni, thickness and monolayer equivalence of Ni(OH)₂ for as-deposited, anodized and after Tafel NiO_xH_y _{100mC} and $\text{Ni}_{0.6}\text{Al}_{0.4}\text{O}_x\text{H}_y$ _{100mC} films measured in 1 M Fe-free KOH.

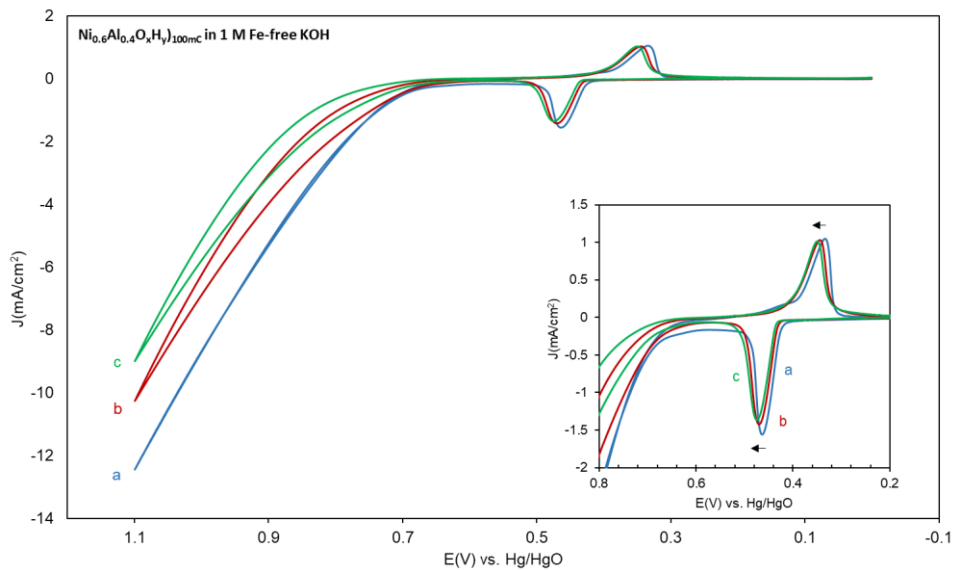


Figure 4.18: Cyclic voltammograms in 1 M Fe-free KOH at $\text{Ni}_{0.6}\text{Al}_{0.4}\text{O}_x\text{H}_y)_{100\text{mC}}$ as a first scan (a, blue), after anodic conditioning in the same solution (b, red) and after Tafel measurements (c, green). The insets show the corresponding redox peaks and onset of oxygen evolution for the three scans shown. Scan rate is 10 mV/s.

We studied the effects of co-deposited Al in $\text{Ni}_{0.6}\text{Al}_{0.4}\text{O}_x\text{H}_y)_{100\text{mC}}$ on the electrochemical behavior and OER in 1 M Fe-free KOH. Figure 4.18 shows CVs of $\text{Ni}_{0.6}\text{Al}_{0.4}\text{O}_x\text{H}_y)_{100\text{mC}}$ at 10 mV/s in 1 M Fe-free KOH: as-deposited (a), after anodic conditioning (b) and after Tafel measurements (c). A sharp anodic peak can be seen at 0.46 ± 0.01 V vs. Hg/HgO ($N = 6$) and a sharp cathodic peak at 0.34 ± 0.02 V vs. Hg/HgO. The anodic peak of $\text{Ni}_{0.6}\text{Al}_{0.4}\text{O}_x\text{H}_y)_{100\text{mC}}$ (33.9 \pm 15.6 nm thick and 42.3 \pm 19.5 $\text{Ni}(\text{OH})_2$ monolayers) anodically shifted from 0.465 ± 0.010 V to 0.487 ± 0.010 V and the cathodic peak from 0.344 ± 0.018 V to 0.372 ± 0.024 V after Tafel measurements in 1 M Fe-free KOH. Higher reversibility was seen at $\text{Ni}_{0.6}\text{Al}_{0.4}\text{O}_x\text{H}_y)_{100\text{mC}}$ in comparison to $\text{NiO}_x\text{H}_y)_{100\text{mC}}$ (Table 4.11). The average Ni content was 65 \pm 37 % in as-deposited $\text{Ni}_{0.6}\text{Al}_{0.4}\text{O}_x\text{H}_y)_{100\text{mC}}$ relative to $\text{NiO}_x\text{H}_y)_{100\text{mC}}$ in Fe-free KOH.

Films	As-Deposited				Anodized			
	$E_{p,a}$	$E_{p,c}$	ΔE_p	$E_{1/2}$	$E_{p,a}$	$E_{p,c}$	ΔE_p	$E_{1/2}$
	(mV)	(mV)	(mV)	(mV)	(mV)	(mV)	(mV)	(mV)
<i>NiO_xH_y</i> _{100mC} (N = 4)	464 ± 12	325 ± 6	140 ± 16	395 ± 5	468 ± 12	334 ± 7	134 ± 13	401 ± 7
<i>Ni_{0.6}Al_{0.4}O_xH_y</i> _{100mC} (N = 6)	465 ± 10	344 ± 18	121 ± 22	404 ± 10	470 ± 10	358 ± 19	112 ± 16	414 ± 13
Films	Tafel							
	$E_{p,a}$	$E_{p,c}$	ΔE_p	$E_{1/2}$				
	(mV)	(mV)	(mV)	(mV)				
<i>NiO_xH_y</i> _{100mC} (N = 4)	471 ± 6	343 ± 8	128 ± 13	407 ± 4				
<i>Ni_{0.6}Al_{0.4}O_xH_y</i> _{100mC} (N = 6)	487 ± 10	372 ± 24	115 ± 15	429 ± 17				

Table 4.11: Average anodic and cathodic peak positions, peak separation and half-wave potentials for as-deposited, anodized and after Tafel NiO_xH_y)_{100mC} and $Ni_{0.6}Al_{0.4}O_xH_y$)_{100mC} films measured in 1 M Fe-free KOH. E_p and $E_{1/2}$ values are reported vs. Hg/HgO.

Films	Charge _{as-dep} (mC/cm ²)	Charge _{anod} (mC/cm ²)	Charge _{tafel} (mC/cm ²)	nmol _{Ni} /cm ² _{as-dep}	nmol _{Ni} /cm ² _{anod}	nmol _{Ni} /cm ² _{tafel}
NiO _x H _y) _{100mC} (N = 2)	10.0 ± 3.75	8.10 ± 2.47	6.31 ± 2.18	86.2 ± 32.4	70.0 ± 21.3	54.5 ± 18.8
Ni _{0.6} Al _{0.4} O _x H _y) _{100mC} (N = 3)	6.01 ± 3.35	5.05 ± 2.57	4.63 ± 2.84	51.9 ± 29.0	43.6 ± 22.2	40.0 ± 25.6

Films	Thickness _{as-dep} (nm)	Thickness _{anod} (nm)	Thickness _{tafel} (nm)	Monolayers _{eq} [Ni(OH) ₂] _{as-dep}	Monolayers _{eq} [Ni(OH) ₂] _{anod}	Monolayers _{eq} [Ni(OH) ₂] _{tafel}
NiO _x H _y) _{100mC} (N = 2)	64.0 ± 24.0	51.9 ± 15.8	40.4 ± 13.9	79.9 ± 30.1	64.9 ± 19.7	50.6 ± 17.4
Ni _{0.6} Al _{0.4} O _x H _y) _{100mC} (N = 3)	38.5 ± 21.5	32.3 ± 16.4	29.7 ± 18.2	48.1 ± 26.8	40.4 ± 20.6	37.1 ± 22.8

Table 4.12: Average cathodic peak charge, number of moles of active Ni, thickness and monolayer equivalence of Ni(OH)₂ for as-deposited, anodized and after Tafel NiO_xH_y)_{100mC} and Ni_{0.6}Al_{0.4}O_xH_y)_{100mC} films measured in 1 M KOH.

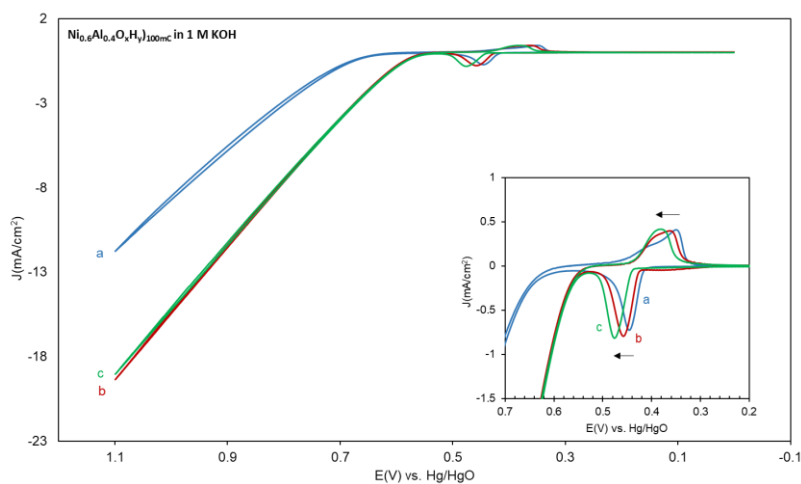


Figure 4.19: Cyclic voltammograms in 1 M KOH at Ni_{0.6}Al_{0.4}O_xH_y)_{100mC} as a first scan (a, blue), after anodic conditioning in the same solution (b, red) and after Tafel measurements (c, green). The insets show the corresponding redox peaks and onset of oxygen evolution for the three scans shown. Scan rate is 10 mV/s.

The effects of co-deposited Al in thicker $\text{Ni}_{0.6}\text{Al}_{0.4}\text{O}_x\text{H}_y$)_{100mC} on the electrochemical behavior and OER was also studied in 1 M unpurified KOH. Figure 4.19 shows CVs of $\text{Ni}_{0.6}\text{Al}_{0.4}\text{O}_x\text{H}_y$)_{100mC} at 10 mV/s in 1 M KOH: as-deposited (a), after anodic conditioning (b) and after Tafel measurements (c). A sharp anodic peak can be seen at 0.44 ± 0.01 V vs. Hg/HgO (N = 3) and a cathodic peak at 0.33 ± 0.02 V vs. Hg/HgO. The anodic peak of $\text{Ni}_{0.6}\text{Al}_{0.4}\text{O}_x\text{H}_y$)_{100mC} (38.5 ± 21.5 nm thick and 48.1 ± 26.8 Ni(OH)₂ monolayers) anodically shifted from 0.445 ± 0.015 V to 0.470 ± 0.013 V after Tafel measurements while remaining at 0.445 ± 0.016 V after anodic conditioning while the cathodic peak anodically shifted from 0.328 ± 0.019 V to 0.336 ± 0.024 V and 0.350 ± 0.029 V after anodic conditioning and Tafel measurements in 1 M KOH, respectively. Higher reversibility was seen at $\text{Ni}_{0.6}\text{Al}_{0.4}\text{O}_x\text{H}_y$)_{100mC} in comparison to NiO_xH_y)_{100mC} (Table 4.13). The average Ni content was 60 ± 40 % in as-deposited $\text{Ni}_{0.6}\text{Al}_{0.4}\text{O}_x\text{H}_y$)_{100mC} relative to NiO_xH_y)_{100mC} in KOH.

Films	As-Deposited				Anodized			
	$E_{p,a}$ (mV)	$E_{p,c}$ (mV)	ΔE_p (mV)	$E_{1/2}$ (mV)	$E_{p,a}$ (mV)	$E_{p,c}$ (mV)	ΔE_p (mV)	$E_{1/2}$ (mV)
$NiO_xH_y)_{100mC}$ ($N = 2$)	472 ± 25	315 ± 10	157 ± 16	394 ± 18	479 ± 2	327 ± 1	152 ± 1	403 ± 1
$Ni_{0.6}Al_{0.4}O_xH_y)_{100mC}$ ($N = 3$)	445 ± 15	328 ± 19	117 ± 23	387 ± 12	455 ± 16	336 ± 24	120 ± 26	396 ± 16
Films	Tafel							
	$E_{p,a}$ (mV)	$E_{p,c}$ (mV)	ΔE_p (mV)	$E_{1/2}$ (mV)				
$NiO_xH_y)_{100mC}$ ($N = 2$)	488 ± 4	340 ± 0	148 ± 4	414 ± 2				
$Ni_{0.6}Al_{0.4}O_xH_y)_{100mC}$ ($N = 3$)	470 ± 13	350 ± 29	120 ± 29	410 ± 17				

Table 4.13: Average anodic and cathodic peak positions, peak separation and half-wave potentials for as-deposited, anodized and after Tafel $NiO_xH_y)_{100mC}$ and $Ni_{0.6}Al_{0.4}O_xH_y)_{100mC}$ films measured in 1 M KOH. E_p and $E_{1/2}$ values are reported vs. Hg/HgO.

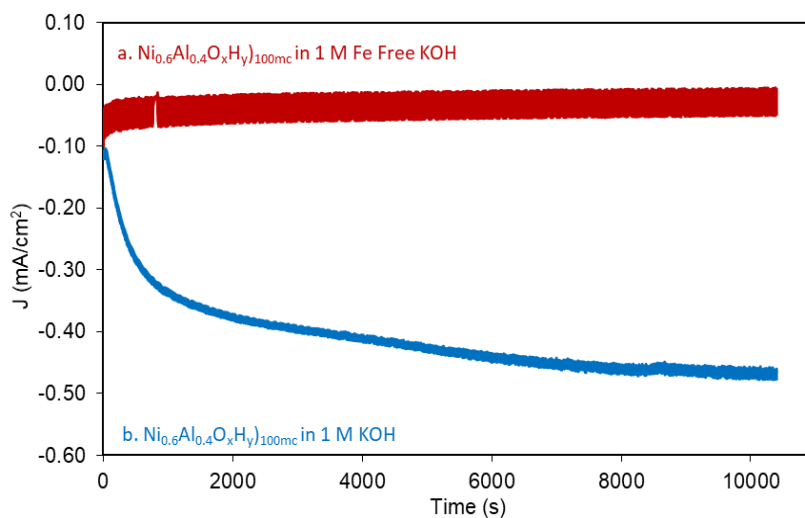


Figure 4.20: Anodization plots (i-t plots) of ultra-thin $Ni_{0.6}Al_{0.4}O_xH_y)_{100mC}$ films biased at 0.58 V vs. Hg/HgO in 1 M Fe-free KOH (a, red traces) or unpurified 1 M KOH (b, blue traces) as indicated.

As-deposited $\text{Ni}_{0.6}\text{Al}_{0.4}\text{O}_x\text{H}_y$)_{100mC} can be concluded to not be more OER active than NiO_xH_y)_{100mC} as seen in the as-deposited CVs in both 1 M Fe-free KOH and 1 M KOH. With anodic conditioning and Tafel measurements, the OER activity decreases in 1 M Fe-free KOH and increases in 1 M KOH similar to the behavior and activity of NiO_xH_y)_{100mC} in these solutions. The films deposited for 30 min in KBi with Fe traces still needed anodic conditioning for further activation of OER catalysis in 1 M KOH. OER current increased and the onset decreased after anodization and remained the same after Tafel indicating catalyst stability. The anodization i-t curves (Figure 4.20) showed an initial decrease in currents in 1 M Fe-free KOH (which almost plateaued with time) and an increase in currents in 1 M unpurified KOH consistent with the previous data in Fe-containing KOH discussed in Chapter 3.X and Chapter 4.A.2 and 4.A.3 for the thin films. During anodic electrodeposition, Fe is co-depositing with both NiO_xH_y)_{100mC} and $\text{Ni}_{0.6}\text{Al}_{0.4}\text{O}_x\text{H}_y$)_{100mC} and initially forming active Fe sites in the catalyst. The OER activity of $\text{Ni}_{0.6}\text{Al}_{0.4}\text{O}_x\text{H}_y$)_{100mC} decreases with anodic conditioning and Tafel measurements in 1 M Fe-free KOH with an increase in OER onset and hysteresis. The decrease in OER activity in Fe-free KOH can be attributed to active Fe moving to the bulk, or the film reverting to a less active structure.

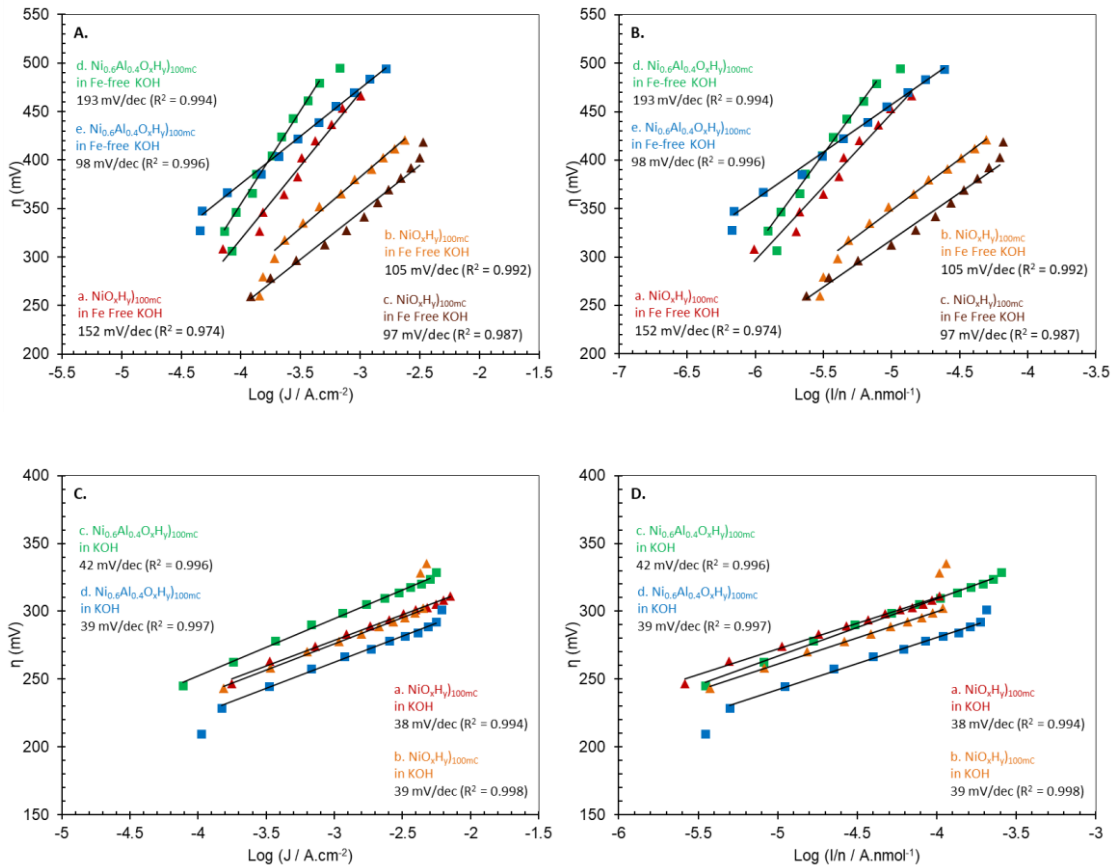


Figure 4.21: Tafel plots (A, C) and normalized Tafel plots (B, D) for $\text{NiO}_x\text{H}_y)_{100\text{mC}}$ (red, orange, brown; ▲) and $\text{Ni}_{0.6}\text{Al}_{0.4}\text{O}_x\text{H}_y)_{100\text{mC}}$ (green, blue; ■) anodized in 1 M Fe-free KOH (A, B) and 1 M KOH (C, D) and measured in the same solution with the corresponding slopes for the best fit linear plot.

Figure 4.21 shows the Tafel plots (A) and normalized Tafel plots (B) of $\text{NiO}_x\text{H}_y)_{100\text{mC}}$ and $\text{Ni}_{0.6}\text{Al}_{0.4}\text{O}_x\text{H}_y)_{100\text{mC}}$ films in 1 M Fe-free KOH and 1 M KOH including those shown in Figures 3.9, 4.18 and 4.19. Tafel slopes of $\text{NiO}_x\text{H}_y)_{100\text{mC}}$ and $\text{Ni}_{0.6}\text{Al}_{0.4}\text{O}_x\text{H}_y)_{100\text{mC}}$ in 1 M Fe-free KOH were 152 and 193 mV/dec, respectively. While Tafel slopes of $\text{NiO}_x\text{H}_y)_{100\text{mC}}$ and $\text{Ni}_{0.6}\text{Al}_{0.4}\text{O}_x\text{H}_y)_{100\text{mC}}$ in 1 M KOH were 38 and 42 mV/dec, respectively. Variations in the Tafel slope have been previously discussed for 1 M Fe-free KOH, with average Tafel slopes of 118 ± 29 mV/dec and 145 ± 67

mV/dec for $\text{NiO}_x\text{H}_y)_{100\text{mC}}$ ($N = 3$) and $\text{Ni}_{0.6}\text{Al}_{0.4}\text{O}_x\text{H}_y)_{100\text{mC}}$ ($N = 2$), respectively. Smaller variations were seen in 1 M KOH, with average Tafel slopes of 38 ± 1 mV/dec and 45 ± 8 mV/dec for $\text{NiO}_x\text{H}_y)_{100\text{mC}}$ ($N = 2$) and $\text{Ni}_{0.6}\text{Al}_{0.4}\text{O}_x\text{H}_y)_{100\text{mC}}$ ($N = 3$), respectively and thus were in the reported range.^{1, 7, 92-93, 95, 144} Normalized Tafel plots in 1 M Fe-free KOH showed higher OER activity per Ni at $\text{NiO}_x\text{H}_y)_{100\text{mC}}$ with respect to $\text{Ni}_{0.6}\text{Al}_{0.4}\text{O}_x\text{H}_y)_{100\text{mC}}$ in contrast to the trend seen at the ultrathin films.

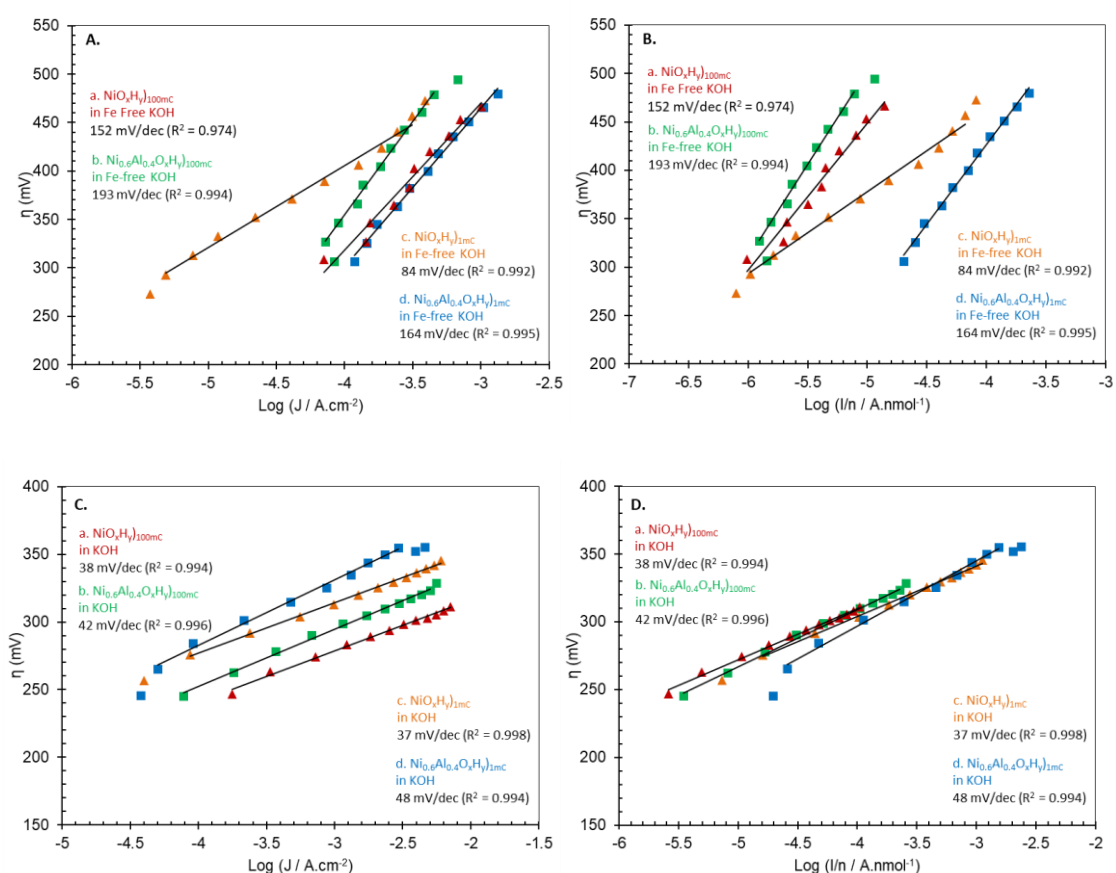


Figure 4.22: Tafel plots (A, C) and normalized Tafel plots (B, D) for $\text{NiO}_x\text{H}_y)_{100\text{mC}}$ (red \blacktriangle), $\text{Ni}_{0.6}\text{Al}_{0.4}\text{O}_x\text{H}_y)_{100\text{mC}}$ (green \blacksquare), $\text{NiO}_x\text{H}_y)_{1\text{mC}}$ (orange \blacktriangle) and $\text{Ni}_{0.6}\text{Al}_{0.4}\text{O}_x\text{H}_y)_{1\text{mC}}$ (blue \blacksquare) anodized in 1 M Fe-free KOH (A, B) and 1 M KOH (C, D) and measured in the same solution with the corresponding slopes for the best fit linear plot.

In KOH, Tafel plots showed higher OER activity at $\text{NiO}_x\text{H}_y)_{100\text{mC}}$ than $\text{NiO}_x\text{H}_y)_{1\text{mC}}$, and at $\text{Ni}_{0.6}\text{Al}_{0.4}\text{O}_x\text{H}_y)_{100\text{mC}}$ than $\text{Ni}_{0.6}\text{Al}_{0.4}\text{O}_x\text{H}_y)_{1\text{mC}}$. Normalized Tafel plots in KOH showed comparable OER activity between all four films.

In Fe-free KOH, Tafel plots showed higher OER activity at $\text{NiO}_x\text{H}_y)_{100\text{mC}}$ than $\text{NiO}_x\text{H}_y)_{1\text{mC}}$, and higher activity at $\text{Ni}_{0.6}\text{Al}_{0.4}\text{O}_x\text{H}_y)_{1\text{mC}}$ than $\text{Ni}_{0.6}\text{Al}_{0.4}\text{O}_x\text{H}_y)_{100\text{mC}}$.

Normalized Tafel plots in Fe-free KOH also showed higher activity at $\text{Ni}_{0.6}\text{Al}_{0.4}\text{O}_x\text{H}_y)_{1\text{mC}}$ than $\text{Ni}_{0.6}\text{Al}_{0.4}\text{O}_x\text{H}_y)_{100\text{mC}}$, but higher OER activity at $\text{NiO}_x\text{H}_y)_{1\text{mC}}$ than $\text{NiO}_x\text{H}_y)_{100\text{mC}}$.

A.

Films	Tafel Slope (mV/dec)	TOF _{SS-asdep} (s ⁻¹) (@ $\eta \sim 400$ mV)	TOF _{SS-anod} (s ⁻¹) (@ $\eta \sim 400$ mV)
$\text{NiO}_x\text{H}_y)_{100\text{mC}}$ (N = 3)	118 ± 29	0.067 ± 0.061 ($\eta = 402 \pm 0$ mV)	0.078 ± 0.069 ($\eta = 402 \pm 0$ mV)
$\text{Ni}_{0.6}\text{Al}_{0.4}\text{O}_x\text{H}_y)_{100\text{mC}}$ (N = 2)	145 ± 67	0.007 ± 0.001 ($\eta = 404 \pm 0$ mV)	0.008 ± 0.001 ($\eta = 404 \pm 0$ mV)
$\text{Ni}_{0.6}\text{Al}_{0.4}\text{O}_x\text{H}_y)_{100\text{mC}}$ (N = 6)	126 ± 56	0.098 ± 0.103 ($\eta = 401 \pm 4$ mV)	0.110 ± 0.114 ($\eta = 401 \pm 4$ mV)

B.

Films	Tafel Slope (mV/dec)	TOF _{SS-asdep} (s ⁻¹) (@ $\eta \sim 300$ mV)	TOF _{SS-anod} (s ⁻¹) (@ $\eta \sim 300$ mV)
$\text{NiO}_x\text{H}_y)_{100\text{mC}}$ (N = 2)	38 ± 1	0.127 ± 0.046 ($\eta = 300 \pm 2$ mV)	0.153 ± 0.045 ($\eta = 300 \pm 2$ mV)
$\text{Ni}_{0.6}\text{Al}_{0.4}\text{O}_x\text{H}_y)_{100\text{mC}}$ (N = 3)	45 ± 8	0.163 ± 0.187 ($\eta = 299 \pm 2$ mV)	0.188 ± 0.217 ($\eta = 299 \pm 2$ mV)

Table 4.14: Average Tafel slope, apparent TOF for O₂ per second per Ni center calculated at an overpotential of ~ 400 mV from steady-state current measurements under stirring for as-deposited and anodized $\text{NiO}_x\text{H}_y)_{100\text{mC}}$ and $\text{Ni}_{0.6}\text{Al}_{0.4}\text{O}_x\text{H}_y)_{100\text{mC}}$ films measured in 1 M Fe-free KOH (A) and 1 M KOH (B).

The average steady-state $\text{TOF}_{400\text{mV}}$ in Fe-free KOH for as-deposited $\text{Ni}_{0.6}\text{Al}_{0.4}\text{O}_x\text{H}_y)_{100\text{mC}}$ ($N = 2$) equaled to $0.01 \pm 0.00 \text{ s}^{-1}$ and for as-deposited $\text{NiO}_x\text{H}_y)_{100\text{mC}}$ ($N = 3$) equaled to $0.07 \pm 0.06 \text{ s}^{-1}$, indicating that Al is reducing activity per Ni in thicker films. A wide variation in $\text{TOF}_{400\text{mV}}$ of $\text{Ni}_{0.6}\text{Al}_{0.4}\text{O}_x\text{H}_y)_{100\text{mC}}$ was calculated. Two of these measurements ($N = 2$ in Table 4.14) were conducted vs. Hg/HgO reference electrodes which were filled with and stored in 1 M Fe-free (purified) NaOH. The cell setup was also thoroughly rinsed with Fe-free solution. Further experiments are needed to study $\text{NiO}_x\text{H}_y)_{100\text{mC}}$ under similar conditions. Higher $\text{TOF}_{400\text{mV}}$ was seen at $\text{Ni}_{0.6}\text{Al}_{0.4}\text{O}_x\text{H}_y)_{100\text{mC}}$ ($N = 6$) with possible suspected presence of Fe traces in solution. Therefore, the effect of Al co-deposition on the OER of $\text{NiO}_x\text{H}_y)_{100\text{mC}}$ in the absence of Fe still requires further investigation, especially as a function of film thickness.

In KOH, $\text{TOF}_{300\text{mV}}$ for as-deposited $\text{Ni}_{0.6}\text{Al}_{0.4}\text{O}_x\text{H}_y)_{100\text{mC}}$ ($N = 3$) equaled to $0.16 \pm 0.19 \text{ s}^{-1}$ and for as-deposited $\text{NiO}_x\text{H}_y)_{100\text{mC}}$ ($N = 2$) equaled to $0.13 \pm 0.05 \text{ s}^{-1}$, indicating possibly better OER with Al and Fe in solution but with significant variation. The ratios of the average steady-state TOF for as-deposited $\text{Ni}_{0.6}\text{Al}_{0.4}\text{O}_x\text{H}_y)_{100\text{mC}}$ to $\text{NiO}_x\text{H}_y)_{100\text{mC}}$ in Fe-free KOH and KOH equaled to 0.11 and 1.28, respectively. A similar trend was seen in the anodized $\text{Ni}_{0.6}\text{Al}_{0.4}\text{O}_x\text{H}_y)_{100\text{mC}}$ and $\text{NiO}_x\text{H}_y)_{100\text{mC}}$ films in both solutions as their corresponding as-deposited films.

Steady-state $\text{TOF}_{400\text{mV}}$ of $\text{Ni}_{0.6}\text{Al}_{0.4}\text{O}_x\text{H}_y$ in 1 M Fe-free KOH and $\text{TOF}_{300\text{mV}}$ in 1 M KOH decreased with increased loading. The TOF was $0.007 \pm 0.001 \text{ s}^{-1}$ at $\text{Ni}_{0.6}\text{Al}_{0.4}\text{O}_x\text{H}_y)_{100\text{mC}}$ ($N = 2$) compared to $0.209 \pm 0.097 \text{ s}^{-1}$ at $\text{Ni}_{0.6}\text{Al}_{0.4}\text{O}_x\text{H}_y)_{1\text{mC}}$ ($N = 2$) in Fe-free KOH showing a thickness dependence. On the other hand, NiO_xH_y showed significantly smaller variation with thickness in both solutions. For instance, the TOF

equaled $0.067 \pm 0.061 \text{ s}^{-1}$ at $\text{NiO}_x\text{H}_y)_{100\text{mC}}$ compared to $0.093 \pm 0.035 \text{ s}^{-1}$ at $\text{NiO}_x\text{H}_y)_{1\text{mC}}$ in Fe-free KOH. Baker et al. reported the strong thickness dependence of TOF for Ni-Al-Fe-OOH films with a significant decrease in TOF with increasing number of monolayers, which was not seen for Ni-Fe-OOH, and attributed it to morphological and electronic structure changes with Al.¹⁴⁴

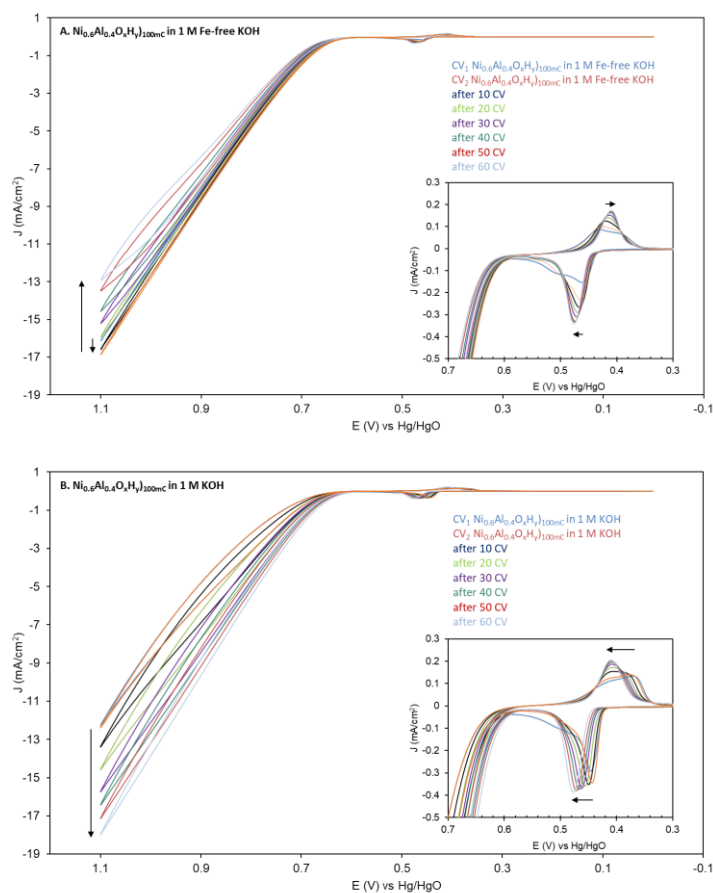


Figure 4.23: Cyclic voltammograms of $\text{Ni}_{0.6}\text{Al}_{0.4}\text{O}_x\text{H}_y)_{100\text{mC}}$ film in 1 M Fe-free KOH (A) and 1 M KOH (B), as a first (CV₁ blue) and second (CV₂ orange) scan and CVs acquired after 10 CVs were taken at 100 mV/s, repeated 6 times in the same solution. Scan rate of all CVs in this figure is 10 mV/s. The inset shows the $\text{Ni(OH)}_2/\text{NiOOH}$ redox peaks and onset of oxygen evolution. The number of CVs (10-60) refers to the total number of scans acquired at 100 mV/s.

We investigated the effect of potential cycling in 1 M Fe-free KOH and 1 M unpurified KOH on the electrochemical behavior and OER activity of thicker co-deposited $\text{Ni}_{0.6}\text{Al}_{0.4}\text{O}_x\text{H}_y$ films. Figure 4.23 shows a first and second scan CV at $\text{Ni}_{0.6}\text{Al}_{0.4}\text{O}_x\text{H}_y$ in 1 M Fe-free KOH (A) and in 1 M KOH (B) at 10 mV/s and then after 10 CVs at 100 mV/s, repeated six times. In Fe-free KOH, OER currents slightly increased and onset slightly decreased with the second scan followed by gradual decrease in currents, increase in onset and hysteresis and appearance of the anodic wave with potential cycling. The slight initial increase in activity might be due to surface restructuring with some Fe that was co-included from the deposition and activating some surface sites. In KOH, the OER currents increased and onset decreased with the second scan and further potential cycling. The OER activity behavior follows the expected trend in each solution as observed for the ultrathin films despite the possibility of higher Fe inclusion for thicker films during deposition. The major $\text{Ni}(\text{OH})_2/\text{NiOOH}$ redox peaks in the as-deposited $\text{Ni}_{0.6}\text{Al}_{0.4}\text{O}_x\text{H}_y$ films in the Fe-free solution showed significant peak splitting with a larger peak charge for the more positive shoulder in the cathodic peak and for the more negative shoulder in the anodic peak. The anodic peaks merged forming a sharper peak near the initially larger shoulder and shifted anodically with potential cycling. The cathodic peaks also merged forming a sharper peak near the larger peak and shifted cathodically with potential cycling. A cathodic shift has been reported to be an indication of Al leaching out of the films.¹⁴⁴ In contrast, the major $\text{Ni}(\text{OH})_2/\text{NiOOH}$ redox peaks in the as-deposited films in unpurified KOH showed significant peak splitting with a larger peak charge for the more negative shoulder in the cathodic peak and for the more negative shoulder in the anodic peak. The anodic peaks

also merged forming a sharper peak near the initially larger shoulder and shifted anodically with potential cycling. The cathodic peaks also merged forming a sharper peak near the larger shoulder and shifted anodically with potential cycling. The anodic shifts here are attributed to Fe inclusion. The redox peak charges in both solutions decreased with the second scan, increased with the first 10 CVs and then remained almost unchanged (or slightly decreased as for the cathodic peak in 1 M KOH) with the rest of the potential cycling. Thus, dissolution cannot be clearly deduced from the peak charges.

The literature showed that Al co-deposition leads to an enhancement effect with respect to pure NiO_xH_y in KOH, possibly due to Al interacting with neighboring Fe sites, acquired from the unpurified solution (during deposition, film preparation, conditioning and cycling), and thus, leading to the formation of more OER active sites via inducing electronic and morphological changes and increasing film conductivity.¹⁴⁴⁻

145

C. Conclusions

This chapter investigated the effect of mode of inclusion of Al on OER at NiO_xH_y in different electrolytes in the presence and absence of Fe in solution. It was observed and concluded from these studies that:

A. In 1 M KBi:

- 1) Without Al in solution, OER currents of Ni-Bi increase with potential cycling in KBi, anodic peak charge decreases minimally and peaks remain sharp, and cathodic peak charge decreases (ca. 62%).

- 2) With Al in KBi, OER activity of Ni-Bi decreases, cathodic peak charge decreases comparably (ca. 50%) to the absence of Al, but anodic peak charge significantly decreases compared to its absence. The effect of Al is most noticeable on OER and on the anodic peak, as the ratio of anodic to cathodic peak charge decreases from 0.93 initially to 0.16 after the addition of 0.08 mM Al³⁺ and 60 CVs, and from 0.88 to 0.10 after the addition of 0.32 mM Al³⁺ and 60 CVs. Therefore, it appears that Al inclusion is affecting the oxidation of Ni(OH)₂ to NiOOH possibly leading to a decrease in OER, despite the presence of Fe in solution.
- 3) The effect of Al in KBi was concentration dependent as at a concentration of 0.01 mM, OER did not decrease but Al still prevented Fe traces in solution from enhancing OER.
- 4) The usual increase in OER activity was seen at co-deposited Ni_{1-x}Al_x-Bi films with anodization, and redox peak behavior was also unaffected (no decrease in peak charges) except for lower ΔE_p caused by Al co-inclusion.
- 5) Tafel plots showed similar Tafel slopes (ca. 40 mV/dec) and OER activity between Ni_{0.6}Al_{0.4}-Bi)_{1mC} and Ni-Bi)_{1mC}, but with TOF_{400mV} slightly on average lower with Al co-inclusion.
- 6) Al generally has a negative effect on OER with both deposition methods (uptake from solution and co-deposition) in KBi.

B. In 1 M Unpurified KOH:

- 1) The addition of Al to unpurified KOH resulted in an anodic shift in redox peaks as observed in its absence, major splitting of cathodic peak, no change in anodic peak charge and an increase in OER currents. The increase in OER is attributed to Fe in

KOH. Al inclusion is thus indicating the presence two different Ni sites as evident in the peak splitting without affecting OER.

- 2) A clear cathodic peak splitting was observed at co-deposited $\text{Ni}_{0.6}\text{Al}_{0.4}\text{O}_x\text{H}_y$ films with potential cycling, but not observed at NiO_xH_y films when potential was cycled (without Al co-deposition). Further evidence of Al inclusion and its effect on differentiating Ni sites.
- 3) With Al co-deposition in thin films, cathodic peak splitting was observed with an increase in OER currents post-anodization and a slight anodic shift in $E_{1/2}$ post-Tafel. While with Al co-deposition in thick films $E_{1/2}$ was not anodically shifted but a smaller ΔE_p was observed in comparison to NiO_xH_y .
- 4) Tafel plots showed similar Tafel slopes and OER activity between $\text{Ni}_{0.6}\text{Al}_{0.4}\text{O}_x\text{H}_y$ and NiO_xH_y , but with larger average $\text{TOF}_{300\text{mV}}$ with Al co-deposition in the presence of Fe traces in solution for both thin and thick films indicating a possible synergistic effect between Al and Fe.

C. In 1 M Fe-free KOH

- 1) The addition of Al to Fe-free KOH resulted in an anodic shift and splitting of redox peaks (not observed in the absence of Al), and a decrease in OER activity. Therefore, Al inclusion in $\text{Ni}(\text{OH})_2$ (in the absence of Fe) does not cause an increase in OER. It does not significantly decrease the peak charges (like in KBi).
- 2) Co-deposited $\text{Ni}_{0.6}\text{Al}_{0.4}\text{O}_x\text{H}_y$ films resulted in similar peak position to NiO_xH_y after anodization in Fe-free KOH, and an anodic shift in redox peaks and increase in hysteresis post-Tafel. However, OER onset remained constant. Therefore, Al co-deposition does not cause an enhancement of OER in Fe-free KOH.

- 3) The co-deposition of Al in thin and thick $\text{Ni}_{0.6}\text{Al}_{0.4}\text{O}_x\text{H}_y$ in Fe-free KOH resulted in a more positive average $E_{1/2}$ but no decrease in ΔE_p only in thin $\text{Ni}_{0.6}\text{Al}_{0.4}\text{O}_x\text{H}_y$ as seen in KBi.
- 4) Cycling the potential of co-deposited thin and thick $\text{Ni}_{0.6}\text{Al}_{0.4}\text{O}_x\text{H}_y$ films in Fe-free KOH resulted in almost no change in redox peak charges but a decrease in OER.
- 5) Tafel slopes were comparable (not lower) on average with Al inclusion, but showing variations due to the possible different levels of Fe traces in the purified Fe-free solution. Average $\text{TOF}_{400\text{mV}}$ is higher with Al inclusion for thin films, even after thorough purification from Fe, but $\text{TOF}_{400\text{mV}}$ is lower with Al inclusion in thicker films after thorough purification, requiring further investigation.

D. Future Studies:

- 1) Future studies are needed to test the effect of mode of inclusion of Al on OER and redox behavior of Ni-Bi in KBi at different film thicknesses.
- 2) Future studies are needed using EQCM to investigate leaching and the effect of Al on the stability of Ni-Bi films in KBi and KOH
- 3) Further studies are needed to detect and understand the possible changes of conductivity and morphology with different film thickness occurring due to Al co-deposition and Al inclusion from solution on NiO_xH_y .
- 4) Further studies are needed to conclude on the effect of Al in the absence of Fe in solution for both thin and thicker films with further purification of reference electrode filling and storage solutions and overall setup as different effects were observed for thin and thick films.
- 5) Future studies are needed to examine the effect of Al in solution at different electrolyte concentrations and pH values on the formation of various Al complexes

and their subsequent effect on OER activity and electrochemical behavior of NiO_xH_y .

CHAPTER V

CONCLUSION

We have conducted in this thesis work an electrochemical study on the effect of Fe and Al on the redox behavior and OER catalysis on Ni-oxo/hydroxide of different thicknesses as a function of method of deposition and in the presence and absence of Fe in electrolyte.

In the study of the effect of Fe on the electrochemistry and OER of Ni-oxo/hydroxide (Chapter 3), anodically deposited NiFe-oxo/hydroxide films did not exhibit high OER activity in the absence of Fe from solution. High OER activity is attributed to surface sites activated by Fe from solution rather than bulk-Fe inclusion. The decrease in OER activity seen at Fe-activated NiO_xH_y films in the absence of Fe in solution is proposed to be due to Fe from low coordination active surface-Fe sites becoming higher coordination bulk-Fe sites. Further studies are needed to investigate the dependence of the sustainability of active sites and their deactivation mechanism on film thickness and the deposition method used, hence initial crystallinity.

In the study of the effect of Al on the electrochemistry and OER of Ni-oxo/hydroxide (Chapter 4), we investigated the effect of Al in KBi and KOH. The addition of Al to KBi lowers OER activity at Ni-Bi and significantly decreases its anodic peak charges. Al is indicated to make the oxidation of Ni(OH)₂ to NiOOH in KBi harder and thus, leading to a decrease in OER activity despite the presence of Fe in solution. Co-deposited Ni_{1-x}Al_x-Bi films showed the usual increase in OER currents with anodization in KBi and no change in redox peak behavior except for decreased ΔE_p with Al co-inclusion. Comparable Tafel slopes were observed with Al co-deposition in KBi but with slightly lower average TOF_{400mV}. The addition of Al to unpurified KOH

resulted in an anodic shift in redox peaks, cathodic peak splitting, no change in anodic peak charge and an increase in OER activity attribute to Fe in KOH. The addition of Al to Fe-free KOH resulted in similar redox behavior as in KOH but with a decrease in OER activity. Thus, Al inclusion in KOH and Fe-free KOH is affecting two different Ni sites with no effect on OER. Tafel plots in KOH showed similar Tafel slopes with Al co-deposition. Larger average $\text{TOF}_{300\text{mV}}$ was seen for both thin and thick films with Al co-deposition in KOH (in the presence of Fe in solution). Co-deposited $\text{Ni}_{0.6}\text{Al}_{0.4}\text{O}_x\text{H}_y$ films showed similar redox behavior as NiO_xH_y in Fe-free KOH with a constant OER onset. Thus, Al co-deposition does not cause an enhancement of OER in Fe-free KOH. Average Tafel slopes were similar (not lower) with Al inclusion in Fe-free KOH, with variation depending on different levels of Fe traces in solution. Average $\text{TOF}_{400\text{mV}}$ in Fe-free KOH is larger with Al co-deposition in thin films (even after thorough setup purification from Fe) while lower with Al co-deposition in thicker films after thorough purification requiring further study. Further studies are needed using EQCM to examine the effect of Al on the stability of Ni-oxo/hydroxide films in KBi, KOH and Fe-free KOH, and to investigate possible changes in the conductivity and morphology of NiO_xH_y films at different thickness with Al inclusion. Further studies are needed to examine the effect of Al inclusion from solution at different electrolyte pH values and concentrations on redox behavior and OER catalysis.

These OER catalysts have potential to pave the way for more efficient and low cost solar water splitting by coupling these earth abundant co-catalyst materials to photoelectrodes. Future studies should address the coupling of these catalysts to photoelectrochemical cells for solar water splitting, and the effect of different factors

(such as deposition technique, catalyst morphology and crystallinity, and electrolyte composition) on sustainability and efficiency.

REFERENCES

1. Fayad, R.; Dhainy, J.; Ghandour, H.; Halaoui, L., Electrochemical study of the promoting effect of Fe on oxygen evolution at thin 'NiFe–Bi' films and the inhibiting effect of Al in borate electrolyte. *Catal. Sci. Technol* **2017**, *7* (17), 3876-3891.
2. Cook, T. R.; Dogutan, D. K.; Reece, S. Y.; Surendranath, Y.; Teets, T. S.; Nocera, D. G., Solar energy supply and storage for the legacy and nonlegacy worlds. *Chem. Rev.* **2010**, *110* (11), 6474-6502.
3. Mao, S. S.; Shen, S.; Guo, L., Nanomaterials for renewable hydrogen production, storage and utilization. *Progress in Natural Science: Materials International* **2012**, *22* (6), 522-534.
4. Lewis, N. S.; Crabtree, G., Basic research needs for solar energy utilization: report of the basic energy sciences workshop on solar energy utilization. US Department of Energy, Office of Basic Energy Science: 2005.
5. Dincă, M.; Surendranath, Y.; Nocera, D. G., Nickel-borate oxygen-evolving catalyst that functions under benign conditions. *Proc. Natl. Acad. Sci.* **2010**, *107* (23), 10337-10341.
6. Zhao, J.; Ren, X.; Han, Q.; Fan, D.; Sun, X.; Kuang, X.; Wei, Q.; Wu, D., Ultra-thin wrinkled NiOOH–NiCr₂O₄ nanosheets on Ni foam: an advanced catalytic electrode for oxygen evolution reaction. *Chem. Commun.* **2018**, *54* (39), 4987-4990.
7. Bediako, D. K.; Surendranath, Y.; Nocera, D. G., Mechanistic studies of the oxygen evolution reaction mediated by a nickel–borate thin film electrocatalyst. *J. Am. Chem. Soc.* **2013**, *135* (9), 3662-3674.
8. Eriksson, E.; Gray, E. M., Optimization and integration of hybrid renewable energy hydrogen fuel cell energy systems—A critical review. *Applied energy* **2017**, *202*, 348-364.
9. Ciamician, G., The photochemistry of the future. *Science* **1912**, *36* (926), 385-394.
10. Barber, J., Photosynthetic energy conversion: natural and artificial. *Chem. Soc. Rev.* **2009**, *38* (1), 185-196.
11. Nocera, D. G., The artificial leaf. *Acc. Chem. Res.* **2012**, *45* (5), 767-776.
12. Barber, J., Biological solar energy. *Philosophical Transactions of the Royal Society A: Mathematical, Physical and Engineering Sciences* **2007**, *365* (1853), 1007-1023.
13. Hisatomi, T.; Kubota, J.; Domen, K., Recent advances in semiconductors for photocatalytic and photoelectrochemical water splitting. *Chem. Soc. Rev.* **2014**, *43* (22), 7520-7535.
14. Fujishima, A.; Honda, K., Electrochemical Photolysis of Water at a Semiconductor Electrode. *Nature* **1972**, *238* (5358), 37-38.
15. Ismail, A. A.; Bahnemann, D. W., Photochemical splitting of water for hydrogen production by photocatalysis: a review. *Sol. Energy Mater. Sol. Cells* **2014**, *128*, 85-101.
16. Tee, S. Y.; Win, K. Y.; Teo, W. S.; Koh, L. D.; Liu, S.; Teng, C. P.; Han, M. Y., Recent progress in energy-driven water splitting. *Advanced Science* **2017**, *4* (5), 1600337.
17. Chu, S.; Li, W.; Yan, Y.; Hamann, T.; Shih, I.; Wang, D.; Mi, Z., Roadmap on solar water splitting: current status and future prospects. *Nano Futures* **2017**, *1* (2), 022001.

18. Zhang, L.; Zhao, H.; Wilkinson, D. P.; Sun, X.; Zhang, J., *Electrochemical Water Electrolysis: Fundamentals and Technologies*. CRC Press: 2020.
19. De Levie, R., The electrolysis of water. *J. Electroanal. Chem.* **1999**, *476* (1), 92-93.
20. Dau, H.; Limberg, C.; Reier, T.; Risch, M.; Roggan, S.; Strasser, P., The mechanism of water oxidation: from electrolysis via homogeneous to biological catalysis. *ChemCatChem* **2010**, *2* (7), 724-761.
21. LeRoy, R., Industrial water electrolysis: present and future. *Int. J. Hydrogen Energy* **1983**, *8* (6), 401-417.
22. Suen, N.-T.; Hung, S.-F.; Quan, Q.; Zhang, N.; Xu, Y.-J.; Chen, H. M., Electrocatalysis for the oxygen evolution reaction: recent development and future perspectives. *Chem. Soc. Rev.* **2017**, *46* (2), 337-365.
23. Walter, M. G.; Warren, E. L.; McKone, J. R.; Boettcher, S. W.; Mi, Q.; Santori, E. A.; Lewis, N. S., Solar water splitting cells. *Chem. Rev.* **2010**, *110* (11), 6446-6473.
24. Suntivich, J.; May, K. J.; Gasteiger, H. A.; Goodenough, J. B.; Shao-Horn, Y., A perovskite oxide optimized for oxygen evolution catalysis from molecular orbital principles. *Science* **2011**, *334* (6061), 1383-1385.
25. Frydendal, R.; Paoli, E. A.; Knudsen, B. P.; Wickman, B.; Malacrida, P.; Stephens, I. E.; Chorkendorff, I., Benchmarking the stability of oxygen evolution reaction catalysts: the importance of monitoring mass losses. *ChemElectroChem* **2014**, *1* (12), 2075-2081.
26. Reier, T.; Nong, H. N.; Teschner, D.; Schlögl, R.; Strasser, P., Electrocatalytic oxygen evolution reaction in acidic environments—reaction mechanisms and catalysts. *Advanced Energy Materials* **2017**, *7* (1), 1601275.
27. Shinagawa, T.; Garcia-Esparza, A. T.; Takanabe, K., Insight on Tafel slopes from a microkinetic analysis of aqueous electrocatalysis for energy conversion. *Scientific reports* **2015**, *5*, 13801.
28. Rossmeisl, J.; Qu, Z.-W.; Zhu, H.; Kroes, G.-J.; Nørskov, J. K., Electrolysis of water on oxide surfaces. *J. Electroanal. Chem.* **2007**, *607* (1-2), 83-89.
29. Trasatti, S., Electrocatalysis by oxides—attempt at a unifying approach. *J. Electroanal. Chem* **1980**, *111* (1), 125-131.
30. McCrory, C. C.; Jung, S.; Peters, J. C.; Jaramillo, T. F., Benchmarking heterogeneous electrocatalysts for the oxygen evolution reaction. *J. Am. Chem. Soc.* **2013**, *135* (45), 16977-16987.
31. Doyle, R.; Lyons, M., Kinetics and mechanistic aspects of the oxygen evolution reaction at hydrous iron oxide films in base. *J. Electrochem. Soc.* **2013**, *160* (2), H142-H154.
32. Doyle, R. L.; Godwin, I. J.; Brandon, M. P.; Lyons, M. E., Redox and electrochemical water splitting catalytic properties of hydrated metal oxide modified electrodes. *PCCP* **2013**, *15* (33), 13737-13783.
33. Trasatti, S., Electrocatalysis in the anodic evolution of oxygen and chlorine. *Electrochim. Acta* **1984**, *29* (11), 1503-1512.
34. Marshall, A.; Børresen, B.; Hagen, G.; Tsytkin, M.; Tunold, R., Preparation and characterisation of nanocrystalline $\text{Ir}_x\text{Sn}_{1-x}\text{O}_2$ electrocatalytic powders. *Mater. Chem. Phys.* **2005**, *94* (2-3), 226-232.
35. Trasatti, S., Physical electrochemistry of ceramic oxides. *Electrochim. Acta* **1991**, *36* (2), 225-241.

36. Rüetschi, P.; Delahay, P., Influence of electrode material on oxygen overvoltage: a theoretical analysis. *The Journal of Chemical Physics* **1955**, *23* (3), 556-560.
37. Lodi, G.; Sivieri, E.; De Battisti, A.; Trasatti, S., Ruthenium dioxide-based film electrodes. *J. Appl. Electrochem.* **1978**, *8* (2), 135-143.
38. De Pauli, C.; Trasatti, S., Composite materials for electrocatalysis of O₂ evolution: IrO₂+ SnO₂ in acid solution. *J. Electroanal. Chem.* **2002**, *538*, 145-151.
39. Mattos-Costa, F. I.; de Lima-Neto, P.; Machado, S. A. S.; Avaca, L. A., Characterisation of surfaces modified by sol-gel derived Ru_xIr_{1-x}O₂ coatings for oxygen evolution in acid medium. *Electrochim. Acta* **1998**, *44* (8-9), 1515-1523.
40. Hoertz, P. G.; Kim, Y.-I.; Youngblood, W. J.; Mallouk, T. E., Bidentate dicarboxylate capping groups and photosensitizers control the size of IrO₂ nanoparticle catalysts for water oxidation. *J. Phys. Chem. B.* **2007**, *111* (24), 6845-6856.
41. Zhao, Y.; Hernandez-Pagan, E. A.; Vargas-Barbosa, N. M.; Dysart, J. L.; Mallouk, T. E., A high yield synthesis of ligand-free iridium oxide nanoparticles with high electrocatalytic activity. *The Journal of Physical Chemistry Letters* **2011**, *2* (5), 402-406.
42. Yagi, M.; Tomita, E.; Kuwabara, T., Remarkably high activity of electrodeposited IrO₂ film for electrocatalytic water oxidation. *J. Electroanal. Chem.* **2005**, *579* (1), 83-88.
43. Biswas, K.; Rao, C., Synthesis and characterization of nanocrystals of the oxide metals, RuO₂, IrO₂, and ReO₃. *Journal of Nanoscience and Nanotechnology* **2007**, *7* (6), 1969-1974.
44. Lee, Y.; Suntivich, J.; May, K. J.; Perry, E. E.; Shao-Horn, Y., Synthesis and activities of rutile IrO₂ and RuO₂ nanoparticles for oxygen evolution in acid and alkaline solutions. *The Journal of Physical Chemistry Letters* **2012**, *3* (3), 399-404.
45. Neyerlin, K.; Bugosh, G.; Forgie, R.; Liu, Z.; Strasser, P., Combinatorial study of high-surface-area binary and ternary electrocatalysts for the oxygen evolution reaction. *J. Electrochem. Soc.* **2009**, *156* (3), B363-B369.
46. Cherevko, S.; Geiger, S.; Kasian, O.; Kulyk, N.; Grote, J.-P.; Savan, A.; Shrestha, B. R.; Merzlikin, S.; Breitbach, B.; Ludwig, A., Oxygen and hydrogen evolution reactions on Ru, RuO₂, Ir, and IrO₂ thin film electrodes in acidic and alkaline electrolytes: A comparative study on activity and stability. *Catal. Today* **2016**, *262*, 170-180.
47. Reier, T.; Oezaslan, M.; Strasser, P., Electrocatalytic oxygen evolution reaction (OER) on Ru, Ir, and Pt catalysts: a comparative study of nanoparticles and bulk materials. *ACS Catal.* **2012**, *2* (8), 1765-1772.
48. Jirkovský, J.; Hoffmannová, H.; Klementová, M.; Krtil, P., Particle size dependence of the electrocatalytic activity of nanocrystalline RuO₂ electrodes. *J. Electrochem. Soc.* **2006**, *153* (6), E111-E118.
49. Jirkovský, J.; Makarova, M.; Krtil, P., Particle size dependence of oxygen evolution reaction on nanocrystalline RuO₂ and Ru_{0.8}Co_{0.2}O_{2-x}. *Electrochem. Commun.* **2006**, *8* (9), 1417-1422.
50. Feng, J.; Lv, F.; Zhang, W.; Li, P.; Wang, K.; Yang, C.; Wang, B.; Yang, Y.; Zhou, J.; Lin, F., Iridium-based multimetallic porous hollow nanocrystals for efficient overall-water-splitting catalysis. *Adv. Mater.* **2017**, *29* (47), 1703798.

51. Cheng, J.; Zhang, H.; Chen, G.; Zhang, Y., Study of $\text{Ir}_x\text{Ru}_{1-x}\text{O}_2$ oxides as anodic electrocatalysts for solid polymer electrolyte water electrolysis. *Electrochim. Acta* **2009**, *54* (26), 6250-6256.
52. Mamaca, N.; Mayousse, E.; Arrii-Clacens, S.; Napporn, T.; Servat, K.; Guillet, N.; Kokoh, K., Electrochemical activity of ruthenium and iridium based catalysts for oxygen evolution reaction. *Applied Catalysis B: Environmental* **2012**, *111*, 376-380.
53. Owe, L.-E.; Tsyppkin, M.; Wallwork, K. S.; Haverkamp, R. G.; Sunde, S., Iridium–ruthenium single phase mixed oxides for oxygen evolution: Composition dependence of electrocatalytic activity. *Electrochim. Acta* **2012**, *70*, 158-164.
54. Wang, L.; Saveleva, V. A.; Zafeiratos, S.; Savinova, E. R.; Lettenmeier, P.; Gazdzicki, P.; Gago, A. S.; Friedrich, K. A., Highly active anode electrocatalysts derived from electrochemical leaching of Ru from metallic $\text{Ir}_{0.7}\text{Ru}_{0.3}$ for proton exchange membrane electrolyzers. *Nano Energy* **2017**, *34*, 385-391.
55. Danilovic, N.; Subbaraman, R.; Chang, K. C.; Chang, S. H.; Kang, Y.; Snyder, J.; Paulikas, A. P.; Strmcnik, D.; Kim, Y. T.; Myers, D., Using Surface Segregation To Design Stable Ru-Ir Oxides for the Oxygen Evolution Reaction in Acidic Environments. *Angew. Chem. Int. Ed.* **2014**, *53* (51), 14016-14021.
56. Kasian, O.; Geiger, S.; Stock, P.; Polymeros, G.; Breitbach, B.; Savan, A.; Ludwig, A.; Cherevko, S.; Mayrhofer, K. J., On the origin of the improved ruthenium stability in $\text{RuO}_2\text{-IrO}_2$ mixed oxides. *J. Electrochem. Soc.* **2016**, *163* (11), F3099-F3104.
57. Kötz, R.; Stucki, S., Stabilization of RuO_2 by IrO_2 for anodic oxygen evolution in acid media. *Electrochim. Acta* **1986**, *31* (10), 1311-1316.
58. Spoeri, C.; Kwan, J. T. H.; Bonakdarpour, A.; Wilkinson, D. P.; Strasser, P., The stability challenges of oxygen evolving catalysts: towards a common fundamental understanding and mitigation of catalyst degradation. *Angew. Chem. Int. Ed.* **2017**, *56* (22), 5994-6021.
59. Shan, J.; Guo, C.; Zhu, Y.; Chen, S.; Song, L.; Jaroniec, M.; Zheng, Y.; Qiao, S.-Z., Charge-redistribution-enhanced nanocrystalline Ru@IrO_x electrocatalysts for oxygen evolution in acidic media. *Chem* **2019**, *5* (2), 445-459.
60. Kim, Y.-T.; Lopes, P. P.; Park, S.-A.; Lee, A.-Y.; Lim, J.; Lee, H.; Back, S.; Jung, Y.; Danilovic, N.; Stamenkovic, V., Balancing activity, stability and conductivity of nanoporous core-shell iridium/iridium oxide oxygen evolution catalysts. *Nature communications* **2017**, *8* (1), 1-8.
61. De Chialvo, M. G.; Chialvo, A., Oxygen evolution reaction on $\text{Ni}_x\text{Co}_{3-x}\text{O}_4$ electrodes with spinel structure. *Electrochim. Acta* **1993**, *38* (15), 2247-2252.
62. Subbaraman, R.; Tripkovic, D.; Chang, K.-C.; Strmcnik, D.; Paulikas, A. P.; Hirunsit, P.; Chan, M.; Greeley, J.; Stamenkovic, V.; Markovic, N. M., Trends in activity for the water electrolyser reactions on 3d M (Ni, Co, Fe, Mn) hydr(oxy)oxide catalysts. *Nature Materials* **2012**, *11* (6), 550.
63. Song, F.; Hu, X., Exfoliation of layered double hydroxides for enhanced oxygen evolution catalysis. *Nature communications* **2014**, *5* (1), 1-9.
64. Lu, Z.; Wang, H.; Kong, D.; Yan, K.; Hsu, P.-C.; Zheng, G.; Yao, H.; Liang, Z.; Sun, X.; Cui, Y., Electrochemical tuning of layered lithium transition metal oxides for improvement of oxygen evolution reaction. *Nature communications* **2014**, *5* (1), 1-7.
65. Liang, H.; Meng, F.; Cabán-Acevedo, M.; Li, L.; Forticaux, A.; Xiu, L.; Wang, Z.; Jin, S., Hydrothermal continuous flow synthesis and exfoliation of NiCo layered

- double hydroxide nanosheets for enhanced oxygen evolution catalysis. *Nano Lett.* **2015**, *15* (2), 1421-1427.
66. Li, M.; Xiong, Y.; Liu, X.; Bo, X.; Zhang, Y.; Han, C.; Guo, L., Facile synthesis of electrospun MFe_2O_4 (M= Co, Ni, Cu, Mn) spinel nanofibers with excellent electrocatalytic properties for oxygen evolution and hydrogen peroxide reduction. *Nanoscale* **2015**, *7* (19), 8920-8930.
67. Nikolov, I.; Darkaoui, R.; Zhecheva, E.; Stoyanova, R.; Dimitrov, N.; Vitanov, T., Electrocatalytic activity of spinel related cobaltites $M_xCo_{3-x}O_4$ (M= Li, Ni, Cu) in the oxygen evolution reaction. *J. Electroanal. Chem.* **1997**, *429* (1-2), 157-168.
68. Vojvodic, A.; Nørskov, J. K., Optimizing perovskites for the water-splitting reaction. *Science* **2011**, *334* (6061), 1355-1356.
69. Bockris, J. O. M.; Otagawa, T., The electrocatalysis of oxygen evolution on perovskites. *J. Electrochem. Soc.* **1984**, *131* (2), 290.
70. Liu, Y.; Wang, H.; Lin, D.; Liu, C.; Hsu, P.-C.; Liu, W.; Chen, W.; Cui, Y., Electrochemical tuning of olivine-type lithium transition-metal phosphates as efficient water oxidation catalysts. *Energy. Environ. Sci.* **2015**, *8* (6), 1719-1724.
71. Burns, R. G.; Burns, R. G., *Mineralogical applications of crystal field theory*. Cambridge University Press: 1993; Vol. 5.
72. Wang, H.-Y.; Hung, S.-F.; Chen, H.-Y.; Chan, T.-S.; Chen, H. M.; Liu, B., In operando identification of geometrical-site-dependent water oxidation activity of spinel Co_3O_4 . *J. Am. Chem. Soc.* **2016**, *138* (1), 36-39.
73. Wang, H. Y.; Hsu, Y. Y.; Chen, R.; Chan, T. S.; Chen, H. M.; Liu, B., Ni³⁺-Induced Formation of Active NiOOH on the Spinel Ni–Co Oxide Surface for Efficient Oxygen Evolution Reaction. *Advanced Energy Materials* **2015**, *5* (10), 1500091.
74. Tung, C.-W.; Hsu, Y.-Y.; Shen, Y.-P.; Zheng, Y.; Chan, T.-S.; Sheu, H.-S.; Cheng, Y.-C.; Chen, H. M., Reversible adapting layer produces robust single-crystal electrocatalyst for oxygen evolution. *Nature communications* **2015**, *6*, 8106.
75. Oliva, P.; Leonardi, J.; Laurent, J.; Delmas, C.; Braconnier, J.; Figlarz, M.; Fievet, F.; Guibert, A. d., Review of the structure and the electrochemistry of nickel hydroxides and oxy-hydroxides. *J. Power Sources* **1982**, *8*, 229-255.
76. Hall, D. S.; Lockwood, D. J.; Bock, C.; MacDougall, B. R., Nickel hydroxides and related materials: a review of their structures, synthesis and properties. *Proc. Math. Phys. Eng. Sci.* **2015**, *471* (2174), 20140792.
77. Klaus, S.; Cai, Y.; Louie, M. W.; Trotochaud, L.; Bell, A. T., Effects of Fe electrolyte impurities on Ni(OH)₂/NiOOH structure and oxygen evolution activity. *J. Phys. Chem. C* **2015**, *119* (13), 7243-7254.
78. Dionigi, F.; Strasser, P., NiFe-Based (Oxy) hydroxide Catalysts for Oxygen Evolution Reaction in Non-Acidic Electrolytes. *Advanced Energy Materials* **2016**, *6* (23), 1600621.
79. Bode, H.; Dehmelt, K.; Witte, J., Zur kenntnis der nickelhydroxidelektrode—I. Über das nickel (II)-hydroxidhydrat. *Electrochim. Acta* **1966**, *11* (8), 1079-1087.
80. Wehrens-Dijksma, M.; Notten, P., Electrochemical quartz microbalance characterization of Ni(OH)₂-based thin film electrodes. *Electrochim. Acta* **2006**, *51* (18), 3609-3621.
81. Kamath, P. V.; Therese, G. H. A.; Gopalakrishnan, J., On the existence of hydrotalcite-like phases in the absence of trivalent cations. *J. Solid State Chem.* **1997**, *128* (1), 38-41.

82. Farhat, R.; Dhainy, J.; Halaoui, L. I., OER Catalysis at Activated and Codeposited NiFe-Oxo/Hydroxide Thin Films Is Due to Postdeposition Surface-Fe and Is Not Sustainable without Fe in Solution. *ACS Catal.* **2020**, *10* (1), 20-35.
83. Klaus, S.; Louie, M. W.; Trotochaud, L.; Bell, A. T., Role of Catalyst Preparation on the Electrocatalytic Activity of Ni_{1-x}Fe_xOOH for the Oxygen Evolution Reaction. *J. Phys. Chem. C* **2015**, *119* (32), 18303-18316.
84. McEwen, R., Crystallographic studies on nickel hydroxide and the higher nickel oxides. *The Journal of Physical Chemistry* **1971**, *75* (12), 1782-1789.
85. Tessier, C.; Guerlou-Demourgues, L.; Faure, C.; Basterreix, M. t.; Nabias, G.; Delmas, C., Structural and textural evolution of zinc-substituted nickel hydroxide electrode materials upon ageing in KOH and upon redox cycling. *Solid State Ionics* **2000**, *133* (1-2), 11-23.
86. Hickling, A.; Hill, S., Oxygen overvoltage. Part I. The influence of electrode material, current density, and time in aqueous solution. *Discussions of the Faraday Society* **1947**, *1*, 236-246.
87. Munshi, M.; Tseung, A.; Parker, J., The dissolution of iron from the negative material in pocket plate nickel-cadmium batteries. *J. Appl. Electrochem.* **1985**, *15* (5), 711-717.
88. Falk, S. U.; Salkind, A. J., *Alkaline storage batteries*, Wiley: 1969.
89. Troilius, G.; Alfelt, G., The migration of iron in alkaline nickel-cadmium cells with pocket electrodes. In *Power Sources*, Elsevier: 1967; pp 337-347.
90. Tichenor, R. L., Nickel Oxides-Relation Between Electrochemical and Foreign Ion Content. *Industrial & Engineering Chemistry* **1952**, *44* (5), 973-977.
91. Młynarek, G.; Paszkiewicz, M.; Radniecka, A., The effect of ferric ions on the behaviour of a nickelous hydroxide electrode. *J. Appl. Electrochem.* **1984**, *14* (2), 145-149.
92. Corrigan, D. A., The catalysis of the oxygen evolution reaction by iron impurities in thin film nickel oxide electrodes. *J. Electrochem. Soc.* **1987**, *134* (2), 377-384.
93. Bediako, D. K.; Lassalle-Kaiser, B.; Surendranath, Y.; Yano, J.; Yachandra, V. K.; Nocera, D. G., Structure–activity correlations in a nickel–borate oxygen evolution catalyt. *J. Am. Chem. Soc.* **2012**, *134* (15), 6801-6809.
94. Trotochaud, L.; Young, S. L.; Ranney, J. K.; Boettcher, S. W., Nickel–iron oxyhydroxide oxygen-evolution electrocatalysts: the role of intentional and incidental iron incorporation. *J. Am. Chem. Soc.* **2014**, *136* (18), 6744-6753.
95. Smith, A. M.; Trotochaud, L.; Burke, M. S.; Boettcher, S. W., Contributions to activity enhancement via Fe incorporation in Ni-(oxy) hydroxide/borate catalysts for near-neutral pH oxygen evolution. *Chem. Commun.* **2015**, *51* (25), 5261-5263.
96. Li, N.; Bediako, D. K.; Hadt, R. G.; Hayes, D.; Kempa, T. J.; Von Cube, F.; Bell, D. C.; Chen, L. X.; Nocera, D. G., Influence of iron doping on tetravalent nickel content in catalytic oxygen evolving films. *Proc. Natl. Acad. Sci.* **2017**, *114* (7), 1486-1491.
97. Corrigan, D. A.; Bendert, R. M., Effect of coprecipitated metal ions on the electrochemistry of nickel hydroxide thin films: cyclic voltammetry in 1M KOH. *J. Electrochem. Soc.* **1989**, *136* (3), 723-728.
98. Corrigan, D. A., Effect of Coprecipitated Metal Ions on the Electrochemistry of Nickel Hydroxide Thin Films: Cyclic Voltammetry in 1M KOH. *J. Electrochem. Soc.* **1989**, *136* (3), 723.

99. Corrigan, D. A.; Conell, R. S.; Fierro, C. A.; Scherson, D. A., In-situ Moessbauer study of redox processes in a composite hydroxide of iron and nickel. *J. Phys. Chem.* **1987**, *91* (19), 5009-5011.
100. Friebel, D.; Louie, M. W.; Bajdich, M.; Sanwald, K. E.; Cai, Y.; Wise, A. M.; Cheng, M.-J.; Sokaras, D.; Weng, T.-C.; Alonso-Mori, R.; Davis, R. C.; Bargar, J. R.; Nørskov, J. K.; Nilsson, A.; Bell, A. T., Identification of Highly Active Fe Sites in (Ni,Fe)OOH for Electrocatalytic Water Splitting. *Journal of the American Chemical Society* **2015**, *137* (3), 1305-1313.
101. Smith, R. D.; Prévot, M. S.; Fagan, R. D.; Trudel, S.; Berlinguette, C. P., Water oxidation catalysis: electrocatalytic response to metal stoichiometry in amorphous metal oxide films containing iron, cobalt, and nickel. *J. Am. Chem. Soc.* **2013**, *135* (31), 11580-11586.
102. Trotochaud, L.; Ranney, J. K.; Williams, K. N.; Boettcher, S. W., Solution-cast metal oxide thin film electrocatalysts for oxygen evolution. *J. Am. Chem. Soc.* **2012**, *134* (41), 17253-17261.
103. Gerken, J. B.; Shaner, S. E.; Massé, R. C.; Porubsky, N. J.; Stahl, S. S., A survey of diverse earth abundant oxygen evolution electrocatalysts showing enhanced activity from Ni-Fe oxides containing a third metal. *Energy. Environ. Sci.* **2014**, *7* (7), 2376-2382.
104. Louie, M. W.; Bell, A. T., An investigation of thin-film Ni-Fe oxide catalysts for the electrochemical evolution of oxygen. *J. Am. Chem. Soc.* **2013**, *135* (33), 12329-12337.
105. Bates, M. K.; Jia, Q.; Doan, H.; Liang, W.; Mukerjee, S., Charge-transfer effects in Ni-Fe and Ni-Fe-Co mixed-metal oxides for the alkaline oxygen evolution reaction. *ACS Catal.* **2015**, *6* (1), 155-161.
106. Diaz-Morales, O.; Ledezma-Yanez, I.; Koper, M. T.; Calle-Vallejo, F., Guidelines for the rational design of Ni-based double hydroxide electrocatalysts for the oxygen evolution reaction. *ACS Catal.* **2015**, *5* (9), 5380-5387.
107. Chen, J. Y.; Dang, L.; Liang, H.; Bi, W.; Gerken, J. B.; Jin, S.; Alp, E. E.; Stahl, S. S., Operando analysis of NiFe and Fe oxyhydroxide electrocatalysts for water oxidation: detection of Fe⁴⁺ by Mossbauer spectroscopy. *J. Am. Chem. Soc.* **2015**, *137* (48), 15090-15093.
108. Friebel, D.; Louie, M. W.; Bajdich, M.; Sanwald, K. E.; Cai, Y.; Wise, A. M.; Cheng, M.-J.; Sokaras, D.; Weng, T.-C.; Alonso-Mori, R., Identification of highly active Fe sites in (Ni, Fe) OOH for electrocatalytic water splitting. *J. Am. Chem. Soc.* **2015**, *137* (3), 1305-1313.
109. Li, Y.-F.; Selloni, A., Mechanism and activity of water oxidation on selected surfaces of pure and Fe-doped NiO_x. *ACS Catal.* **2014**, *4* (4), 1148-1153.
110. Ahn, H. S.; Bard, A. J., Surface Interrogation Scanning Electrochemical Microscopy of Ni_{1-x}Fe_xOOH (0 < x < 0.27) Oxygen Evolving Catalyst: Kinetics of the "fast" Iron Sites. *J. Am. Chem. Soc.* **2016**, *138* (1), 313-318.
111. Burke, M. S.; Zou, S.; Enman, L. J.; Kellon, J. E.; Gabor, C. A.; Pledger, E.; Boettcher, S. W., Revised oxygen evolution reaction activity trends for first-row transition-metal (oxy) hydroxides in alkaline media. *The journal of physical chemistry letters* **2015**, *6* (18), 3737-3742.
112. Zou, S.; Burke, M. S.; Kast, M. G.; Fan, J.; Danilovic, N.; Boettcher, S. W., Fe (oxy) hydroxide oxygen evolution reaction electrocatalysis: Intrinsic activity and the

- roles of electrical conductivity, substrate, and dissolution. *Chem. Mater.* **2015**, *27* (23), 8011-8020.
113. Goldsmith, Z. K.; Harshan, A. K.; Gerken, J. B.; Vörös, M.; Galli, G.; Stahl, S. S.; Hammes-Schiffer, S., Characterization of NiFe oxyhydroxide electrocatalysts by integrated electronic structure calculations and spectroelectrochemistry. *Proc. Natl. Acad. Sci.* **2017**, *114* (12), 3050-3055.
114. Martirez, J. M. P.; Carter, E. A., Unraveling oxygen evolution on iron-doped β -nickel oxyhydroxide: The key role of highly active molecular-like sites. *J. Am. Chem. Soc.* **2018**, *141* (1), 693-705.
115. Xu, D.; Stevens, M. B.; Rui, Y.; DeLuca, G.; Boettcher, S. W.; Reichmanis, E.; Li, Y.; Zhang, Q.; Wang, H., The role of Cr doping in NiFe oxide/(oxy) hydroxide electrocatalysts for oxygen evolution. *Electrochim. Acta* **2018**, *265*, 10-18.
116. Martirez, J. M. P.; Carter, E. A., Non-innocent Influence of Host β -NiOOH Redox Activity on Transition-Metal Dopants' Efficacy as Active Sites in Electrocatalytic Water Oxidation. *ACS Catal.* **2020**.
117. Bard, A. J., Inner-sphere heterogeneous electrode reactions. Electrocatalysis and photocatalysis: the challenge. *J. Am. Chem. Soc.* **2010**, *132* (22), 7559-7567.
118. Wu, G.; Li, N.; Zhou, D.-R.; Mitsuo, K.; Xu, B.-Q., Anodically electrodeposited Co+Ni mixed oxide electrode: preparation and electrocatalytic activity for oxygen evolution in alkaline media. *J. Solid State Chem.* **2004**, *177* (10), 3682-3692.
119. Cui, B.; Lin, H.; Li, J. B.; Li, X.; Yang, J.; Tao, J., Core-ring structured NiCo₂O₄ nanoplatelets: synthesis, characterization, and electrocatalytic applications. *Adv. Funct. Mater.* **2008**, *18* (9), 1440-1447.
120. Tiwari, S.; Samuel, S.; Singh, R.; Poillerat, G.; Koenig, J.; Chartier, P., Active thin NiCo₂O₄ film prepared on nickel by spray pyrolysis for oxygen evolution. *Int. J. Hydrogen Energy* **1995**, *20* (1), 9-15.
121. Singh, N.; Singh, R., Electrocatalytic properties of spinel type Ni_xFe_{3-x}O₄ synthesized at low temperature for oxygen evolution in KOH solutions. **1999**.
122. Jasem, S.; Tseung, A., A potentiostatic pulse study of oxygen evolution on teflon-bonded nickel-cobalt oxide electrodes. *J. Electrochem. Soc.* **1979**, *126* (8), 1353-1360.
123. Balasubramanian, M.; Melendres, C.; Mini, S., X-ray absorption spectroscopy studies of the local atomic and electronic structure of iron incorporated into electrodeposited hydrous nickel oxide films. *J. Phys. Chem. B.* **2000**, *104* (18), 4300-4306.
124. Zhang, T.; Nellist, M. R.; Enman, L. J.; Xiang, J.; Boettcher, S. W., Modes of Fe Incorporation in Co-Fe (Oxy) hydroxide Oxygen Evolution Electrocatalysts. *ChemSusChem* **2019**, *12* (9), 2015-2021.
125. Swierk, J. R.; Klaus, S.; Trotochaud, L.; Bell, A. T.; Tilley, T. D., Electrochemical study of the energetics of the oxygen evolution reaction at nickel iron (oxy) hydroxide catalysts. *J. Phys. Chem. C.* **2015**, *119* (33), 19022-19029.
126. Kim, S.; Tryk, D. A.; Antonio, M. R.; Carr, R.; Scherson, D., In situ X-ray absorption fine structure studies of foreign metal ions in nickel hydrous oxide electrodes in alkaline electrolytes. *The Journal of Physical Chemistry* **1994**, *98* (40), 10269-10276.
127. Batchellor, A. S.; Boettcher, S. W., Pulse-electrodeposited Ni-Fe (oxy) hydroxide oxygen evolution electrocatalysts with high geometric and intrinsic activities at large mass loadings. *ACS Catal.* **2015**, *5* (11), 6680-6689.

128. Stevens, M. B.; Trang, C. D.; Enman, L. J.; Deng, J.; Boettcher, S. W., Reactive Fe-sites in Ni/Fe (oxy) hydroxide are responsible for exceptional oxygen electrocatalysis activity. *J. Am. Chem. Soc.* **2017**, *139* (33), 11361-11364.
129. Barnard, R.; Randell, C.; Tye, F., Studies concerning charged nickel hydroxide electrodes I. Measurement of reversible potentials. *J. Appl. Electrochem.* **1980**, *10* (1), 109-125.
130. Stevens, M. B.; Enman, L. J.; Batchellor, A. S.; Cosby, M. R.; Vise, A. E.; Trang, C. D.; Boettcher, S. W., Measurement techniques for the study of thin film heterogeneous water oxidation electrocatalysts. *Chem. Mater.* **2016**, *29* (1), 120-140.
131. Yeo, B. S.; Bell, A. T., Enhanced activity of gold-supported cobalt oxide for the electrochemical evolution of oxygen. *J. Am. Chem. Soc.* **2011**, *133* (14), 5587-5593.
132. Chen, Y. W. D.; Noufi, R. N., Electrodeposition of nickel and cobalt oxides onto platinum and graphite electrodes for alkaline water electrolysis. *J. Electrochem. Soc.* **1984**, *131* (4), 731-735.
133. Mayrhofer, K.; Crampton, A.; Wiberg, G.; Arenz, M., Analysis of the impact of individual glass constituents on electrocatalysis on Pt electrodes in alkaline solution. *J. Electrochem. Soc.* **2008**, *155* (6), P78-P81.
134. Mayrhofer, K.; Wiberg, G.; Arenz, M., Impact of glass corrosion on the electrocatalysis on Pt electrodes in alkaline electrolyte. *J. Electrochem. Soc.* **2008**, *155* (1), P1-P5.
135. Subbaraman, R.; Danilovic, N.; Lopes, P.; Tripkovic, D.; Strmcnik, D.; Stamenkovic, V.; Markovic, N., Origin of anomalous activities for electrocatalysts in alkaline electrolytes. *J. Phys. Chem. C.* **2012**, *116* (42), 22231-22237.
136. Enman, L. J.; Burke, M. S.; Batchellor, A. S.; Boettcher, S. W., Effects of intentionally incorporated metal cations on the oxygen evolution electrocatalytic activity of nickel (oxy) hydroxide in alkaline media. *ACS Catal.* **2016**, *6* (4), 2416-2423.
137. Brownson, J. R.; Lévy - Clément, C., Electrodeposition of α - and β - cobalt hydroxide thin films via dilute nitrate solution reduction. *Physica Status Solidi (B)* **2008**, *245* (9), 1785-1791.
138. Therese, G. H. A.; Kamath, P. V., Electrochemical synthesis of metal oxides and hydroxides. *Chem. Mater.* **2000**, *12* (5), 1195-1204.
139. Morales-Guio, C. G.; Liardet, L.; Hu, X., Oxidatively electrodeposited thin-film transition metal (oxy) hydroxides as oxygen evolution catalysts. *J. Am. Chem. Soc.* **2016**, *138* (28), 8946-8957.
140. Tench, D.; Warren, L. F., Electrodeposition of conducting transition metal oxide/hydroxide films from aqueous solution. *J. Electrochem. Soc.* **1983**, *130* (4), 869-872.
141. Pinaud, B. A.; Benck, J. D.; Seitz, L. C.; Forman, A. J.; Chen, Z.; Deutsch, T. G.; James, B. D.; Baum, K. N.; Baum, G. N.; Ardo, S., Technical and economic feasibility of centralized facilities for solar hydrogen production via photocatalysis and photoelectrochemistry. *Energy Environ. Sci.* **2013**, *6* (7), 1983-2002.
142. Shaner, M. R.; Atwater, H. A.; Lewis, N. S.; McFarland, E. W., A comparative techno-economic analysis of renewable hydrogen production using solar energy. *Energy Environ. Sci.* **2016**, *9* (7), 2354-2371.
143. Singh, R.-N.; Hamdani, M.; Koenig, J.-F.; Poillerat, G.; Gautier, J.; Chartier, P., Thin films of Co_3O_4 and NiCo_2O_4 obtained by the method of chemical spray pyrolysis for electrocatalysis III. The electrocatalysis of oxygen evolution. *J. Appl. Electrochem.* **1990**, *20* (3), 442-446.

144. Baker, J. G.; Schneider, J. R.; Garrido Torres, J. A.; Singh, J. A.; Mackus, A. J.; Bajdich, M.; Bent, S. F., The Role of Aluminum in Promoting Ni-Fe-OOH Electrocatalysts for the Oxygen Evolution Reaction. *ACS Applied Energy Materials* **2019**, 2 (5), 3488-3499.
145. Chen, J. Y.; Miller, J. T.; Gerken, J. B.; Stahl, S. S., Inverse spinel NiFeAlO₄ as a highly active oxygen evolution electrocatalyst: promotion of activity by a redox-inert metal ion. *Energy. Environ. Sci.* **2014**, 7 (4), 1382-1386.
146. Wang, C.; Zhong, S.; Konstantinov, K.; Walter, G.; Liu, H., Structural study of Al-substituted nickel hydroxide. *Solid State Ionics* **2002**, 148 (3-4), 503-508.
147. Zhu, W.-H.; Ke, J.-J.; Yu, H.-M.; Zhang, D.-J., A study of the electrochemistry of nickel hydroxide electrodes with various additives. *J. Power Sources* **1995**, 56 (1), 75-79.
148. Hu, W.-K.; Noréus, D., Alpha nickel hydroxides as lightweight nickel electrode materials for alkaline rechargeable cells. *Chem. Mater.* **2003**, 15 (4), 974-978.
149. Liu, B.; Wang, X.; Yuan, H.; Zhang, Y.; Song, D.; Zhou, Z., Physical and electrochemical characteristics of aluminium-substituted nickel hydroxide. *J. Appl. Electrochem.* **1999**, 29 (7), 853-858.
150. Vlamidis, Y.; Scavetta, E.; Gazzano, M.; Tonelli, D., Iron vs aluminum based layered double hydroxides as water splitting catalysts. *Electrochim. Acta* **2016**, 188, 653-660.
151. Suntivich, J.; Perry, E. E.; Gasteiger, H. A.; Shao-Horn, Y., The influence of the cation on the oxygen reduction and evolution activities of oxide surfaces in alkaline electrolyte. *Electrocatalysis* **2013**, 4 (1), 49-55.
152. Strmcnik, D.; Kodama, K.; Van der Vliet, D.; Greeley, J.; Stamenkovic, V. R.; Marković, N., The role of non-covalent interactions in electrocatalytic fuel-cell reactions on platinum. *Nature chemistry* **2009**, 1 (6), 466.
153. Zhang, J.; Klasky, M.; Letellier, B. C., The aluminum chemistry and corrosion in alkaline solutions. *J. Nucl. Mater.* **2009**, 384 (2), 175-189.
154. Hem, J. D.; Roberson, C. E. Form and stability of aluminum hydroxide complexes in dilute solution; *USGPO*: **1967**.
155. Brown, O.; Whitley, J., Electrochemical behaviour of aluminium in aqueous caustic solutions. *Electrochim. Acta* **1987**, 32 (4), 545-556.

